

## AN ABSTRACT OF THE THESIS OF

Allan A. Douglas for the degree of Master of Science in Electrical and Computer Engineering presented on April 27, 1993.

Title: Alternating-Current Thin-Film Electroluminescent Device Physics and Modeling.

Redacted for Privacy

Abstract approved: \_\_\_\_\_

Dr. John F. Wager

Alternating-current thin-film electroluminescent (ACTFEL) devices are used in the formation of pixels in flat panel displays. ACTFEL flat panel displays have many advantages over other flat panel technologies. Specifically, ACTFEL panels are emissive displays, they have high brightness, wide viewing angles, and rugged construction. Although much is already known about the operation of ACTFEL devices, several topics related to the device physics and modeling of these devices require further research.

In this work, existing ACTFEL device models are refined by expanding the understanding of ACTFEL device physics and operation. Modeling is separated into three levels of increasing complexity as follows; (1) equivalent circuit modeling, (2) device physics or electrostatic modeling, or (3) Monte Carlo modeling. Each level of model is addressed in this thesis. Existing equivalent circuit models are empirically refined to account for device response to variations in the shape of the driving waveform pulse. The device physics model is expanded by presenting evidence for the formation of space charge in the phosphor layer and the equations prescribing device response are modified accordingly. Also, a new technique for measuring the distribution of interface states in ACTFEL devices is presented. This gives new insight into device operation, as the interface state distribution is one of the most difficult parameters to estimate/measure in the device physics model. Finally, an experiment is presented which attempts to measure the maximum energy of hot electrons during conduction in the phosphor. This research leads to a recommendation of the complexity of the conduction band model needed for accurate Monte Carlo simulation of ACTFEL devices.

**Alternating-Current Thin-Film Electroluminescent Device  
Physics and Modeling**

by

**Allan A. Douglas**

**A THESIS  
submitted to  
Oregon State University**

**in partial fulfillment of  
the requirements for the  
degree of**

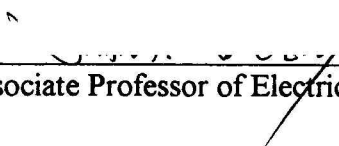
**Master of Science**

**Completed April 27, 1993**

**Commencement June 1993**

**APPROVED:**


Redacted for Privacy

  
Associate Professor of Electrical Engineering & Computer Engineering in charge of major

Redacted for Privacy

  
Head of Department of Electrical & Computer Engineering

Redacted for Privacy

  
Dean of Graduate School

Date thesis is presented: April 27th, 1993

Typed by Allan A. Douglas

## **ACKNOWLEDGEMENTS**

I would to thank Dr. John Wager for his continued support throughout this endeavor and for providing many opportunities to grow both technically and personally.

Acknowledgment is given to Ron Khormaei and Chris King of Planar Systems for providing samples using throughout this research and for their constructive technical recommendations.

In addition, I wish to acknowledge David Morton, Chris Hogg, and James Koh of the U.S. Army LABCOM for the use their laboratory and for generously offering their technical expertise.

Furthermore, I would like to thank my parents, without whom this work would not have been possible. But foremost, I would like to thank my wife, Kathleen Douglas, for her continued support and encouragement, and to whom this thesis is dedicated.

This work was supported by the Center for Advanced Materials Research at Oregon State University, the U.S. Army Research Office under contract DAAL03-91G0242, and by the U.S. Army LABCOM under contract DAAL01-89-C-0927 as administered by GEO-CENTERS, Inc.

## TABLE OF CONTENTS

1.0	INTRODUCTION.....	1
2.0	ACTFEL DEVICES AND OPERATION: LITERATURE REVIEW .....	4
2.1	Device Structure.....	4
2.2	Device Fabrication.....	4
2.3	Physics of Device Operation .....	4
2.4	Electrical Measurement of Device Response .....	8
2.5	Phosphor Space Charge .....	12
2.6	Interface State Distribution .....	13
2.7	Electron Transport.....	13
2.8	Levels of Device Modeling .....	14
2.9	Discussion/Summary.....	16
3.0	WAVEFORM VARIATION TRENDS/EQUIVALENT CIRCUIT MODEL .....	17
3.1	Introduction.....	17
3.2	Experimental Technique.....	17
3.3	Experimental Results .....	19
3.4	Revised Circuit Model .....	22
3.5	Optical Circuit Analogy .....	25
3.6	Discussion/Summary.....	28
4.0	PHOSPHOR SPACE CHARGE/DEVICE PHYSICS MODEL .....	30
4.1	Introduction.....	30
4.2	Experimental Technique.....	30
4.3	Experimental Results .....	32
4.4	Discussion .....	37
4.5	Summary .....	48
5.0	INTERFACE STATE DISTRIBUTION/DEVICE PHYSICS MODEL .....	49
5.1	Introduction.....	49
5.2	Theory.....	49
5.3	Experimental Technique.....	57
5.4	Experimental Results .....	62
5.5	Discussion .....	66
5.6	Summary .....	68
6.0	HOT ELECTRON LUMINESCENCE/MONTE CARLO MODEL .....	70
6.1	Introduction.....	70
6.2	Experimental Technique.....	71
6.3	Experimental Results .....	72
6.4	Discussion .....	76
6.5	Summary .....	77
7.0	CONCLUSIONS AND RECOMMENDATIONS FOR FUTURE WORK.....	78
7.1	Waveform Variation Trends/Equivalent Circuit Model .....	78
7.2	Phosphor Space Charge/Device Physics Model .....	79
7.3	Interface State Distribution/Device Physics Model .....	81
7.4	Hot Electron Luminescence/Monte Carlo Model.....	83
	BIBLIOGRAPHY .....	85

## TABLE OF FIGURES

Figure 2-1.	Typical ACTFEL device structure .....	5
Figure 2-2.	Cycle of energy band diagrams. ....	7
Figure 2-3.	Typical Q-V curve. ....	9
Figure 2-4.	A typical C-V curve. ....	11
Figure 2-5.	Simplest ACTFEL equivalent circuit. ....	15
Figure 3-1.	Waveform variation. ....	18
Figure 3-2.	Q-V loop with response definitions. ....	18
Figure 3-3.	Maximum voltage amplitude variation. ....	19
Figure 3-4.	Pulse width variation. ....	20
Figure 3-5.	Rise/fall time variation. ....	21
Figure 3-6.	Phosphor electric field components. ....	21
Figure 3-7.	Davidson's equivalent circuit model. ....	23
Figure 3-8.	Revised equivalent circuit model. ....	24
Figure 3-9.	Revised circuit parameters. ....	24
Figure 3-10.	Field transients. ....	25
Figure 3-11.	Experimental and simulated intensity transient. ....	26
Figure 3-12.	Optical circuit model. ....	26
Figure 3-13.	Optical circuit parameters. ....	27
Figure 3-14.	Experimental and simulated B-V curves. ....	27
Figure 4-1.	ALE ACTFEL device structure. ....	31
Figure 4-2.	Experimental set-up. ....	32
Figure 4-3.	Voltage and field transients at room temperature. ....	33
Figure 4-4.	Current transients at low and room temperature. ....	34
Figure 4-5.	Secondary current peaks shift with changing temperature. ....	34
Figure 4-6.	Time-resolved luminescence and electric field. ....	35
Figure 4-7.	Emission spectra. ....	36
Figure 4-8.	Device definitions to account for space charge. ....	38
Figure 4-9.	Energy band diagram with no space charge and no external bias. ....	40
Figure 4-10.	Energy band diagram with space charge and no external bias. ....	41
Figure 4-11.	Energy band diagram cycle with space charge. ....	44
Figure 4-12.	Energy states associated with the formation of space charge. ....	45
Figure 4-13.	Electric field transients. ....	47
Figure 5-1.	Emission mechanisms. ....	50
Figure 5-2.	Time evolution of the occupancy function at 1.5 MV/cm. ....	53
Figure 5-3.	Occupancy function after 5 ms at given field strengths. ....	54
Figure 5-4.	Spread of the occupancy function after 5 ms at various fields. ....	55
Figure 5-5.	Emission at various field strengths. ....	56
Figure 5-6.	Field-control experimental set-up. ....	58
Figure 5-7.	Field-control waveforms. ....	59
Figure 5-8.	Field-control circuit. ....	60
Figure 5-9.	Maximum electron emission energy under a constant field for 5 ms. ....	62
Figure 5-10.	Interface state distribution for a SiON ACTFEL device. ....	63
Figure 5-11.	Transferred charge versus energy for an ACTFEL device with BTO. ....	65

Figure 5-12.	ALE ACTFEL device transferred charge versus energy. ....	66
Figure 5-13.	ALE ACTFEL device aged at 200V and operated at 180V. ....	67
Figure 5-14.	ALE ACTFEL device aged and operated at 200V. ....	67
Figure 6-1.	Hot electron luminescence experimental set-up. ....	71
Figure 6-2.	Time-resolved electric field and 460 nm luminescence. ....	72
Figure 6-3.	Hot electron luminescence at various fields. ....	73
Figure 6-4.	Rotated and normal incidence hot electron luminescence. ....	74
Figure 6-5.	ACTFEL film transmission spectra. ....	75
Figure 6-6.	ZnS conduction band density of states. ....	76

# **ALTERNATING-CURRENT THIN-FILM ELECTROLUMINESCENT DEVICE**

## **PHYSICS AND MODELING**

### **1.0 INTRODUCTION**

The video display industry is currently undergoing a dramatic technology revolution. A few of the most evident technologies emerging in the last decade are high definition television (HDTV), heads-up displays, virtual reality, and flat panel displays. Each form of conveying visual information has particular attributes which make it very attractive for specific commercial, industrial, or military applications. Presently, the primary component of the conventional video display, the cathode ray tube or CRT, is being replaced with flat panel technology. Flat panel technology promises to eliminate bulky television and computer monitors with thin, light, and very durable alternatives.

Several implementations of flat panel displays are currently available, namely, liquid crystal displays (LCD), plasma displays, and electroluminescent (EL) displays. Electroluminescence is the process of conversion of electrical energy into luminous energy. EL displays are believed to be promising due to their high brightness, wide viewing angle, high contrast, and emissive nature (i.e. they do not require an external lighting source). EL displays may be made for either dc or ac operation using either power or thin-film phosphors. Alternating-current operation is preferred for matrix addressed displays and fabrication with thin-films is desirable since one can make use of existing solid-state processing technology. For these reasons, this thesis focuses on, alternating-current thin-film electroluminescent (ACTFEL) displays. Recently, full color panels have been demonstrated with each kind of flat panel technology. Even though ACTFEL flat panels seem likely to play an important role in the future of display systems, there are many fabrication and electrical design problems which must be solved if ACTFEL flat panel technology is to become commonplace.

First, processing issues are briefly considered. To replace large CRTs, 19" or even 25" diagonal displays, thin-film EL displays must be manufacturable. This requires



extreme uniformity in deposition as the thin films are typically 5 to 6 thousand angstroms thick. Obviously, this poses a very significant potential yield problem as no defects are tolerable. Additionally, the materials must be chosen to generate appropriate wavelengths of light in the visible spectrum (ie. red, green, and blue). A sufficiently high brightness blue phosphor has proven very difficult to achieve. The materials must not react with one another, diffuse, or, in general, chemically change the operating characteristics of the device after prolonged use.

Secondly, it is essential to have a clear understanding of the physics and electrical characteristics of the device. Understanding the device physics enables one to engineer an optimal set of fabrication parameters and maximize device efficiency. Electrical characterization allows one to monitor device performance, compare different devices, and identify aging phenomena. Finally, a physical understanding of the device is very important for driver circuit design since the matrixed array of pixels behaves as a distributed network or a transmission line. At this point the availability of very accurate models of device behavior becomes necessary.

With this in mind, the goal of the research described in this thesis is to further the understanding of ACTFEL device physics with particular attention paid to enhancing the accuracy of device models.

Chapter 2 is a review of literature relevant to fundamental device physics and modeling of ACTFEL devices. In Chapter 3, the simplest form of device modeling, the equivalent circuit model, is considered. An empirical model is developed which agrees with experimental device response to variations in the driving voltage waveform. Chapter 4 and 5 describe an electrostatic device model proposed by Bringuier<sup>1</sup>. In Chapter 4, this model is expanded to include the special case of phosphor space charge and is shown to match experimental results. Chapter 5 presents a new method for measuring the interface state distribution; the greatest uncertainty in Bringuier's model. An experiment to determine the extent of electron heating during conduction is presented in Chapter 6. This

result indicates the level of model complexity required for accurate Monte Carlo modeling of ACTFEL devices. Finally, Chapter 7 presents conclusions and suggestions for future research. Most of the results presented in this thesis have been published, submitted for publication, or presented orally<sup>2-8</sup>.

## **2.0 ACTFEL DEVICES AND OPERATION: LITERATURE REVIEW**

In this chapter the relevant current literature is reviewed and the basics of the ACTFEL device structure and operation are presented.

### **2.1 Device Structure**

The structure of a typical ACTFEL device is shown in Fig. 1. The device is fabricated on a glass substrate and consists of a phosphor layer sandwiched between two insulating layers and a pair of electrodes. The lower electrode is usually indium-tin oxide (ITO). This material is used because it is transparent to visible light and it has a low sheet resistivity. The insulators are typically silicon oxynitride (SiON), barium tantalate (BTO), or aluminum-titanium oxide (ATO). These materials are chosen because they have high dielectric constants and a high resistance to electrical breakdown. The phosphor layer is typically zinc sulfide, a II-VI semiconductor, doped with manganese (ZnS:Mn).

### **2.2 Device Fabrication**

The ACTFEL fabrication process begins with a glass, Corning 7059, substrate. Deposition of thin-film insulators and phosphors can be achieved with evaporation, sputtering, or various epitaxial methods. This work focuses on evaporated devices with SiON and BTO insulators, as well as devices grown by atomic layer epitaxy<sup>9</sup> (ALE) with ATO insulators.

### **2.3 Physics of Device Operation**

The ACTFEL device operates by applying a large ac voltage across the external electrodes. In a matrix-addressed configuration, as in a flat panel display, a voltage just below the threshold for light emission is applied to the row electrodes. Then another voltage pulse can be applied to the column electrodes such that the total voltage across the device exceeds the threshold voltage such that light is emitted<sup>10</sup>. For research purposes, a sequence of alternating, trapezoidal voltage pulses is applied to a test device. Note that other waveforms such as a triangle (sawtooth) or sinusoid have been used by other

researchers to extract specific kinds of information about ACTFEL devices. The total externally applied voltage is capacitively divided across the two insulator layers and the phosphor layer.

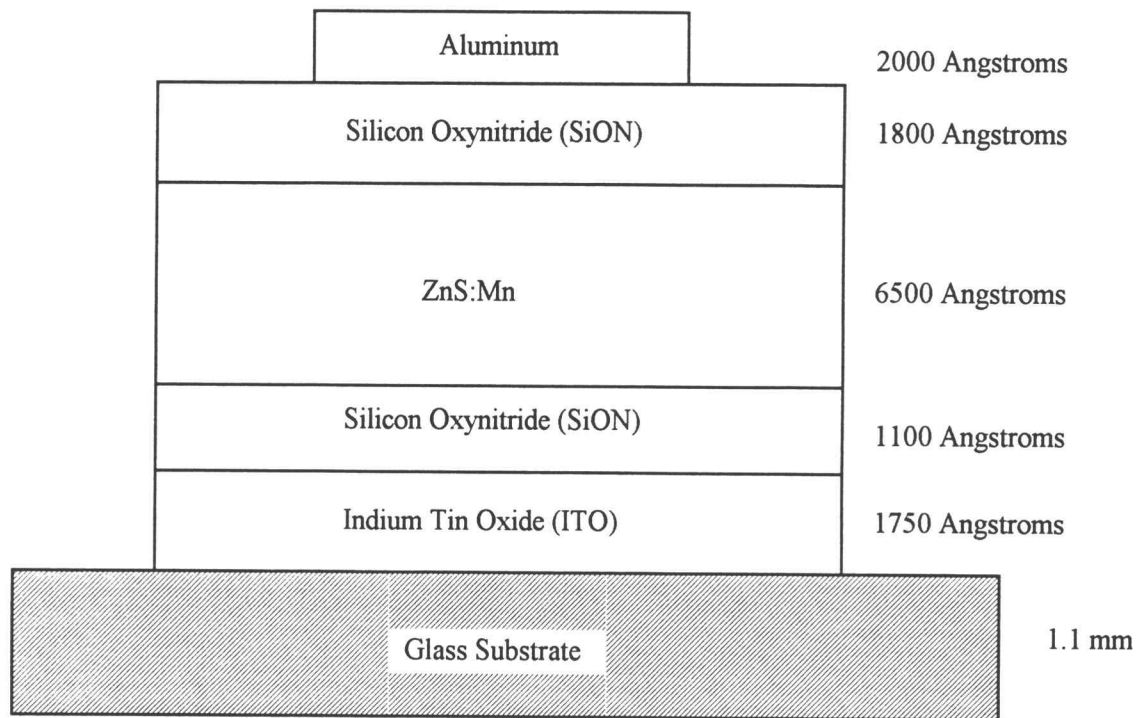


Figure 2-1. Typical ACTFEL device structure.

Figure 2-2 shows the energy band diagrams of the device when driven with an ac voltage. Figure 2-2a depicts the device in a flat band situation with no external bias. When the phosphor voltage, or, more specifically, the phosphor electric field, reaches a critical value corresponding to the external threshold voltage, electrons tunnel out of energy states located at the ZnS/insulator interface into the ZnS conduction band. These states are distributed throughout the band gap and are referred to as interface states. The emitted electrons are accelerated by the phosphor electric field towards the opposite interface as shown in Fig. 2-2b. This pulse of current dissipates real power and is known as conduction current. As the electrons move in the field, they gain energy. If the

electrons gain sufficient energy before reaching the other interface they may be able to impact excite a luminescent impurity; about 2.0 eV is required for Mn. When the impurity atoms decay to their ground state, they emit photons with energy corresponding to the difference between the excited and ground states. For Mn, the emitted light is centered at 585 nm which is yellow-orange in color. Once the electrons reach the opposite interface, they are captured by interface states. In this process of moving electrons from one interface to another, a charge imbalance occurs. The emitting interface becomes net positively charged and the collecting interface becomes net negatively charged, as shown in Fig 2-2c. The absolute value of the charge which remains at one interface after the voltage pulse terminates is called polarization charge. Polarization charge gives rise to a phosphor field component that discourages additional conduction of electrons. The external voltage is zero until the next voltage pulse of opposite polarity arrives, as shown in Fig. 2-2d. Note that during this voltage pulse the polarity of the polarization charge is such that it assists in the emission of electrons. This is very significant in terms of device operation since the turn-on voltage is lowered. In other words, the presence of polarization charge establishes an internal field in the phosphor, therefore, reducing the amount of external voltage required for conduction. The voltage required for the initial onset of conduction without polarization charge is called the threshold voltage and the reduced voltage when polarization charge is present is termed the turn-on voltage. Also note that the resulting conduction current flows in the opposite direction with respect to Fig. 2-2b and, as before, Fig. 2-2e illustrates that the conduction of electrons results in a polarization charge of opposite polarity. This process continues cycling through the energy band diagrams emitting a burst of photons each time current flows in the phosphor. The process reaches steady state in about 2 or 3 periods.

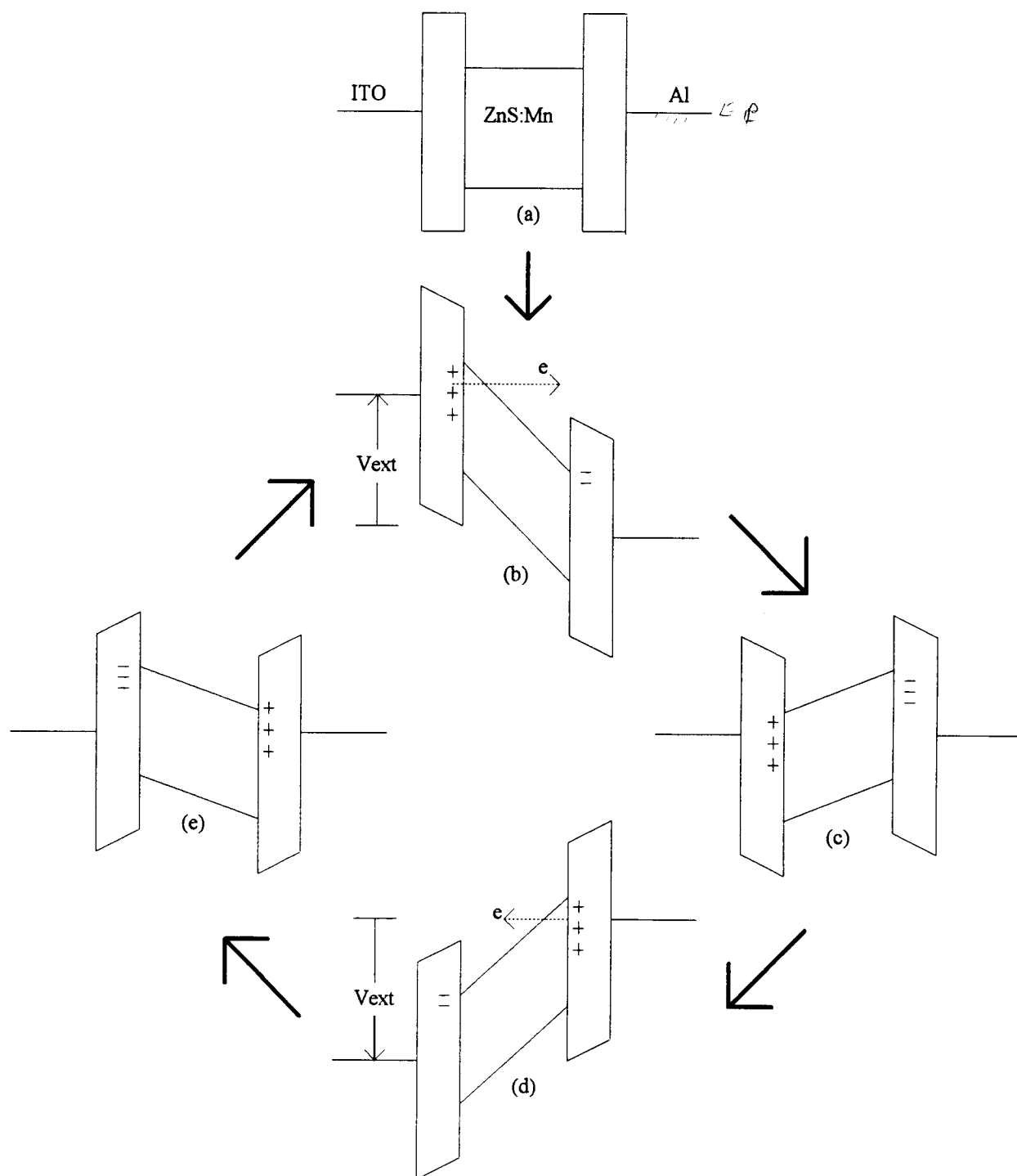


Figure 2-2. Cycle of energy band diagrams.

In summary, with each alternating voltage pulse, conduction current flows in alternating directions in the phosphor layer. Some of these electrons excite luminescent impurity atoms (Mn) which radiatively decay, producing visible photons.

## **2.4 Electrical Measurement of Device Response**

Fundamentally, there are only a few electrically measurable quantities in any characterization of ACTFEL devices. These are separated into the external quantities, measured with respect to the external electrodes of the device, and internal quantities, measured with respect to the phosphor layer. Externally one can measure the applied voltage and the total current or charge flowing through the device as a function of time. Current is measured with either a current probe or as a voltage drop across a small resistor in series with the device. Total external charge is measured as function of time by placing a large capacitor in series with the device which effectively integrates the current. This is known as the Sawyer-Tower configuration<sup>11</sup>. Internal current flowing in the phosphor, conduction current, can be measured with a bridge circuit<sup>12</sup>. First a capacitor is connected in parallel with the device and balanced to match the total capacitance of the ACTFEL device. Then the current is monitored with a current probe; however, one wire from both the device and the parallel capacitor run through the current probe. The wires are run in opposite directions so that the currents cancel and the total current below threshold is zero. Once conduction occurs in the phosphor layer, there is a difference in the current flowing through each wire equal to the internal conduction current.

There are many techniques for processing this seemingly limited set of data which yield tremendous amounts of information about internal device physics. The first technique is known as the charge-voltage (Q-V) method<sup>13</sup>. A Q-V curve is usually generated by plotting the time integral of the current or the Sawyer-Tower charge versus the external voltage. A typical Q-V curve is plotted in Fig. 2-3. This curve is obtained experimentally from a device which has reached the steady state condition. This plot is directly related to the energy band diagrams considered above. First, focus on the point of

0 external voltage and -50 nC. This amount of charge is the polarization charge perceived externally. The actual internal polarization charge can be related to the external charge by,

$$Q_{\text{pol}} = \frac{C_i + C_p}{C_i} Q_{\text{ext}} \quad (2-1)$$

where  $C_i$  and  $C_p$  are the total insulator and phosphor capacitances, respectively. This ratio of capacitances occurs frequently when relating external to internal quantities.

Further note that polarization charge is only defined at  $V_{\text{ext}} = 0$ . In this case the polarization charge just before the positive voltage pulse is equal to the capacitance ratio multiplied by approximately -50 nanocoulombs. The same polarization charge is found just prior to the application of the negative pulse, however the charge is positive. The Q-V curve is traversed counter-clockwise beginning with a positive voltage pulse. The constant slope for voltages less than 110 V is the total capacitance of the ACTFEL structure since,

$$C = \frac{dQ}{dV}. \quad (2-2)$$

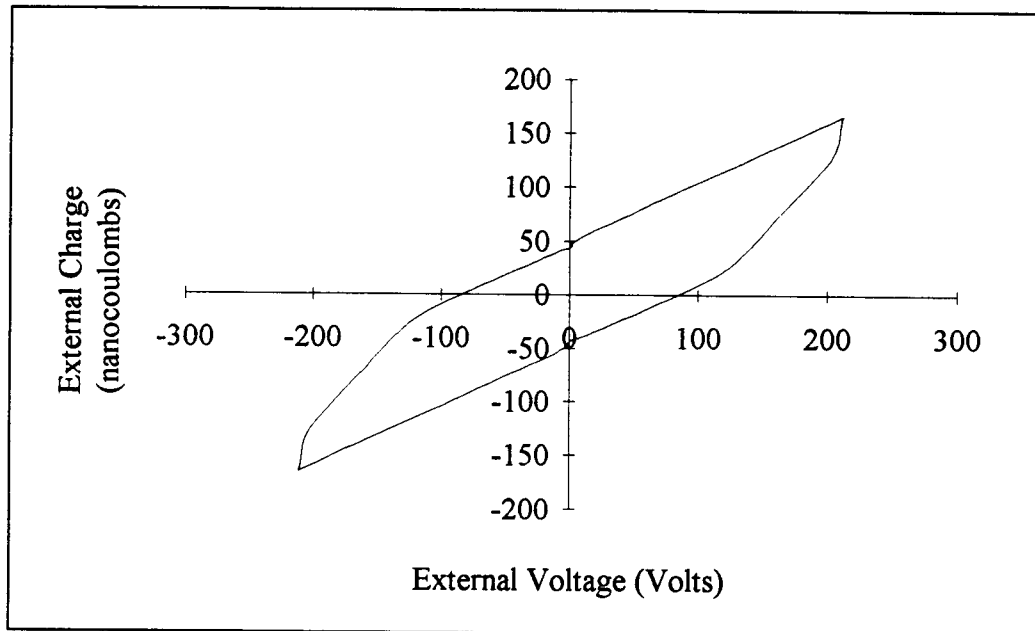


Figure 2-3. Typical Q-V curve.



At 110 V, the turn-on voltage, conduction current begins to flow in the phosphor. This non-destructive breakdown of the phosphor layer results in a change in slope of the Q-V curve. The new slope is the remaining capacitance; the two insulator layer in series as the phosphor capacitance is now effectively shorted. At this point note that if the applied voltage is lower than the threshold voltage, conduction current does not flow and no polarization charge accumulates. If this is the case, the Q-V loop collapses to a single line with a slope equal to the total capacitance. From Fig. 2-3 it is seen that the maximum voltage amplitude is over 200 V which exceeds the threshold voltage of the device and, therefore, opens the Q-V loop. Also note that the Q-V curve is symmetrical about the origin; however, this is not always the case. Some devices are asymmetrical with different turn-on voltages. In addition to capacitances, threshold voltages, and turn-on voltages one can also measure the amount of charge that leaks from the interfaces between voltage pulses (see the discontinuities in Fig. 2-3 at V=0), the relaxation charge (see Chapter 3), conduction charge, polarization charge, and the extent of device asymmetry with the Q-V curve.

Another form of electrical characterization is the capacitance-voltage (C-V) technique<sup>14-18</sup>. The C-V curve is generated by plotting the ratio of the current to the time derivative of the voltage versus the voltage since, from Eqn. 2-2, capacitance is also equal to

$$C = \frac{i(t)}{\frac{dV(t)}{dt}}. \quad (2-3)$$

A typical C-V curve is shown in Fig. 2-4. Total device (~ 0.5 nF) and total insulator (~ 1.4 nF) capacitances can be read directly from this curve as can the threshold voltage (~ 120 V). Davidson<sup>15-17</sup> has used trends in C-V curves to characterize parasitic resistance, estimate interface state density, and study device aging phenomena.

At this point it must be noted that the C-V technique only measures external

quantities, whereas the Q-V technique is capable of measuring internal quantities as well. The preferred method of processing the C-V data is to relate the external quantities to the internal (phosphor layer) values via simple electrostatics. The internal or polarization charge is<sup>1</sup>,

$$Q_{\text{int}}(t) = \frac{C_i + C_p}{C_i} Q_{\text{ext}}(t) - C_p V_{\text{ext}}(t) \quad (2-4)$$

and the internal phosphor and insulator electric fields are,

$$F_p(t) = -\frac{C_i V_{\text{ext}}(t) - Q_{\text{int}}(t)}{d_p (C_i + C_p)} \quad (2-5)$$

and

$$F_i(t) = -\frac{C_p V_{\text{ext}}(t) + Q_{\text{int}}(t)}{d_i (C_i + C_p)} \quad (2-6)$$

where  $d_p$  is the phosphor thickness. Note, that in this form one can substitute Eqn. 2-4 into Eqn. 2-5 and find the internal phosphor field in terms of externally measurable quantities. This calculation is shown in the following equation,

$$F_p(t) = -\frac{1}{d_p} \left[ V_{\text{ext}}(t) - \frac{Q_{\text{ext}}(t)}{C_i} \right]. \quad (2-7)$$

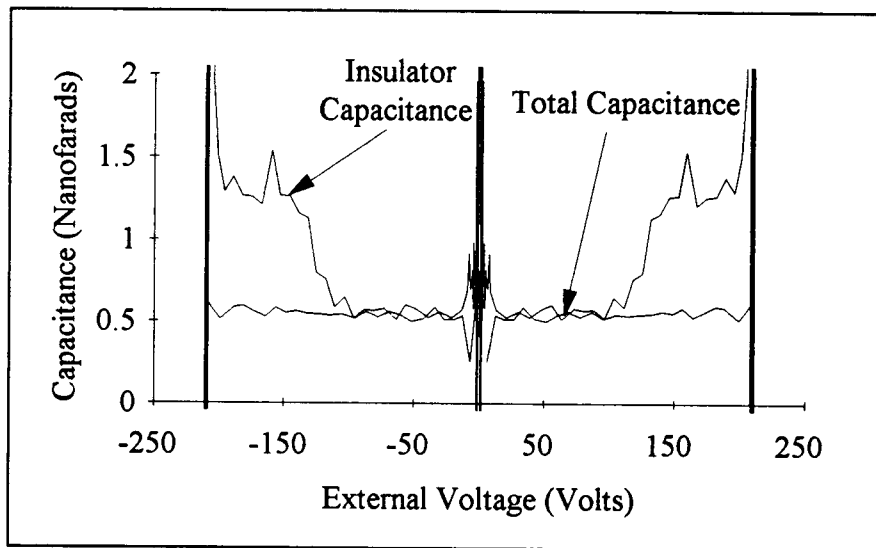


Figure 2-4. A typical C-V curve.

Furthermore, note that these calculations assume that there is no spatial distribution of charge in the phosphor layer (i.e. the field is constant across the phosphor). Calculations based on the existence of space charge are presented in Chapter 4.

## 2.5 Phosphor Space Charge

When space charge is present in the phosphor the energy bands in the phosphor are curved and the electric field is not constant across the phosphor. To determine the amount of curvature one must assume a distribution of charge and solve Poisson's equation. Most researchers believe that space charge occurs in ZnS:Mn ACTFEL devices when they are heavily doped with Mn. This leads to a phenomena known as brightness-voltage (B-V) hysteresis or the memory effect<sup>19</sup>. There is no known method to measure the position of space charge other than building a device with heavily doped probe layers, thus forcing the space charge to occur at a specified position. Understanding the origin and influence of space charge is very important for two reasons. First, space charge causes a distortion of the electric field. If the charge is positive, the field near the emitting interface is increased and a run away or catastrophic breakdown situation may occur. Second, if one interface experiences an increased field relative to the other interface, the conducted charge may be asymmetrical which may cause asymmetrical device aging. The possible processes by which phosphor space charge can be created are field ionization, impact ionization, trapping or capture, electron hole pair generation, and Auger processes<sup>19</sup>. Numerous researchers<sup>20-26</sup> have questioned whether or not the field is constant across the phosphor. Bringuier<sup>27</sup> and Geoffroy<sup>28</sup> have reported the presence of space charge in ALE devices using a "frequency scaling criterion". Neyts<sup>29</sup> has also recently reported the presence of positive space charge in ZnS:Mn devices which occurs only in the first few pulses (the transient regime) with a Q-V measurement. A paper by Mikami et al.<sup>30</sup> will prove to be very important as a verification of observations during the investigation of space charge effects.

## 2.6 Interface State Distribution

The interface state distribution is one area of ACTFEL device physics which is still a great mystery. Knowledge of the interface state distribution would enable one to examine device asymmetry, aging, and provide the necessary feedback for interface engineering to optimize device performance. The origin of interface states is attributed to atomic disorder at the insulator/phosphor interface leading to a continuum of states or perhaps a specific set of traps states associated with an impurity atom or vacancy in either the insulator, the phosphor, or both. Most researchers agree, however, that the density of interface states becomes significant for energies from 0.6 eV to 1.0 eV from the edge of the conduction band<sup>1,19,31</sup>. Kobayashi et al.<sup>31</sup> has suggested a technique for assessing the distribution of filled interface states. Their method leads to high trapped electron densities between 0.6 and 0.8 eV with evaporated ZnS:Mn devices with SiON insulators. Sano<sup>32</sup> reports interface traps as deep as 1.9 eV with thermally stimulated current measurements of evaporated ZnS:Mn devices with yttrium oxide insulators. This result seems too deep for electron emission at typical threshold electric fields of about 1.5 MV/cm. Zheng and Allen<sup>33</sup> have reported deep levels in ZnS at 0.9 and 2.0 eV below the conduction band edge and 0.8 eV above the valence band edge with photocapacitance studies. A listing of various interstitial and substitutional impurities and vacancy trap states has been tabulated by Kröger<sup>34</sup> and Landolt-Börnstein<sup>35</sup>. These levels may be related to interface states/traps or possible states for the formation of space charge as mentioned in the previous section. Two papers from silicon technology are significant because of the theoretical derivation of electron emission rates from trap states<sup>36-37</sup>. This work is crucial of the technique for measuring interface states presented in Chapter 5.

## 2.7 Electron Transport

The topic of electron transport in ZnS ACTFEL devices is a source of much controversy between various researchers. The disagreement arises from the two very different predictions of the electron energy distribution function during conduction. Most

of the work in this area consists of theoretical ensemble Monte Carlo simulations and vacuum emission experiments. Brennan's calculations<sup>38</sup> indicate that the highest energies achieved by the electrons is about 2.5 eV for a field of 1.0 MV/cm. This result is confirmed by Bhattacharyya et al.<sup>39</sup> who found the maximum energy to be about 3.0 eV under the same electric field. However, other researchers<sup>40-41</sup> believe that a ballistic or loss free electron transport occurs giving rise to electron energies of 9 eV or higher. These results seem to be correct as the simulation is apparently confirmed by vacuum emission measurements. However, the simulation did not include all of the relevant physics and the vacuum emission results are highly prone to error<sup>42-43</sup>. Also, since the energy range for efficient Mn excitation is 2.0 to 3.1 eV<sup>39</sup>, it is difficult to understand how these devices achieve their high level of efficiency with 9 eV electrons.

Three papers are referenced<sup>30,44-45</sup> which discuss time-resolved optical emission measurements of a broad-band "blue" or white emission in ZnS devices. This emission is believed to be related to electron radiative transitions within the conduction band and, therefore, the energy of the electron distribution during conduction. Finally, note that if the electrons obtain sufficient energy<sup>46</sup>, electron-hole pairs may be generated.

## **2.8 Levels of Device Modeling**

This section of this literature review briefly covers ACTFEL device modeling. Device models can be categorized in three distinct classes. The simplest model, and therefore the least accurate, is the equivalent circuit as shown in Fig. 2-5. The breakdown voltage of the Zener diodes is set to the threshold voltage for the onset of conduction. From this circuit one can see that the phosphor capacitance is shorted during conduction, as required from the discussion in section 2.3. This model was proposed by Smith<sup>19</sup> and refined by Davidson<sup>16-17</sup>.

The next level of model complexity is referred to as the device physics or analytical model<sup>1,27,47</sup>. At this level one includes all basics device physics and electrostatic equations in the description of the device. Solution requires assumptions about interfaces

state density, space charge, and interface occupancy functions, and usually some kind of numerical solution to nonlinear differential equations.

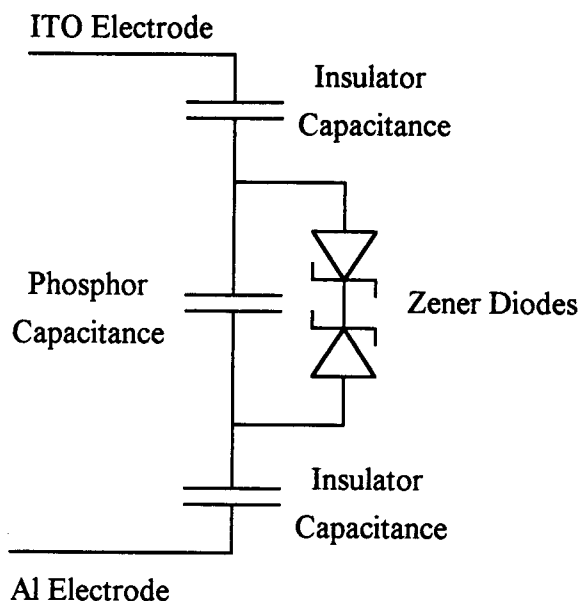


Figure 2-5. Simplest ACTFEL equivalent circuit.

The highest level of modeling is ensemble Monte Carlo simulation. Presently, this form of device modeling is only concerned with the bulk properties of ZnS, but spatial dependence could be included. Monte Carlo modeling simulates electron trajectories and scattering events as the electron moves under the influence of an electric field. Scattering rates for all relevant physical phenomena which effect electron energy and momentum must be included. Bhattacharyya et al.<sup>39</sup> includes polar optical phonon, acoustic phonon, intervalley, ionized impurity, and neutral impurity scattering rates. Additionally, one must describe the Brillouin zone. This is often approximated with parabolic conduction band minima or via a detailed band structure calculation. Generally speaking, accurate Monte Carlo simulations are very computer intensive and depend highly on many material parameters which are not known with a high degree of certainty.

## **2.9 Discussion/Summary**

Much of the ACTFEL device literature relevant to this thesis is reviewed in this chapter. The ACTFEL device structure, basic device physics, and electrical characterization techniques are discussed. Literature pertaining to phosphor space charge, interface states, and electron transport are briefly reviewed as are the three levels of ACTFEL device modeling.

### 3.0 WAVEFORM VARIATION TRENDS/EQUIVALENT CIRCUIT MODEL

#### 3.1 Introduction

In this chapter the electrical response of ZnS:Mn ACTFEL devices is studied as characteristics of the driving waveform are systematically varied. Specifically, the turn-on voltage, total external charge, and relaxation charge are measured as a function of variations in the maximum amplitude, pulse width, and rise/fall time of the driving voltage waveform. A revised equivalent circuit is presented which accurately models the experimental electrical trends. Furthermore, a new model which predicts the optical response with an electric circuit analogy is presented.

#### 3.2 Experimental Technique

The devices measured in this work are fabricated by Planar Systems by evaporation in the typical ACTFEL stack configuration shown in Fig. 2-1. The nominal driving waveform used in this experiment consists of alternating pulses of 210 V amplitude, 5  $\mu$ s rise and fall time, 30  $\mu$ s pulse width, and 1 kHz frequency to approximate normal panel operating conditions. The maximum amplitude, pulse width, and rise/fall time of the driving waveform are varied about this nominal waveform as shown in Fig. 3-1. The electrical response of the device is characterized by digitally acquiring the external voltage and current waveforms, integrating the current, and extracting three quantities from the Q-V curve. In Fig. 3-2 the parameters used to characterize the electrical response are defined.  $Q_{\text{pulse}}$  is defined as the total charge transferred during a single voltage pulse, that is,

$$Q_{\text{pulse}} = 2Q_{\text{ext}}(0) = \frac{2C_i}{C_i + C_p} Q_{\text{pol}}. \quad (3-1)$$

Note that this externally measured quantity is just the width of the Q-V loop. Charge transferred after the voltage pulse reaches its maximum amplitude is also monitored. This charge, denoted as relaxation charge, is a significant fraction of the transferred charge as shown in Fig. 3-2. Finally, recall that  $V_{\text{turn-on}}$  is the external voltage at the onset of



68812/0003

conduction in the phosphor layer.

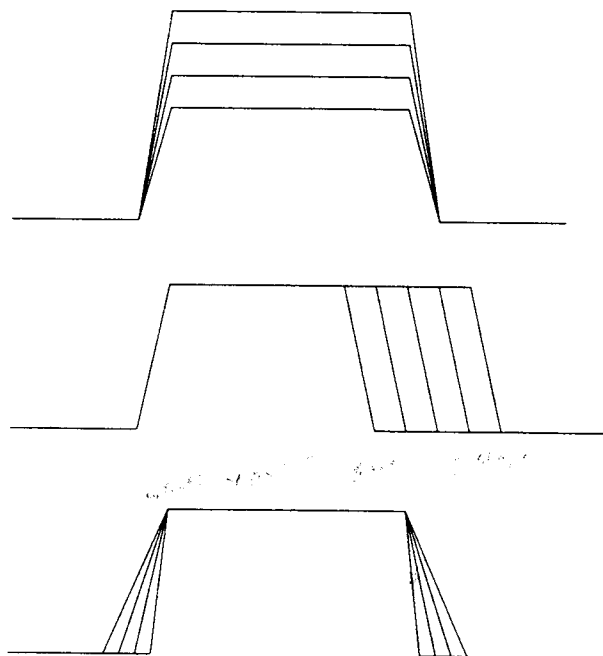


Figure 3-1. Waveform variation.

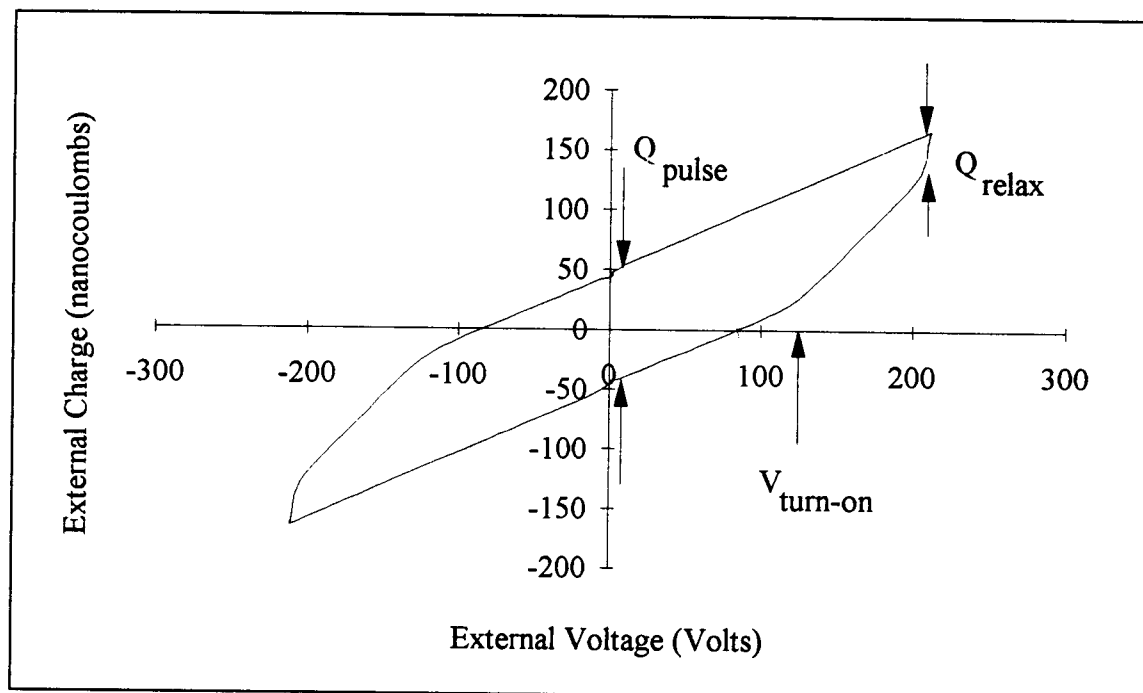


Figure 3-2. Q-V loop with response definitions.

### 3.3 Experimental Results

The systematic trends of  $Q_{\text{pulse}}$ ,  $Q_{\text{relax}}$ , and  $V_{\text{turn-on}}$  are presented in Fig. 3-3 through Fig. 3-5. The results of SPICE simulation using the revised circuit model discussed in the following section are also included for comparison. Experimentally,

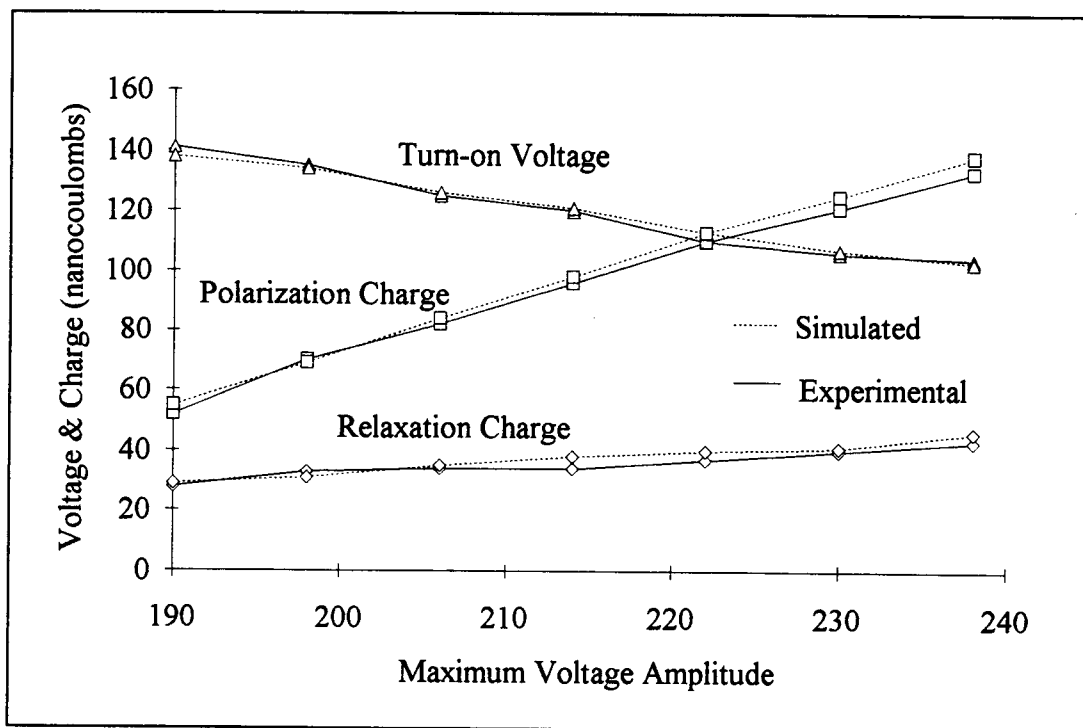


Figure 3-3. Maximum voltage amplitude variation.

it is found that the maximum voltage amplitude has the strongest influence on the device response. Both  $Q_{\text{pulse}}$  and  $V_{\text{turn-on}}$  exhibit a strong linear change over the range of voltage amplitudes employed. Variation of the pulse width results in similar trends, although the effects are of secondary importance. To first order, there is no change in the device response with variations in rise and fall time. These trends can be explained by considering the time-response of the phosphor electric field, as shown in Fig. 3-6. The total phosphor field is calculated using Eqn. 2-5 and the field is separated into two components, one due to the external bias and the other due to the polarization charge, in Eqn. 2-7. Once again, note that these equations presume that the phosphor layer is free of

space charge and, therefore, that the field is constant across the phosphor. Returning to Fig. 3-6, it is found that the initial value of the phosphor field is established by  $Q_{\text{cond}}(0) = Q_{\text{pol}}$ . When the external voltage pulse begins to rise, the phosphor field is eventually driven to a critical-field,  $F(t) = F_{\text{thresh}}$  where;  $V_{\text{ext}} = V_{\text{turn-on}}$ . Notice that the field is essentially constant at  $F_{\text{thresh}}$ . This is phenomena in know as field-clamping. It occurs when sufficient charge can be emitted from the interface to exactly balance the effect of the ramping external voltage. Notice from Fig. 3-6 that the two field components,  $F_{V_{\text{ext}}}$  and  $F_{\text{cond}}$ , have equal and opposite slopes during field-clamping. This means that the charge is emitted from the interface responds in direct proportion to the external voltage. This feedback effect is possible when there is an extremely high density of occupied interface states. More will be said about field-clamping in Chapter 4.

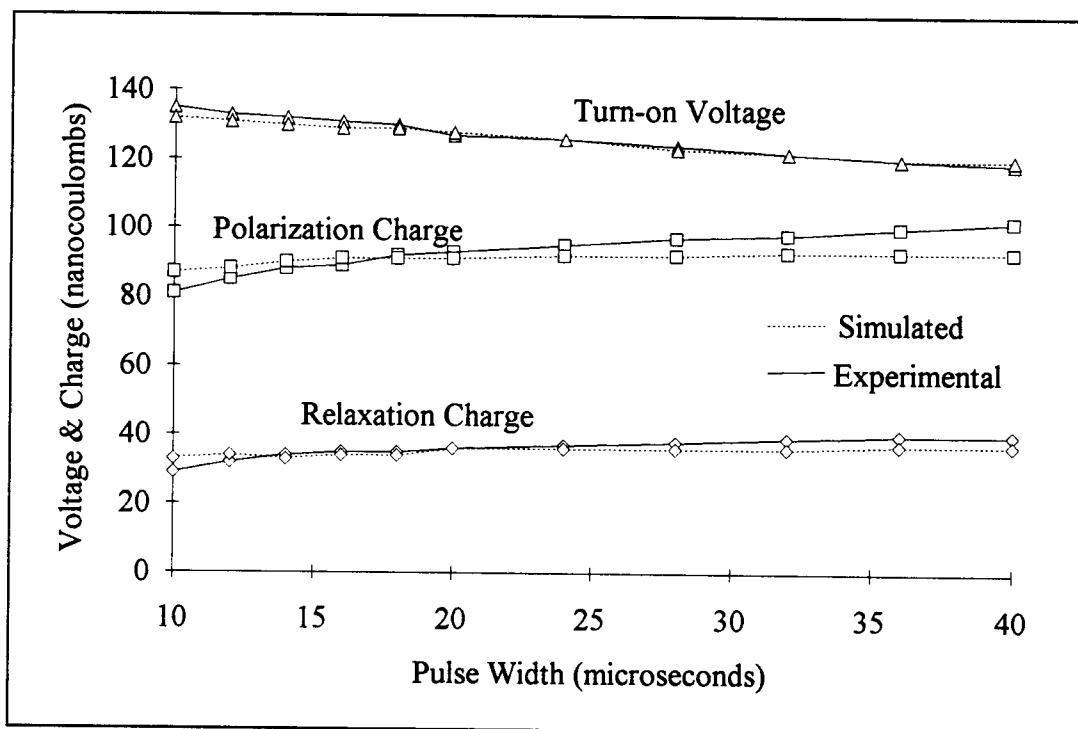


Figure 3-4. Pulse width variation.

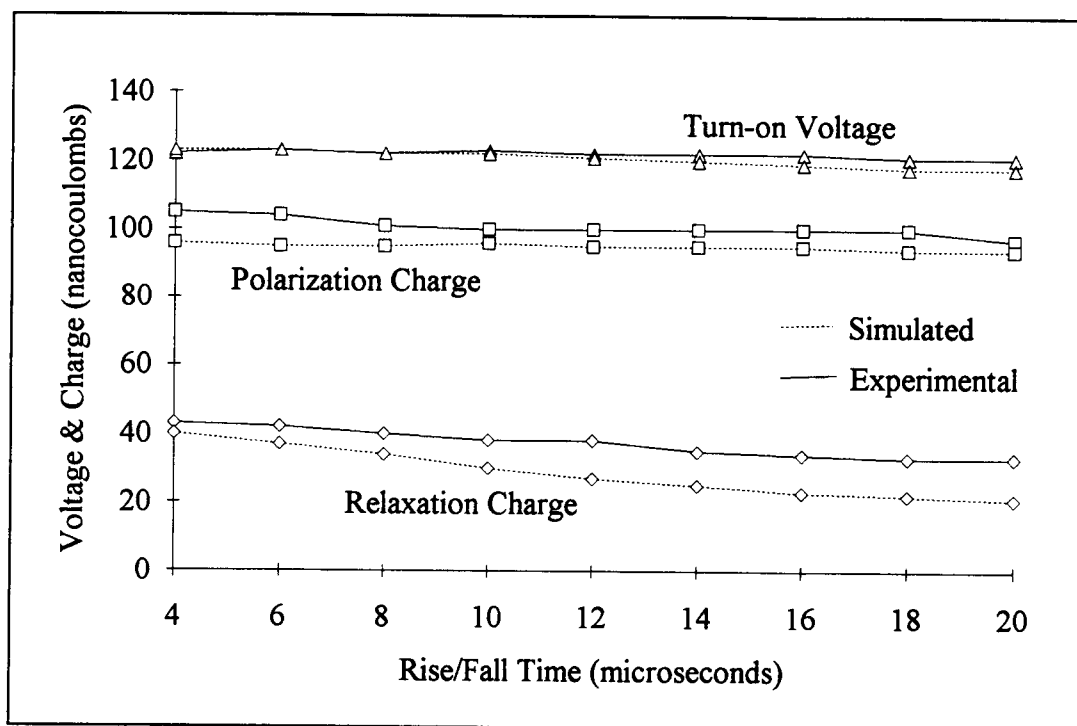


Figure 3-5. Rise/fall time variation.

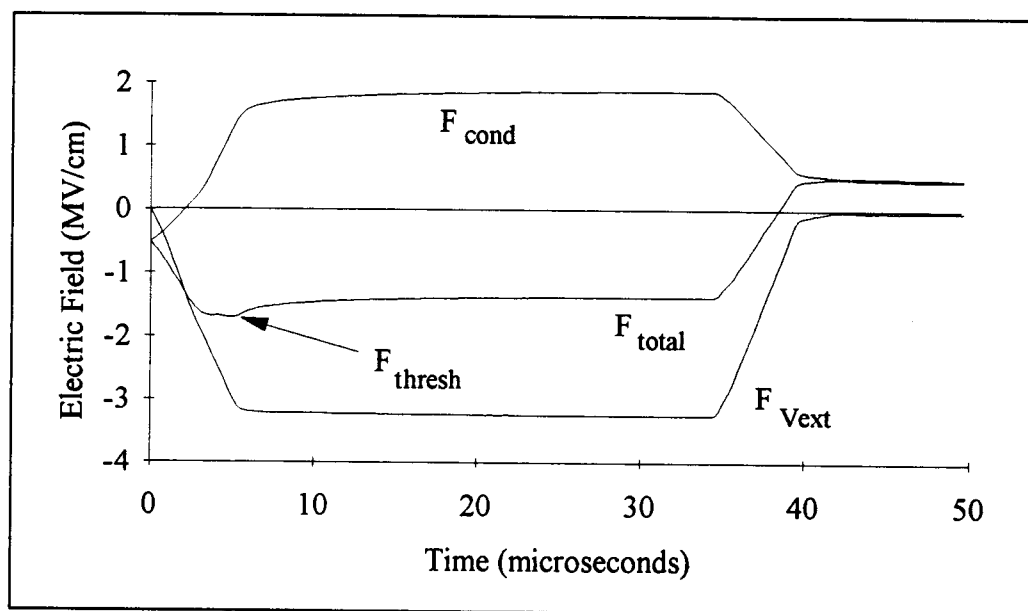


Figure 3-6. Phosphor electric field components.

The trend in the maximum voltage amplitude can now be explained. It is apparent that if the amplitude of the external voltage component increases, additional charge transport is required to keep  $F_{\text{total}}$  at the clamped value, thus,  $Q_{\text{pulse}}$  increases with external voltage amplitude. Also, as  $Q_{\text{pulse}}$  increases,  $Q_{\text{pol}}$  increases as given by Eqn. 3-1. This means that the initial field, at  $t=0$ , is closer to  $F_{\text{thresh}}$ . Therefore,  $V_{\text{turn-on}}$  decreases with increasing pulse amplitude. This relationship can be summarized by the following expression which is based on the geometry of the Q-V curve,

$$V_{\text{turnon}} = \frac{C_i + C_p}{C_i} \left[ \frac{Q_{\text{pulse}}}{2C_i} - d_p F_{\text{thresh}} \right]. \quad (3-2)$$

Notice in Fig. 3-6 that when the external voltage reaches its maximum amplitude, an overshoot in transferred charge occurs. This additional charge transport gives rise to a relaxation of the phosphor field; thus the name relaxation charge. The trends in the pulse width are explained by the modulation of the time for the relaxation charge to settle to a constant value. As the pulse width increases,  $Q_{\text{relax}}$  and, therefore,  $Q_{\text{pol}}$ , increases and  $V_{\text{turn-on}}$  decreases, as prescribed by Eqn. 3-2.

### 3.4 Revised Circuit Model

Attempts were made to develop an equivalent circuit model which includes the detailed physics of ACTFEL device dynamics. This proved extremely difficult, if not impossible, as the coupled differential equations which describe emission from interface states and the electric field transient (see Chapter 4) cannot be modeled with simple circuit elements. For these reasons, an empirical approach to modeling is pursued.

Previous equivalent circuit models for ACTFEL devices<sup>15,17,19</sup> typically consist of three capacitors connected in series to model the insulator/phosphor/insulator stack and a pair of back-to-back Zener diodes which shunt the phosphor capacitor which model conduction across the phosphor layer. Davidson et al.<sup>16-17</sup>, have refined this model, Fig. 3-7, by including insulator and phosphor resistances and a resistor in series with the diodes as a fitting parameter to C-V curves. These equivalent circuits do not accurately model

the waveform dependence of the turn-on voltage and measured charge (relaxation charge cannot be assessed from dynamic C-V curves). Nor do they fit the dynamic electric field or relaxation charge trends described above. By primarily focusing on measured field dynamics and relaxation charge, the refined model shown in Fig. 3-8 was developed. Essentially, a parallel resistor-capacitor combination is added to Davidson's model.

Operation of the revised circuit can be explained by considering the application of an external pulse waveform. Prior to the breakdown of the diodes, displacement current flows through the three series capacitors. After breakdown (turn-on), significant conduction current flows through  $R_d$  and  $C_T$  begins to charge. When the external voltage reaches its maximum amplitude, the displacement charge goes to zero ( $dV_{\text{ext}}/dt = 0$ ), and  $C_T$  begins discharging through  $R_T$ . Since the voltage across the diodes is still at the breakdown voltage, any change in voltage across  $C_T$  is reflected in the voltage across the phosphor capacitor  $C_p$ . Thus, a slow decay in the phosphor voltage (phosphor field) is

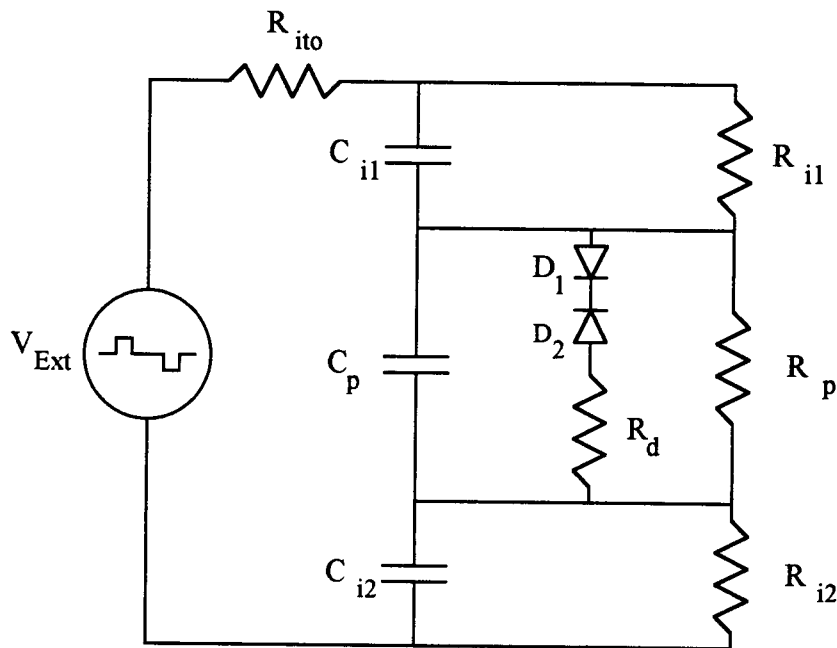


Figure 3-7. Davidson's equivalent circuit model.

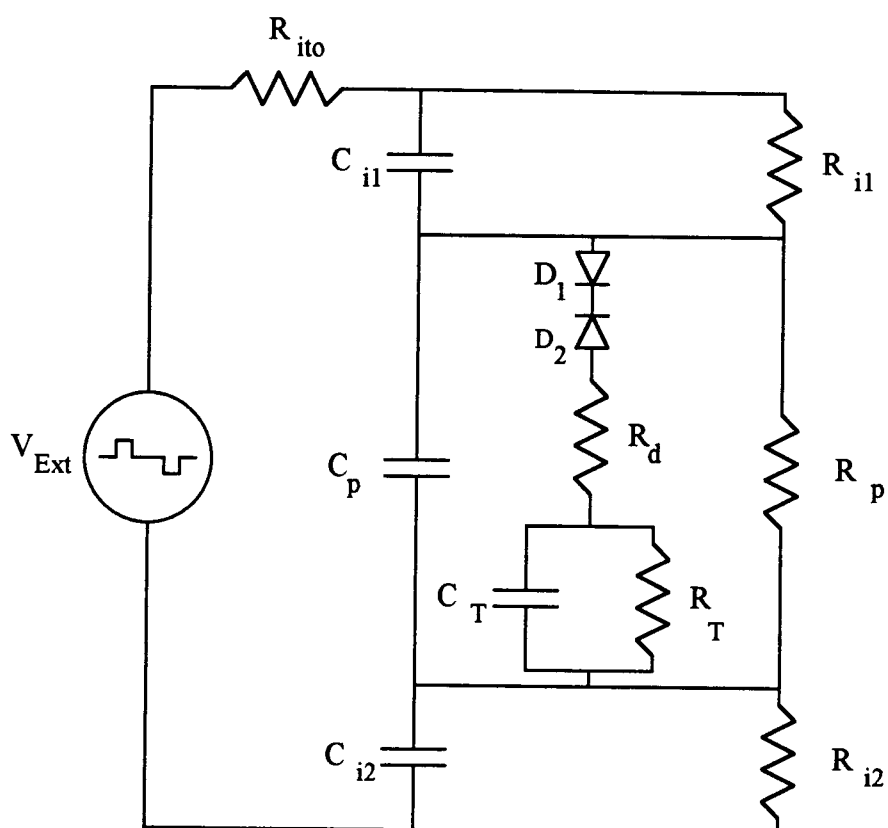


Figure 3-8. Revised equivalent circuit model.

Circuit Element	Value
R <sub>ito</sub>	10 Ohms
C <sub>i1</sub> , C <sub>i2</sub>	1.5 nF
R <sub>i1</sub> , R <sub>i2</sub>	0.1 Gohms
C <sub>p</sub>	0.98 nF
R <sub>p</sub>	6.0 Mohms
R <sub>d</sub>	200 Ohms
C <sub>T</sub>	7.0 nF
R <sub>T</sub>	400 Ohms
Diode Breakdown	100 Volts

Figure 3-9. Revised circuit parameters.

obtained. The predicted field transients for all three models are compared to actual experimental data in Fig. 3-10. Furthermore, Fig. 3-10 illustrates how well the revised model accounts for relaxation charge. As mentioned before, the ability of the revised model to accurately predict the electrical trends of the device response are shown in Fig. 3-3 through Fig. 3-5.

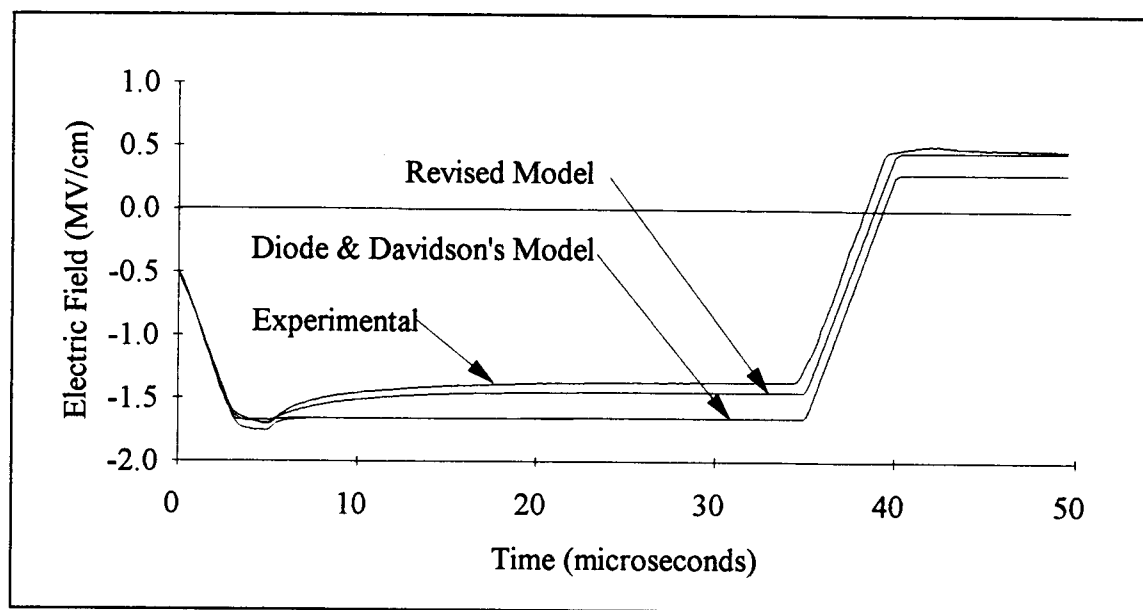


Figure 3-10. Field transients.

Although the relationship between the new electrical circuit elements and the detailed device physics is not yet clear, the essential device dynamics and electrical trends as a function of variations in the driving waveform are taken into account. One cannot model the intricate device physics of the electrostatic model, see Chapter 4, with simple linear circuit elements and diodes. As a point of interest, note that this revised model is strikingly similar to MOS capacitor models<sup>18</sup> for interfaces states in a flat-band condition.

### 3.5 Optical Circuit Analogy

Since primary interest in ACTFEL devices is with respect to their optical properties, the construction of an equivalent circuit which models the optical response of



the device is now considered. The radiative decay of the manganese emission after conduction is experimentally found to consist primarily of the sum two exponential terms. This decay in emission intensity is shown in Fig. 3-11. The time constants are found to be 1.8 ms and 0.31 ms from a least-squares fit. Figure 3-12 illustrates a circuit which utilizes

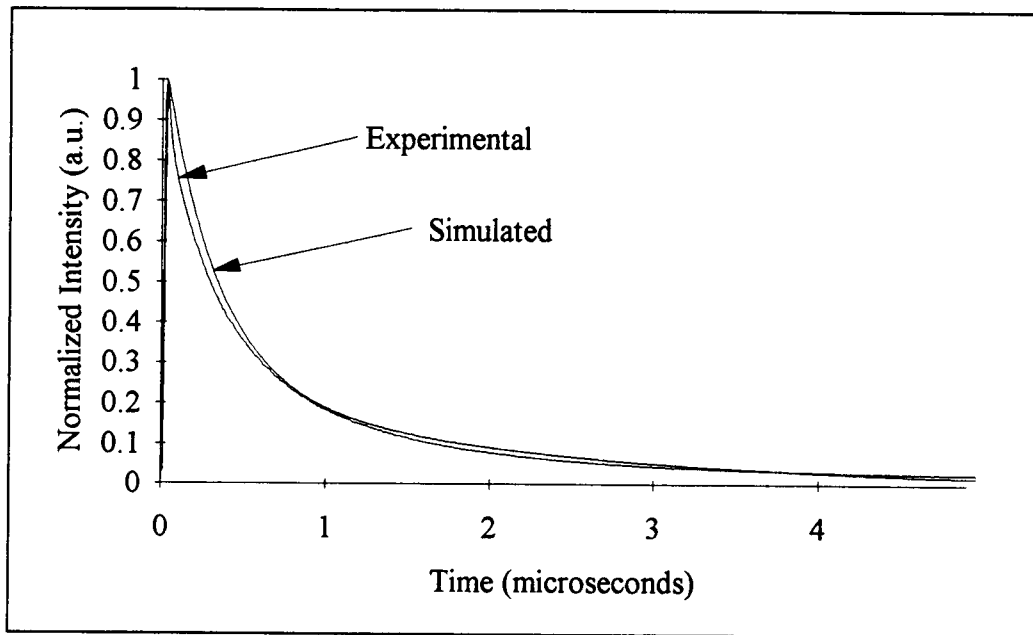


Figure 3-11. Experimental and simulated intensity transient.

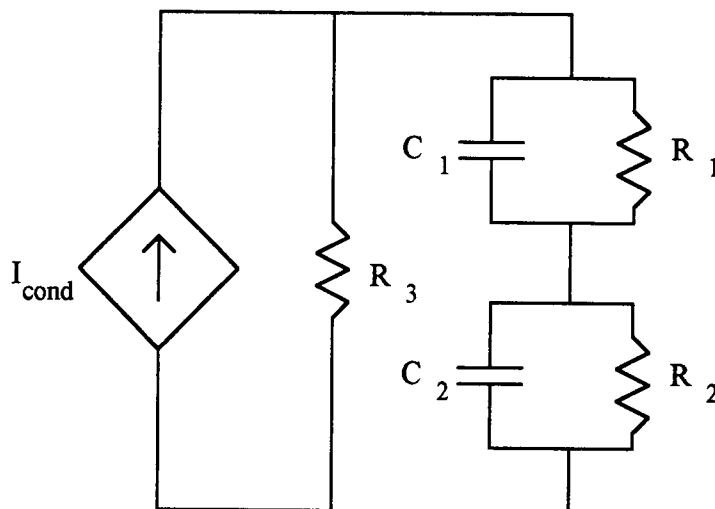


Figure 3-12. Optical circuit model.

a conduction current-controlled current source and a pair of parallel resistor/capacitor elements in a Foster configuration to realized the two decay constants. Thus, the current source in the optical circuit is identical to the conduction current which flows in  $R_d$  of the electrical circuit. The resistor-capacitor branches in the optical circuit model the two decay constants and the optical intensity is taken as proportional to the absolute value of

Circuit Element	Value
R1	433 Ohms
R2	206 Ohms
C1	4.2 $\mu$ F
C2	1.5 $\mu$ F
R3	1.0 Mohms
Current Gain	1.0

Figure 3-13. Optical circuit parameters.

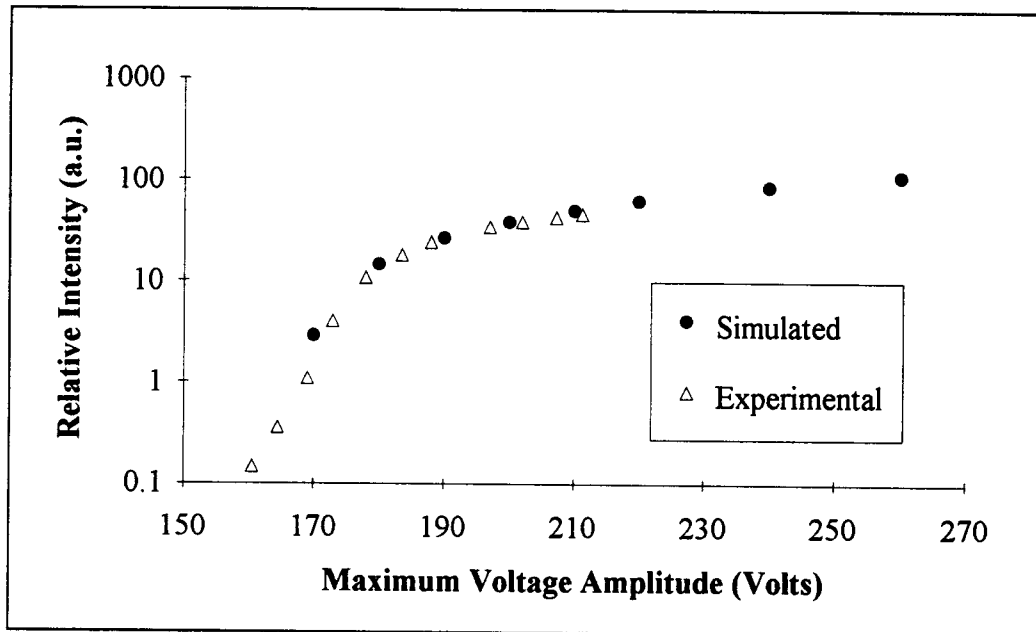


Figure 3-14. Experimental and simulated B-V curves.

the current through  $R_3$ . This circuit is therefore simulated at the same time as the electrical circuit. The circuit element values used in the optical simulation are shown in Fig. 3-13. Finally, Fig. 3-14 illustrates the brightness-voltage (B-V) or equivalently intensity-voltage characteristics predicted by this optical model. There is extremely good agreement above the threshold voltage of 170 V. The curves deviate below threshold because actual ACTFEL subthreshold characteristics are not as abrupt as modeled by the back-to-back diodes.

### 3.6 Discussion/Summary

Both of the models presented in this chapter are derived from engineering intuition or fitting techniques. Although this seems somewhat unscientific, it is argued that since the goal is to develop an accurate equivalent circuit for device modeling, any path which leads to the desired goal is acceptable. The electrical circuit was arrived at by carefully studying the components of the electric field and conduction charge transients. The key observation is the presence of relaxation charge. This charge arises from continued charge transport across the phosphor, in the same direction as the main conduction charge, after the external voltage derivative goes to zero. A capacitive discharge phenomena seems like a reasonable way to account for this kind of effect, thus the new circuit elements  $R_T$  and  $C_T$ .

Trends in ACTFEL device electrical response to variations in the applied waveform are measured, explained, and simulated. The greatest impact upon device performance is due to changes in pulse amplitude. Pulse width variation is of secondary importance and rise/fall time variations have no effect. The response due to amplitude variation is attributed to the requirement that field-clamping occurs in evaporated SiON devices. Pulse width dependence is attributed to modulation of the time for relaxation charge to reach a steady-state value. A revised equivalent circuit is presented which accounts for relaxation charge and, therefore, accurately models the device dynamics as well as trends due to variations in the applied waveform. Finally, the electrical model is

augmented by an optical circuit. Simulated brightness transient and B-V curves from the optical circuit are in excellent agreement with experimental data.

## **4.0 PHOSPHOR SPACE CHARGE/DEVICE PHYSICS MODEL**

### **4.1 Introduction**

In the device physics assessment of ACTFEL devices, it is usually assumed<sup>1,13,19-20</sup> that the electric field is constant across the phosphor layer; this implies that no net space charge exists within the bulk portion of the phosphor layer. Although this assumption is almost universally employed, its validity has been questioned by numerous researchers<sup>1,13,18-28</sup>.

Most discussions of space charge in ACTFEL devices have focused on explaining the mechanism responsible for hysteresis in B-V curves<sup>21-26</sup>. B-V hysteresis is found to occur in ACTFEL devices when the Mn concentration exceeds about 0.5%<sup>24</sup>. Models accounting for B-V hysteresis invoke<sup>21-24</sup> the existence of positive space charge in the ZnS phosphor due to hole trapping or impact ionization of deep levels within the ZnS bandgap. Although atomic identification of this positive space charge has never been clearly established, the existing evidence suggests<sup>22,24</sup> that it is related to Mn and probably due to Mn clustering.

Recently, evidence has been offered<sup>27-28</sup> for the existence of space charge in non-hysteretic, ALE ZnS:Mn ACTFEL devices. This conclusion is reached from a scaling analysis of the conduction current with respect to frequency. The purpose of this chapter is to provide supporting evidence for the existence of bulk space charge in ALE-grown ZnS:Mn ACTFEL devices as deduced from electrical and optical measurements at low temperature and to present a revised electrostatic model which includes space charge effects.

### **4.2 Experimental Technique**

The ZnS:Mn ACTFEL devices measured in this work are fabricated by ALE in the typical stack configuration in which the ZnS:Mn phosphor layer is sandwiched between two ATO insulating layers. Figure 4-1 illustrates, the similarity to the evaporated device structure shown in Fig. 2-1.

The ACTFEL device is driven using an arbitrary waveform generator (Analogic model 2020) in conjunction with a high voltage operational amplifier (Apex model PA85) to obtain alternating bipolar pulses with amplitudes of magnitude 160 V, pulse width of

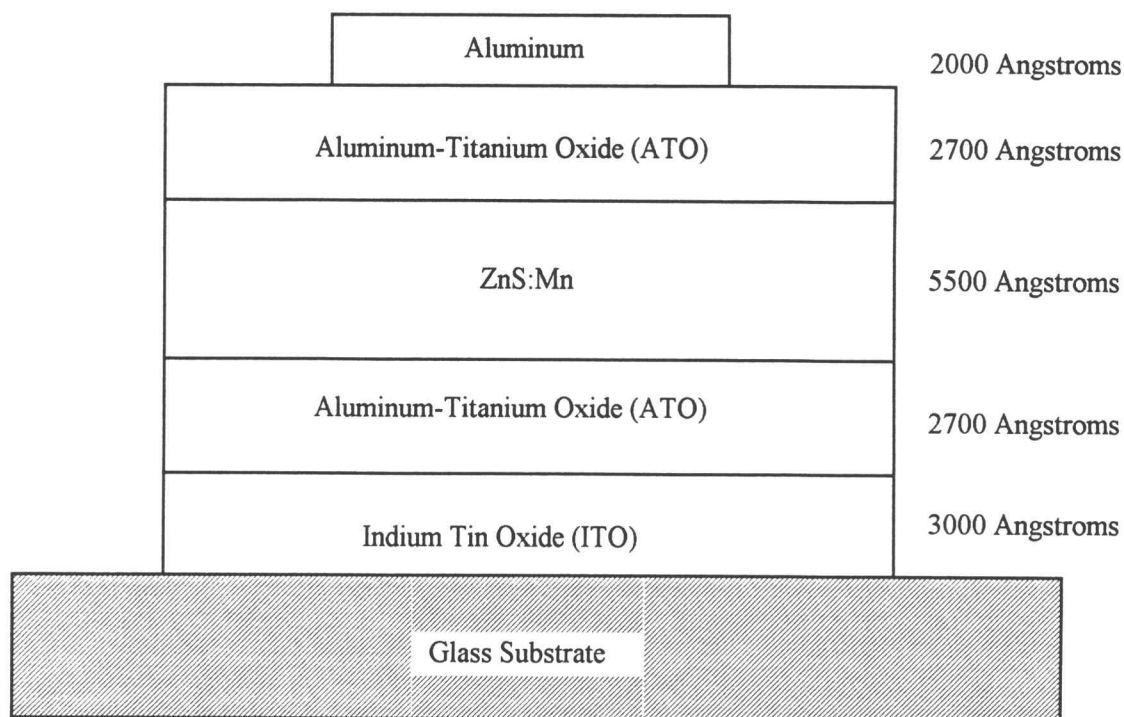


Figure 4-1. ALE ACTFEL device structure.

80  $\mu$ s, a rise/fall time of 30  $\mu$ s, and a frequency of 100 Hz. Electrical characterization is accomplished using a digitizing oscilloscope (Tektronix model 11402) to monitor the voltage across the ACTFEL device and a Sawyer-Tower<sup>11</sup> capacitor as mentioned in Sec. 2-4. The current is monitored using a current probe (Tektronix model A6302 with an AM503 current probe amplifier).

Time-resolved luminescence spectra are measured using a SPEX 3/4 meter monochromator and a cooled, extended range photomultiplier tube (PMT). Spectra are obtained by digitally acquiring the voltage across a resistor between the PMT and ground. A single-system correction to the raw data is performed which accounts for the lenses, grating, and detector. The complete experimental set-up is shown in the Fig. 4-2.

### 4.3 Experimental Results

The voltage and current transients for an ACTFEL device at room temperature are given in Fig. 4-3. During the initial rising edge of the voltage pulse, the device behaves as a capacitive stack and all of the measured current is displacement current. Once the amplitude of the voltage becomes sufficiently large, electrons at the phosphor/insulator interface begin to emit and conduction current flows across the phosphor layer; this is referred to this as the primary conduction current. During the falling edge of the voltage pulse the device appears as a capacitive stack once again and the measured current is exclusively displacement current.

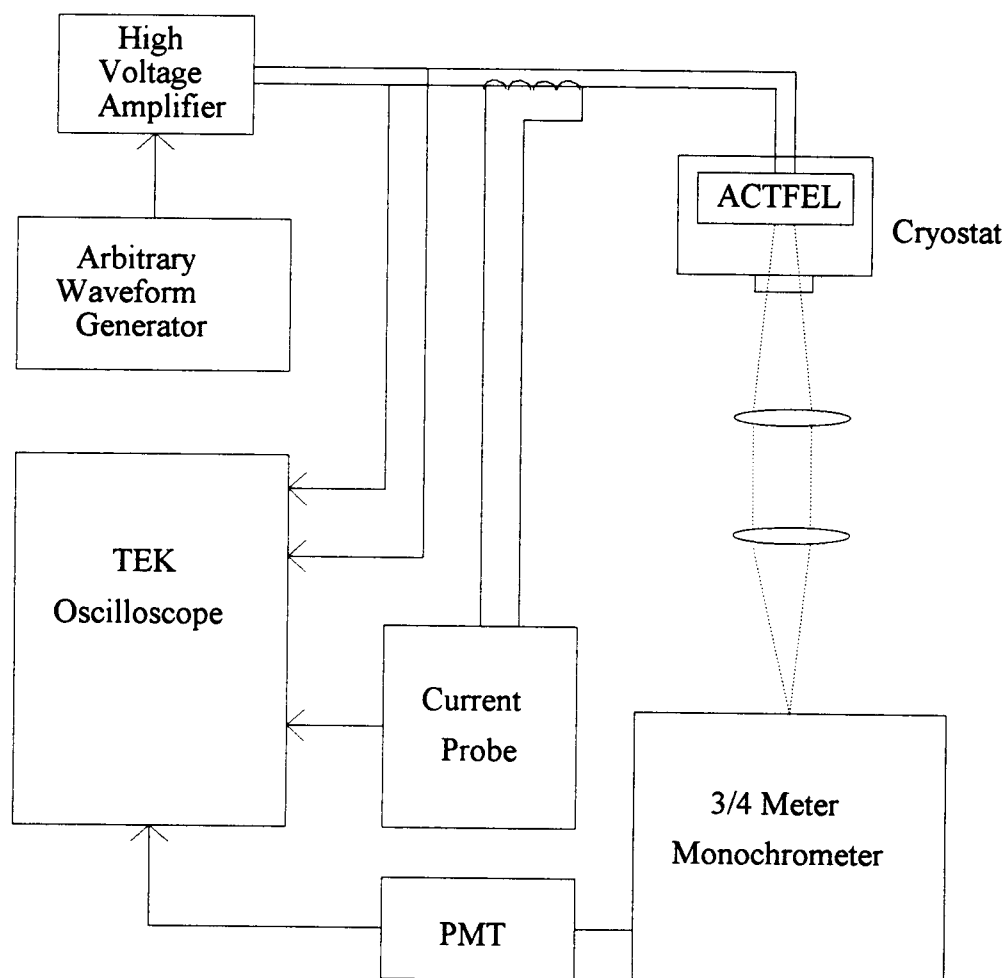


Figure 4-2. Experimental set-up.

As shown in Fig. 4-4, at low temperatures two additional current peaks, subsequently referred to as secondary conduction current, are observed during the falling edge of the voltage pulse. Using a bridge circuit<sup>12</sup> to balance out the displacement current below threshold, these secondary current peaks are confirmed to arise from conduction current which flows in the opposite direction of the primary current. These secondary current peaks are found to occur only during the falling edge of a negative pulse applied to the Al electrode.

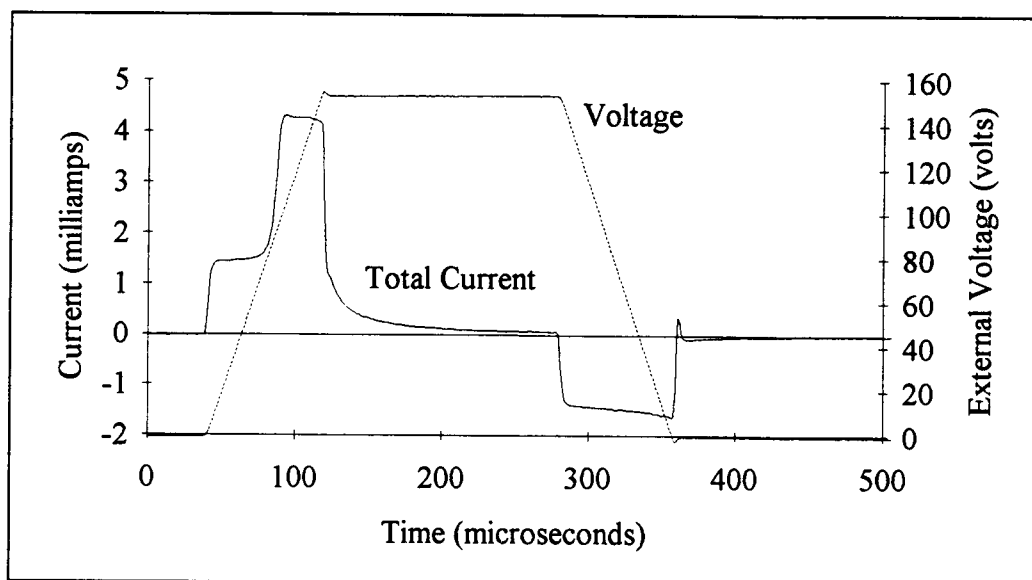


Figure 4-3. Voltage and field transients at room temperature.

Additionally, with increasing temperature the magnitude of these secondary current peaks decreases and they shift in time closer to the initial transition of the voltage pulse, as shown in Fig. 4-5. Note that in Fig. 4-5 the current waveform of Fig. 4-4 is inverted and focuses on the secondary current peaks which occur between 250  $\mu$ s to 400  $\mu$ s.

The appearance of secondary current, as manifest by these two current peaks, is correlated with changes in the shape of the primary conduction current. Notice in Fig. 4-4, the top portion of the conduction current is essentially flat at 275 K whereas at low



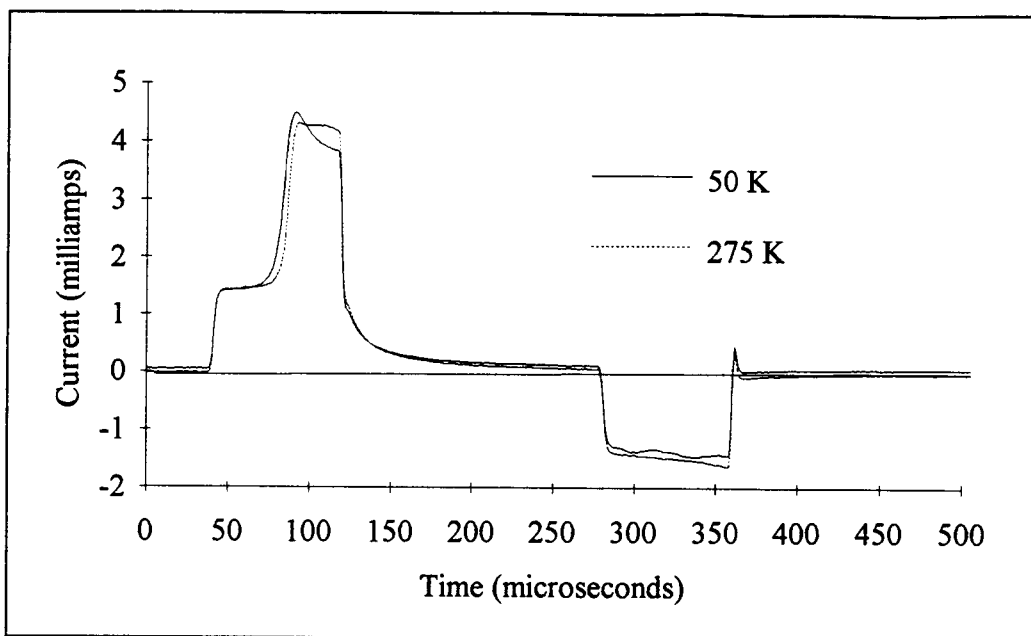


Figure 4-4. Current transients at low and room temperature.

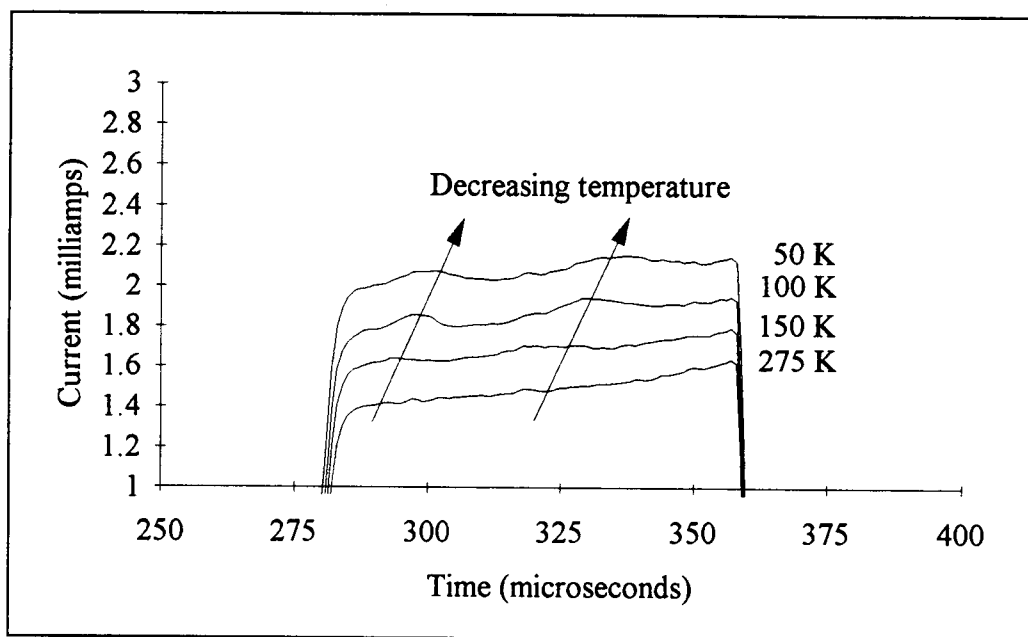


Figure 4-5. Secondary current peaks shift with changing temperature.

temperature, this portion of the current waveform is peaked. Keep in mind that the same external voltage waveform is applied to the same device for both low and high temperatures. Focusing once again on the differences in the main conduction current, a change in the onset of conduction or equivalently a change in the turn-on voltage is

observed. Also, the top portion of the conduction currents should be the same amplitude at  $120\mu\text{s}$ . These two differences lead to the conclusion that the insulator capacitance of the ACTFEL device is a function of temperature, as demonstrated by the shift in the onset of conduction. Even if it is assumed that this is true, it does not account for the peak shape of the conduction current at low temperature. If the change in capacitance is taken into account, it is found that this extra peak is superimposed upon the flat portion of the primary conduction current.

In order to further investigate the nature of the secondary current peaks, time-resolved luminescence measurements are performed. Figure 4-6 displays the luminescence transient at a wavelength of 460 nm and the electric field transient at a temperature of 50 K. The first intensity peak, labeled main emission, is concomitant with the flow of primary conduction current (during field clamping) and the second emission peak, labeled secondary emission, occurs during the falling edge of the voltage waveform during which

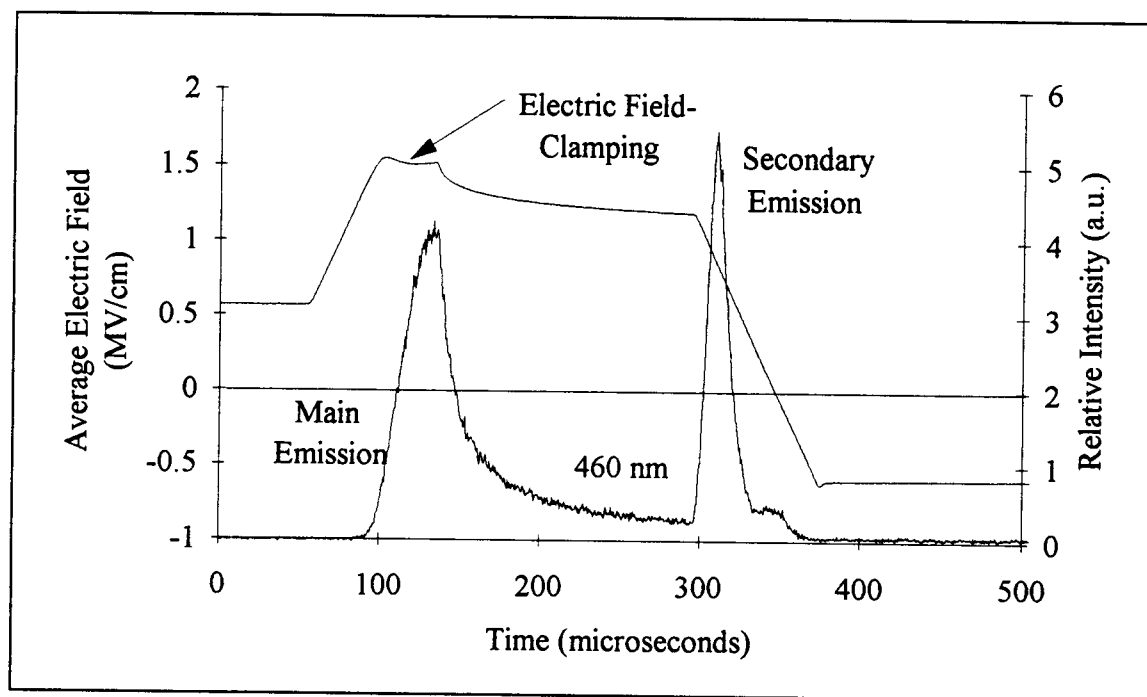


Figure 4-6. Time-resolved luminescence and electric field.

the secondary conduction current peaks are found. This is a very important observation. Notice that the secondary light peak occurs before the average electric field changes sign. If they occurred at the same time, one could explain this as electrons rushing back across the phosphor as the field changes signs. This is the most important piece of evidence supporting the conclusion that space charge is present in the phosphor.

The low temperature luminescence spectra corresponding to the time integral of the primary and secondary emissions in Fig. 4-6 are given for both voltage polarities in Fig. 4-7. The legend indicates the electrode polarity of the emission intensity; the negative electrode is used since it corresponds to the interface from which electrons are emitted. Note that secondary emission is measured for both polarities even though secondary current peaks are observed only when the Al electrode is negatively biased. It is believed that secondary current flows for both polarities but that it is below the detection limit when the ITO electrode is negatively biased; this is consistent with the fact that as the

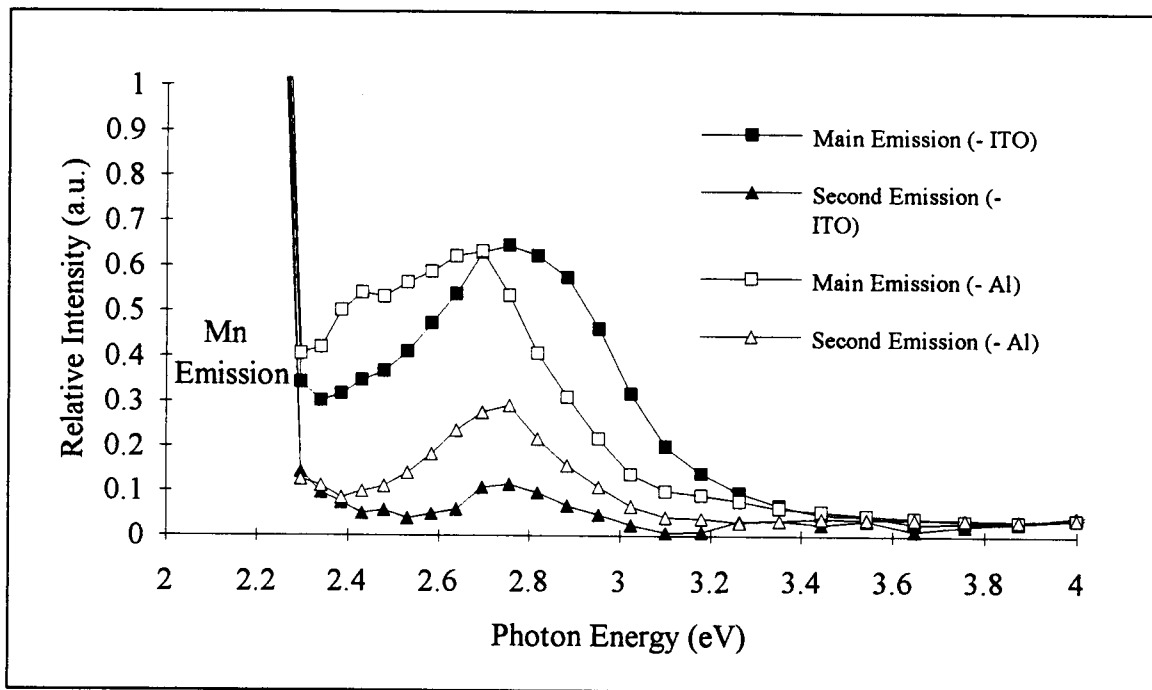


Figure 4-7. Emission spectra.

applied bias is ramped towards threshold, light in the ACTFEL device is always detected prior to the onset of measurable conduction current.

Although there are differences in the spectra shown in Fig. 4-7, the similar shape and peak energy, 2.7 eV, is striking. Thus, the primary and secondary blue emission at 2.7 eV = 460 nm, associated with both voltage polarities is attributed to the same physical process, as discussed later. Having emphasized the similarities between the spectra of Fig. 4-7, note that there are also certain differences in the primary spectra. Since the spectra occur concomitant with the flow of conduction current, these differences are attributed to differences in the distribution of hot electrons giving rise to the measured blue emission. This assertion implies that the electron distribution is hotter when the ITO electrode is biased negatively. This hotter distribution is consistent with the observation that the phosphor clamping field (actually, this should probably be referred to as a pseudo-clamping field since ALE devices do not exhibit hard field-clamping) at the onset of primary conduction current is greater when the ITO electrode is negatively biased.

#### 4.4 Discussion

In this section a model is proposed which explains all of the observations noted in the experimental results section. It is shown that the experimental results can only be explained by assuming the existence of space charge in the phosphor layer.

Begin by assuming that the space charge can be modeled as a thin sheet of charge somewhere inside the phosphor. The following is a summary of the various quantities defined by Fig. 4-8,

$V_{\text{ext}}$  = External voltage applied to the device.

$I_1, I_2$  = Insulators

$P_1, P_2$  = Phosphor layer on either side of the space charge.

$F$  = Electric field (subscript indicates the region where the field exists)

$d_s$  = Position of the space charge measured from the left interface at  $x = 0$ .

$d$  = Film thickness' (subscript indicates the region)

- $Q_a$  = Charge residing at the left interface.  
 $Q_b$  = Space charge.  
 $Q_c$  = Charge residing at the right interface.

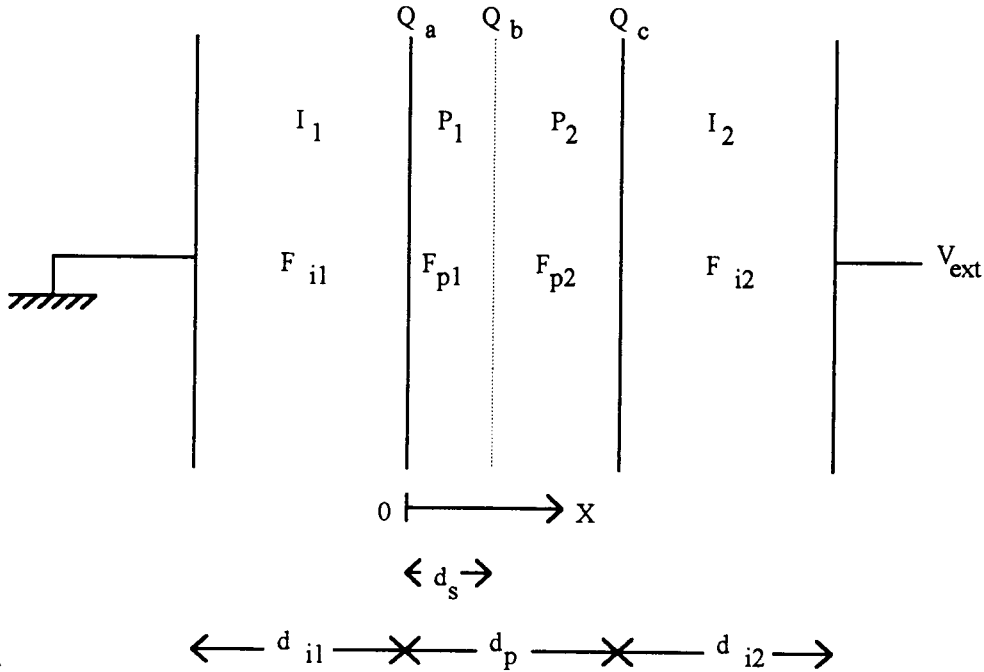


Figure 4-8. Device definitions to account for space charge.

All charges are assumed to be positive quantities. The derivation of the internal field in each region of the phosphor begins with the electrostatic boundary conditions,

$$\hat{x} \cdot (\vec{D}_{n1} - \vec{D}_{n2}) = -\rho_s \quad (4-1)$$

where  $\hat{x}$  is the unit normal vector at the interface,  $D_{n1}$  and  $D_{n2}$  are electric field densities, and  $\rho_s$  is the surface charge density. In terms of the dielectric constant or permittivity of the thin-films,

$$\epsilon_{n1} F_{n1} - \epsilon_{n2} F_{n2} = -\frac{Q}{A}. \quad (4-2)$$

Now, considering each of the sheets of charge,

$$\epsilon_{i1}F_{i1} - \epsilon_p F_{p2} = -\frac{Q_a}{A} \quad (4-3a)$$

$$\epsilon_p F_{p1} - \epsilon_p F_{p2} = -\frac{Q_b}{A} \quad (4-3b)$$

$$\epsilon_p F_{p2} - \epsilon_{i2}F_{i2} = -\frac{Q_c}{A}. \quad (4-3c)$$

Also, from Kirchoff's Voltage Law,

$$-V_{\text{ext}} = V_{i1} + V_{p1} + V_{p2} + V_{i2} \quad (4-4)$$

and therefore,

$$-V_{\text{ext}} = F_{i1}d_{i1} + F_{p1}d_s + F_{p2}(d_p - d_s) + F_{i2}d_{i2}. \quad (4-5)$$

Note that the negative sign is included to conform with the convention originally established by Bringuier<sup>1</sup>. Substitution, of Eqn. 4-3 into Eqn. 4-4, leads to a system of four equations and four unknowns. However, first solve for  $F_{p1}$  by substitution to obtain,

$$-V_{\text{ext}} = -\frac{d_{i1}}{\epsilon_{i1}} \frac{Q_a}{A} + F_{p1} \left( d_s + \frac{d_{i1}}{\epsilon_{i1}} \epsilon_p \right) + \left( \frac{Q_b}{\epsilon_p A} + F_{p1} \right) \left[ (d_p - d_s) + \frac{d_{i1}}{\epsilon_{i2}} \epsilon_p \right] + \frac{d_{i2} Q_c}{\epsilon_{i2} A}. \quad (4-6)$$

Collecting terms and solving for  $F_{p1}$  leads to,

$$F_{p1} = \frac{1}{d_p} \left[ \frac{-2C_i V_{\text{ext}} + Q_a - Q_c}{2(C_i + C_p)} \right] - \frac{1}{d_p} \left[ \frac{2Q_b C_i \left( \frac{1}{C_p} - \frac{1}{C_s} + \frac{1}{C_i} \right)}{2(C_i + C_p)} \right] \quad (4-7)$$

where the capacitances are given by,

$$C = \frac{\epsilon A}{d} \quad (4-8)$$

with the appropriate permittivities and thickness. Equation 4-3b leads directly to

$$F_{p2} = F_{p1} + \frac{Q_b}{\epsilon_p A}. \quad (4-9)$$

$F_{i1}$  and  $F_{i2}$  can easily be determined from Eqn. 4-3a and Eqn. 4-3c. Finally, the average electric field across the phosphor is given by,

$$F_{ave} = \frac{1}{d_p} \left[ \int_0^{d_s} F_{p1} dx + \int_{d_s}^{d_p} F_{p2} dx \right] = F_{p1} + \frac{Q_b}{\epsilon_p A} \left( 1 - \frac{d_s}{d_p} \right). \quad (4-10)$$

Note that Eqn. 4-7 and Eqn. 2-3 given by Bringuier<sup>1</sup> are identical if  $Q_b$  goes to zero or  $d_s$  goes to  $d_p$ . If  $Q_b$  goes to zero,  $Q_a = -Q_c$ . This results in the cycle of energy band diagrams given in Fig. 2-2. However, if space charge is present in the phosphor and one assumes a delta function spatial distribution, the phosphor field will have two different values on either side of the sheet of charge. For completeness an expression for conduction current assuming interface a is emitting charge is included,

$$i_{cond} = \frac{dQ_a}{dt} = \frac{dQ_b}{dt} + \frac{dQ_c}{dt} \quad (4-11)$$

and once again a reminder to the reader that all charge is assumed to be positive. Also, note that in this calculation  $Q_b$  accumulates at the expense of  $Q_c$ .

Consider the case where interface a is net negatively charged and interface b is net positively charged (i.e. depleted of electrons with respect to flat band) and the external voltage and the space charge is zero. The internal field is,

$$F_p = \frac{1}{d_p} \left[ \frac{-Q_a - Q_c}{2(C_i + C_p)} \right] = \frac{1}{d} \left( \frac{-|Q_a|}{(C_i + C_p)} \right) \quad (4-12)$$

and the energy band diagram would appear as shown in Fig. 4-9. If positive space charge

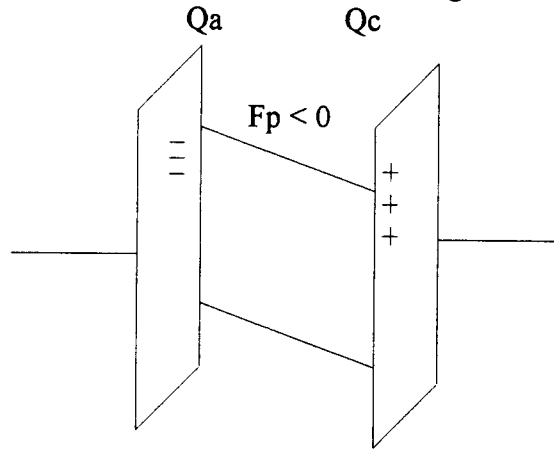


Figure 4-9. Energy band diagram with no space charge and no external bias.

is included, the energy band diagram is bent as indicated in Fig. 4-10. Notice that a negative field already exists, and the addition of positive space charge, increases the magnitude of the field in  $F_{p1}$  and decreases the magnitude of the field in  $F_{p2}$ .

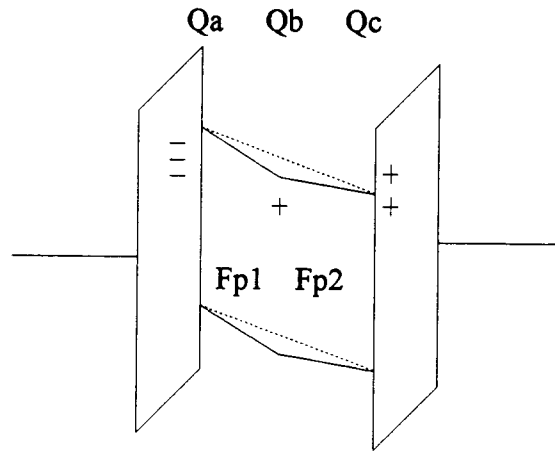


Figure 4-10. Energy band diagram with space charge and no external bias.

This model is now used to explain all of the experimental results of the previous section. The unexpected observations at low temperature are;

- 1) The main conduction current has a peaked shape instead of being flat.
- 2) Two new "secondary" current peaks appear and their polarity is opposite to that of the main conduction current.
- 3) The first secondary peak emits 2.7 eV light, but the second secondary peak does not.
- 4) Both the current peaks and the emission have a greater magnitude when the aluminum electrode is biased negatively.
- 5) The light is centered at 2.7 eV.
- 6) The new current and light emission is thermally quenched.
- 7) The secondary current peaks occur at earlier times as the temperature is increased.



To explain all of these observations, a steady-state energy band diagram cycle including space charge is presented in Fig. 4-11. Each of these energy band diagrams is discussed in detail and related to one of the experimental observations listed above.

As an arbitrary starting position, consider Fig. 4-11a in the upper righthand corner of Fig. 4-11. In this case, there is no external bias, no space charge ( $Q_b=0$ ), and an internal field established by the polarization charge ( $Q_a=-Q_c$ ).

Figure 4-11b shows the application of a positive voltage,  $V_{ext}$ , to the ITO electrode. This bends the conduction band further (i.e. the external field constructively adds to the internal field).

Next, proceed to Fig. 4-11c which shows tunnel injection of electrons from the right interface (Al side) and the formation of space charge by impact ionization of states within the bandgap. This leads to a multiplication effect (i.e. one electron is emitted from the right interface and two electrons are collected at the left interface). This explains why the main conduction current has an additional peak (observation #1 and Fig. 4-4). Note that in this case the field starts with a positive magnitude and, in contrast to Figs. 4-9 and 4-10, the field is reduced in region p1 and increased in region p2.

As the voltage pulse begins to decrease in Fig. 4-11d (i.e.  $V_{ext}$  becomes less negative), the field in region p1 changes sign. As this occurs, electrons at the left interface rush back and neutralize the space charge. This recombination results in the emission of light with a wavelength of 460 nm. This explains the first of the secondary current peaks, and the corresponding emission of light (observation #2).

As the voltage pulse continues to decrease, the space charge is completely neutralized and electrons in shallow interface states flow back to the left interface. This is shown in Fig. 4-11e. It is this phenomena that gives rise to the second secondary current peak and explains why it does not emit the same intense spectrum as the first secondary peak (observation #3 and Fig. 4-6). Note that in Fig. 4-11c that main conduction current flows to the right (i.e. the electrons move to the left) and the the secondary current peaks,

shown in Figs. 4-11d and 4-11e, flow in the opposite direction as required by the observations.

At this time, the voltage pulse returns to zero. Notice that Fig. 4-11f corresponds to the initial diagram given in Fig. 4-11a with the opposite charge state.

Finally, Fig. 4-11g shows the application of a voltage pulse of the opposite polarity to the ITO electrode and the corresponding injection from the left interface (ITO side). These injected electrons, however, do not impact ionize bulk states and, therefore, do not form space charge or emit light during recombination. This can be attributed to the fact that the bulk states responsible for space charge occur predominately on the ITO side of the phosphor layer (observation #4).

Now, consider the fact that the emission is peaked at 2.7 eV and thermally quenched (observation #5). Mikami et al.<sup>30</sup> have performed photoluminescence (PL) spectra measurements of ZnS:Mn layers grown by halide-transport chemical vapor deposition. Specifically, Mikami et al. observe a strong blue PL emission with a peak at 460 nm (2.7 eV) which exhibits thermal quenching by a factor of 1/3 upon raising the temperature from 77 to 300K. This is very similar to the experimental observation #5. Mikami et al. attribute this emission to radiative recombination from shallow chlorine donors on a sulfur site,  $\text{Cl}_\text{S}$ , to a deep acceptor state identified as a zinc vacancy,  $\text{V}_{\text{Zn}}$ . It is interesting to note that the secondary current peaks and corresponding light emission are not observed in evaporated ACTFEL devices which do not use Cl during processing. This seems to imply that Cl is crucial for the formation of space charge. The ionization energy of  $\text{Cl}_\text{S}$  is reported<sup>35</sup> to be about 0.1-0.3 eV which places the  $\text{V}_{\text{Zn}}$  level at about 0.6 eV above the ZnS valence band maximum,  $E_\text{V}$ . This level is probably due to the second acceptor state of the  $\text{V}_{\text{Zn}}$  which has been crudely estimated<sup>34</sup> to be located about 1.5 eV above  $E_\text{V}$ . This is summarized in Fig. 4-12.

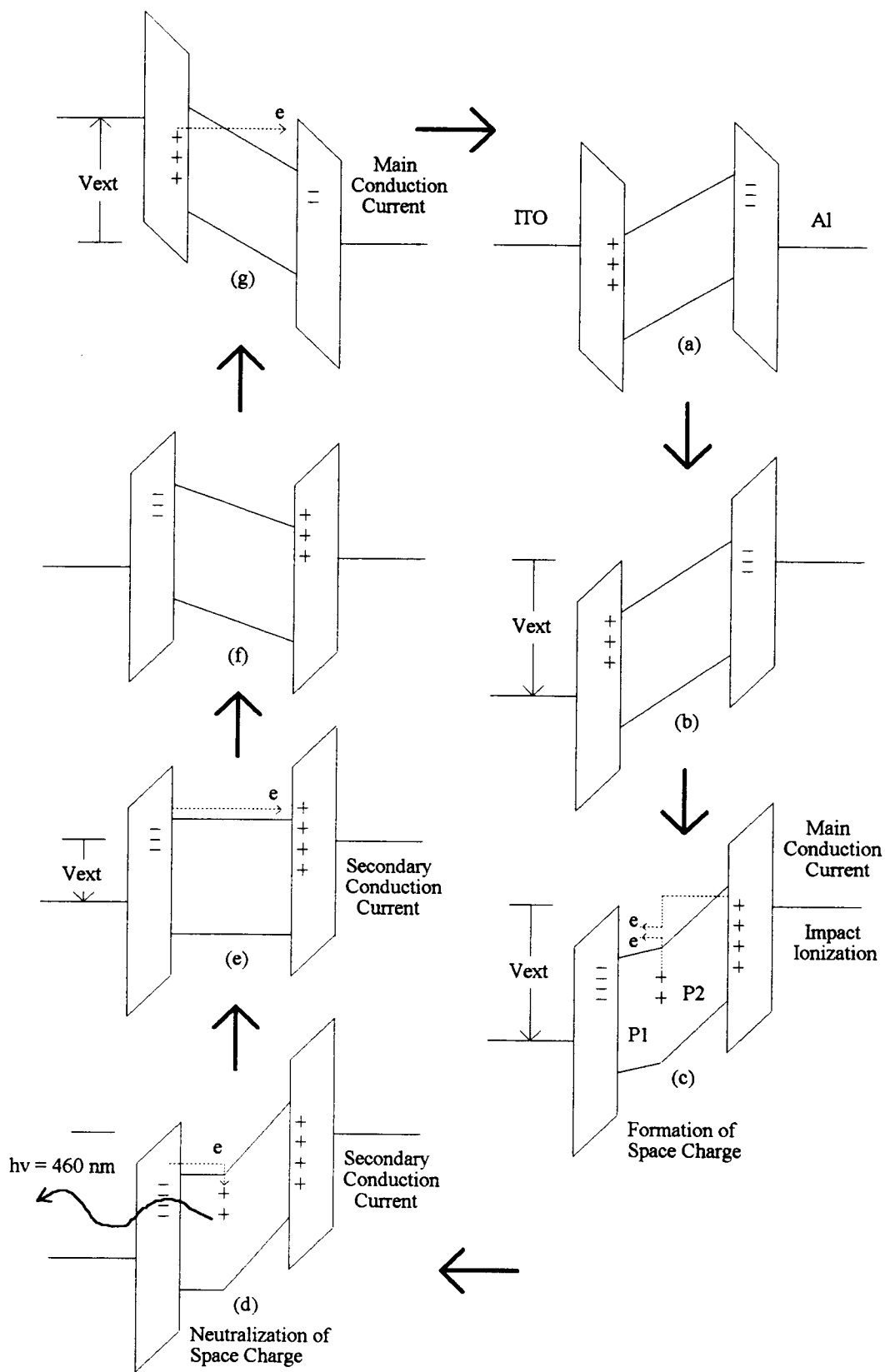


Figure 4-11. Energy band diagram cycle with space charge.

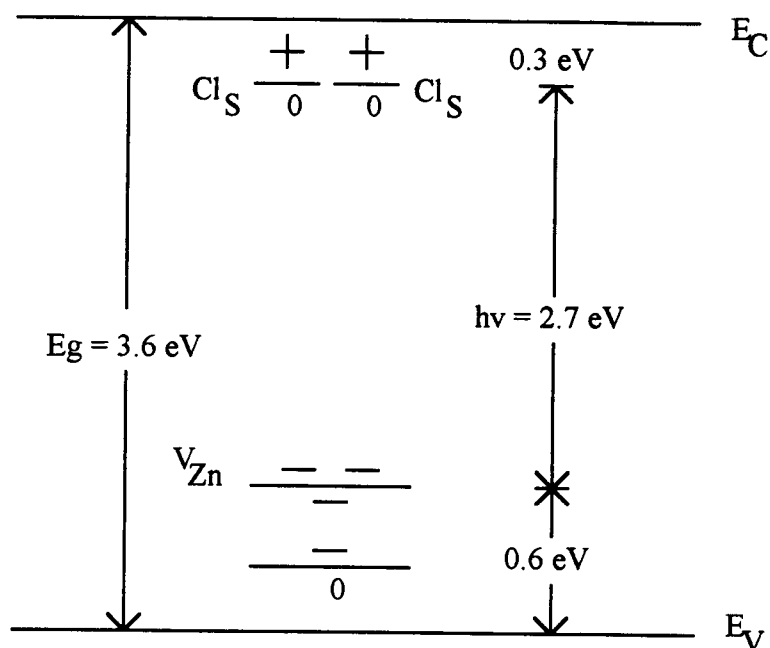
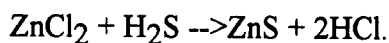


Figure 4-12. Energy states associated with the formation of space charge.

With these considerations in mind, the process of forming space charge, shown in Fig. 4-11c, is explained as follows. Main conduction electrons impact ionize zinc vacancies which reside approximately 0.6 eV from the valence band edge. This leaves the pair of Cl atoms and the zinc vacancy net positively charged. Some of the main conduction electrons recombine. In the recombination process the electrons are first trapped by Cl atoms, and then radiatively decay into the ionized zinc vacancies, thus neutralizing one unit of space charge. This radiative recombination process results in the 2.7 eV emission observed when the main conduction current flows. When Al is negatively biased, not all of the space charge is neutralized by the main conduction current; some space charge remains until the falling edge of the voltage pulse. As the voltage is reduced during the falling edge, electrons in shallow interface states flow backwards, see Fig. 4-11d, recombination occurs through Cl atoms, and the space charge is neutralized. This gives rise to the second emission peak at 2.7 eV.

It is believed that Cl is present throughout the phosphor layer as the ALE growth process relies on the following chemical reaction,



However, it is reasonable to assume that there are more zinc vacancies and, in general, more atomic disorder on the first side of the phosphor grown. This agrees with the finding that the space charge occurs predominately on the ITO side of the phosphor which is the first grown.

The presence of two energy states in the band gap explains why the emission is sharply peaked at 2.7 eV (observation #5). If there is only one state for recombination, the emission would be broad since the initial state of the recombining electrons would be spread over all available states in the conduction band.

The thermal quenching of this phenomena agrees with observations<sup>30</sup> by Mikami et al.; this thermal quenching phenomena is believed to be due to the fact that the probability of impact ionization increases with decreasing temperature (observation #6). Another possible explanation, although very unlikely, is related to the depopulation of the Cl state with thermal energy. In this case the electrons would be re-excited to the conduction band before recombination with the zinc vacancy occurs.

The most difficult observation to explain is #7. This relates to the shift in time of the secondary current peaks as seen in Fig. 4-5. To understand this phenomena, return to the theoretical model for space charge discussed above. The average phosphor electric field and its components, given by Eqns. 4-7, 4-9, and 4-10, (assuming 10 % of the conducted charge results is space charge), are plotted in Fig. 4-13. First note that the field is constant across the phosphor thickness until conduction current begins to flow at approximately 75 $\mu$ s. With the initiation of conduction current the field splits into two components; this field-splitting is due to the formation of space charge. Note that positive space charge causes  $F_{p1}$ , the field on the ITO side of the phosphor, to become less than the average field and  $F_{p2}$ , the field on the Al side of the phosphor, to become larger than

the average field. Notice that the  $F_{p1}$  curve crosses through zero prior to  $F_{p2}$ . This is very important as the  $F_{p1}$  crossing occurs when the first of the two secondary current peaks appears; this corresponds to the energy band diagram of Fig. 4-11d. When  $F_{p1}$

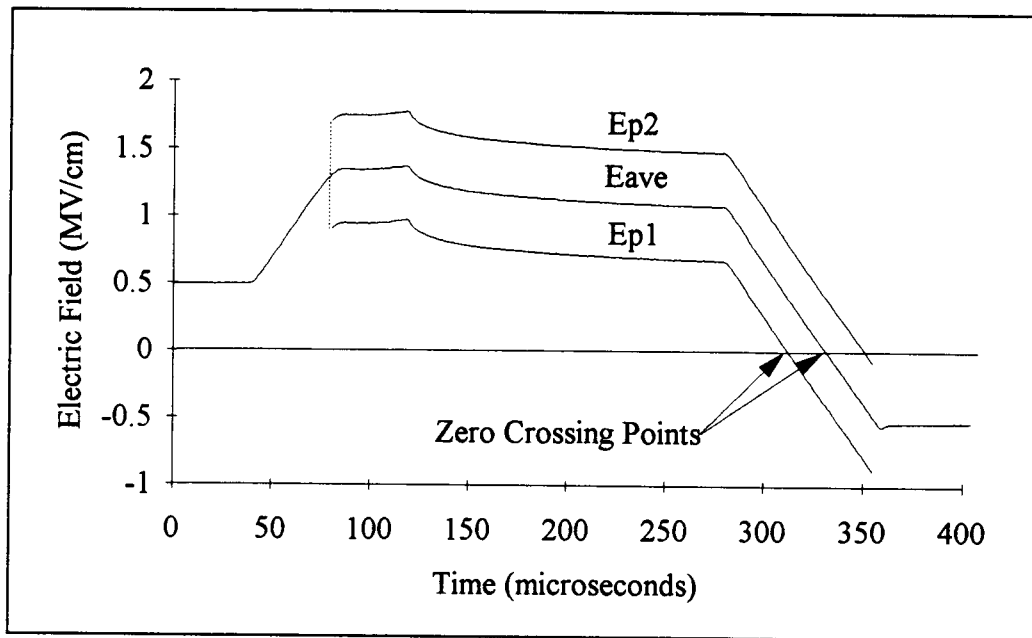


Figure 4-13. Electric field transients.

crosses zero, the space charge begins to be neutralized and both field components,  $F_{p1}$  and  $F_{p2}$ , converge back to one uniform field equal to  $F_{ave}$ . The second secondary current peak occurs when  $F_{ave}$  reaches the zero crossing point; this corresponds to Fig. 4-11e. Note that the amount of spread between  $F_{p1}$  and  $F_{p2}$  is proportional to the amount of space charge present in the phosphor. Therefore, if the amount of space charge increases,  $F_{p1}$  shifts to lower field values and its zero crossing point occurs at earlier times. This is precisely the reason why the current peaks shift in time at various temperatures (see Fig. 4-5). Apparently, lowering the temperature allows a significant amount of space charge to form in the phosphor. As the temperature is lowered more space charge is formed,  $F_{p1}$  shifts to lower field values, and the corresponding current peaks shift to earlier times. Also, note that the amplitude of the secondary peaks increase as the temperature is

lowered. This is consistent with the notion of an inverse relationship between the amount of space charge and temperature. This explains observation #7.

#### **4.5 Summary**

In this chapter the results of an experiment that confirms the presence of space charge in ALE ACTFEL devices operated at low temperatures is reported. The temperature dependence is attributed to the fact that space charge forms by impact ionization and that the probability of impact ionization increases as the temperature is lowered. The presence of space charge at low temperature yields two new current peaks superimposed on the room temperature current waveform. The first of the two new peaks is found to emit 2.7 eV photons while the second does not. The first peak is attributed to the radiative neutralization of space charge. The space charge is believed to originate from impact ionization of Zn vacancies. Electrostatic calculations accounting for the device response assuming a sheet of space charge are consistent with experimental observations. Finally, it is concluded that the space charge exists predominately on the ITO side of the phosphor which is the first grown side.

## 5.0 INTERFACE STATE DISTRIBUTION/DEVICE PHYSICS MODEL

### 5.1 Introduction

In this chapter an experimental technique for assessing the distribution of interface states in ACTFEL devices is presented. Interface states are energy states which are distributed throughout the bandgap and are physically localized at the phosphor/insulator interface. Knowledge of their distribution in energy is critical since these are the states which inject conduction current electrons into the phosphor. Knowledge of the interface state distribution could be very useful in assessing the origin of device aging and asymmetry, and could be valuable for interface-engineering and device optimization. Also, the interface state distribution is one of the greatest uncertainties in Bringuier's device physics model<sup>1</sup>.

### 5.2 Theory

First, recall that during normal device operation electrons are injected into the phosphor conduction band and excite luminescent impurities during transport. Electron emission from interface states may occur by one of three different mechanisms,

- 1) thermal emission,
- 2) phonon assisted tunneling, or
- 3) pure tunneling.

These mechanisms are shown pictorially in Fig. 5-1 along with a possible interface state distribution in which the states are occupied up to the quasi-Fermi level,  $E_{qf}$ . For an electron to reach the conduction band, it must either surmount the potential barrier established by the bandgap of the phosphor or tunnel through the barrier. Notice in Fig. 5-1 that the top of the barrier is drawn as a curve rather than the more typical triangle. This barrier height lowering phenomena, known as the Frenkel-Poole effect, arises from the high electric field in the phosphor. The amount by which the barrier is lowered,  $\Delta E$ , is given by,<sup>35</sup>



$$\Delta E = \left[ \frac{qF_p}{\pi\epsilon_p} \right]^{1/2} \quad (5-1)$$

where  $F_p$  is the phosphor field and  $\epsilon_p$  is the permittivity of the phosphor. For example, if the electric field is 1.5 MV/cm and the relative permittivity of ZnS is 8.3,  $\Delta E = 0.32$  eV. This barrier lowering can be very significant in the emission rate equations as  $\Delta E$  often occurs in exponentials.

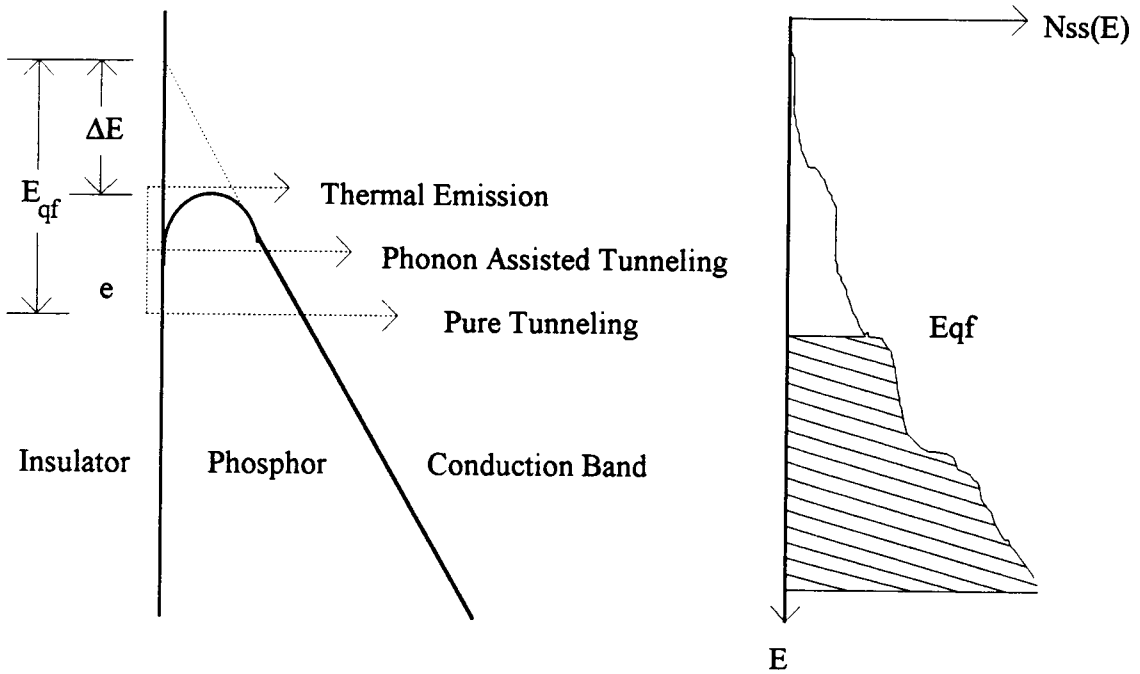


Figure 5-1. Emission mechanisms.

Thermal emission is a process whereby an electron in an interface state gains energy from the thermal energy of lattice vibrations (phonons) which is sufficient to allow the electron to surmount the barrier. This emission rate, including barrier height lowering, is given by<sup>36</sup>,

$$e_n(\text{Thermal}) = \sigma v_{th} N_c \exp\left(-\frac{E_{qf} - \Delta E}{kT}\right) \quad (5-2)$$

where  $k$  is Boltzmann's constant,  $T$  is the temperature in degrees Kelvin,  $\sigma$  is the capture

cross section,  $N_c$  is the effective density of states, and  $v_{th}$  is the thermal velocity.

Phonon assisted tunneling is a two-step process in which an electron gains energy from phonons, although not enough energy to surmount the barrier. The energy barrier seen by an energetic electron is effectively reduced and the electron tunnels through the reduced barrier into the conduction band. The phonon assisted tunneling emission rate,  $e_n(PAT)$ , is given by<sup>36</sup>,

$$e_n(PAT) = e_n(Thermal) \int \exp \left[ z - z^{3/2} \left( \frac{8\pi (m^*)^{1/2} (kT)^{3/2}}{3 qhF_p} \right) \left( 1 - \left( \frac{\Delta E}{zkT} \right)^{5/3} \right) \right] dz \quad (5-3)$$

where  $e_n(Thermal)$  is the thermal emission rate given by Eqn. 5-2,  $h$  is Plank's constant,  $m^*$  is the effective mass of an electron, and  $z$  is the normalized energy,

$$z = \frac{E_{qf}}{kT}. \quad (5-4)$$

Finally, the pure tunneling mechanism is due to direct electron tunneling from interface states to the conduction band. This emission rate is given by<sup>36</sup>,

$$e_n(PT) = \frac{qF_p}{4(2m^*E_{qf})^{1/2}} \exp \left[ \left( -\frac{8\pi (2m^*)^{1/2} E_{qf}^{3/2}}{3 qhF_p} \right) \left( 1 - \left( \frac{\Delta E}{E_{qf}} \right)^{5/3} \right) \right]. \quad (5-5)$$

The sum of all three mechanisms gives the total emission rate,

$$e_n(Total) = e_n(Thermal) + e_n(PAT) + e_n(PT). \quad (5-6)$$

In addition to understanding the mechanisms for electron injection into the conduction band, it is important to determine how the quasi-Fermi level,  $E_{qf}$ , changes as a function of time. The distribution of electrons at the phosphor/insulator interface is described by an occupancy function. In equilibrium semiconductor physics, this function is called the Fermi-Dirac distribution function and the Fermi level is the energy at which the probability of an electron having that energy is 1/2. In the case of an ACTFEL device the Fermi-level is called a quasi-Fermi level. This is due to the fact that the distribution function,  $f(E)$ , is no longer "Fermi-Dirac"-like and changes as a function of time. The

nonequilibrium distribution function is given by the differential equation<sup>1</sup>,

$$\frac{\partial f(E)}{\partial t} = -e_n(\text{Total})f(E). \quad (5-7)$$

The general solution is<sup>1</sup>,

$$f(E, t) = f_0(E) \exp \left[ - \int_0^t e_n(\text{Total}) dt' \right]. \quad (5-8)$$

where  $f_0(E)$  is the initial distribution function at  $t=0$ . The time evolution of the electric field is given by Eqn. 2-3 in terms of the externally measured charge or in terms of the internal or conduction charge as,

$$F_p(t) = - \frac{1}{d_p(C_i + C_p)} [C_i V_{\text{ext}}(t) - Q_{\text{int}}(t)] \quad (5-9)$$

or, in terms of the occupancy function  $f(E)$ ,

$$F_p(t) = - \frac{1}{d_p(C_i + C_p)} \left[ C_i V_{\text{ext}}(t) - q \int_{E_v}^{E_c} N_{ss}(E) [f_0(E) - f(E, t)] dE \right]. \quad (5-10)$$

Note that the second term in the outer brackets is actually the transferred conduction charge,  $Q_{\text{int}}(t)$ , in Eqn. 5-9. If the occupancy function  $f(E)$  is assumed to be close enough to a step function, the limits of integration in Eqn. 5-10 can be changed as follows,

$$Q_{\text{int}}(t) = \int_{E_{fb}}^{E_{cf}(t)} q N_{ss}(E) dE \quad (5-11)$$

where  $E_{fb}$  is the quasi-Fermi level at flat-band. Flat-band is the condition shown in Fig. 2-2a where both phosphor/insulator interfaces are neutral.

To summarize, Eqns. 5-8 and 5-10 comprise a set of coupled differential equations. This system can be solved by assuming a step function for  $f(E)$  and a single discrete trap level for  $N_{ss}(E)$ <sup>1</sup>. In the more general case, the system of differential equations becomes extremely difficult and would in general require a numerical solution.

The technique for measuring interface states is based on an observation that allows one to unravel this very complicated set of equations. The observation is based on Eqn. 5-8 and the equations that describe the emission rates, Eqns. 5-2 through 5-6. First, notice that the only time dependence in the emission rates is implied through the electric field dependence. Furthermore, if the electric field is a constant, the total emission rate is independent of time and can be removed from the integral in Eqn. 5-8 as follows,

$$f(E, t) = f_0(E) \exp[-e_n(\text{Total}) \cdot t]. \quad (5-12)$$

Assuming that the field is held constant and that pure tunneling is the dominant emission mechanism, Eqn. 5-12 is plotted at different times. Notice how fast the initial

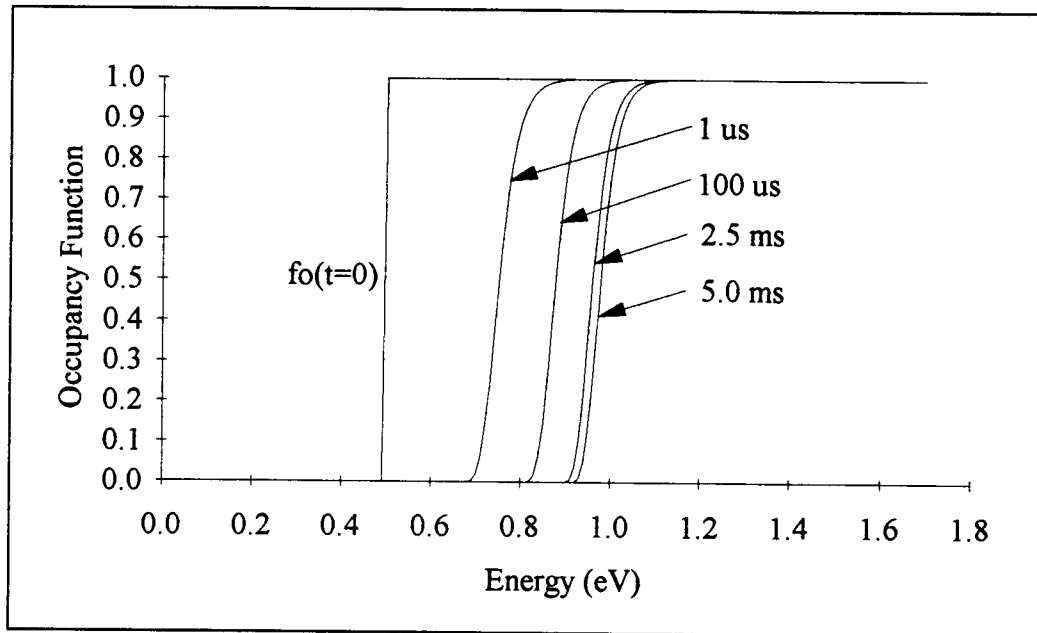


Figure 5-2. Time evolution of the occupancy function at 1.5 MV/cm.

occupancy function,  $f_0$ , changes. The occupancy function at  $t > 0$  is not a Fermi-Dirac function; in fact, the function is not even temperature-dependent (assuming emission occurs exclusively by pure tunneling). The occupancy function is determined exclusively by the electric field strength. Another interesting point is that independent of whatever initial distribution is assumed, e.g.  $f_0$  is assumed to be a step function at 0.5 eV in the

present case, it is immediately distorted by the electric field, as shown in Fig. 5-2. Finally, note that after 5 ms the occupancy function begins to reach steady-state. This means that the probability of any electrons deeper than 0.95 eV being emitted in less than 5 ms is very low. In Fig. 5-3 the occupancy function is plotted after 5 ms (steady-state) under a constant field, again assuming that emission occurs exclusively by pure tunneling. This figure illustrates how far the function moves through the bandgap for different constant field magnitudes after 5 ms.

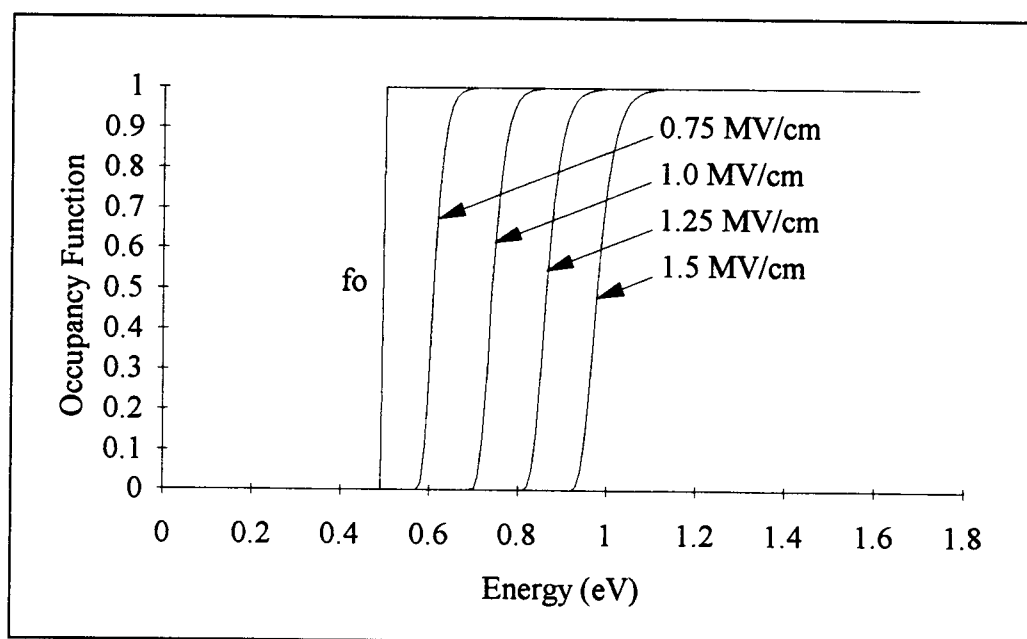


Figure 5-3. Occupancy function after 5 ms at given field strengths.

The previous discussion provides the key for understanding how the interface state distribution is measured. If the phosphor field is held constant at a given value long enough for the system to reach steady state ( $\sim 5$  ms), the maximum depth in energy from which charge is emitted can be determined from Eqn. 5-12, as shown in Fig. 5-3. Then, by stepping the electric field from low to high values, the interface state distribution can be assessed through differentiation of Eqn. 5-11. This gives,

$$N_{ss}(E_{qf}(t_{ss})) = \frac{1}{q} \frac{dQ_{int}(t_{ss})}{dE} \quad (5-13)$$

where  $t_{ss}$  is the time to reach steady-state and  $E_{qf}(t_{ss})$  is the position of the quasi-Fermi level at  $t_{ss}$ . In Fig. 5-3,  $E_{qf}(t_{ss})$  corresponds to the point where  $f(E)$  equals 1/2.

Most ACTFEL models that consider the occupancy function assume that it is a step function. A step function occupancy assumes that all states above  $E_{qf}$  are empty, while all states below  $E_{qf}$  are filled. A step function occupancy can be shown to be an excellent assumption by evaluating the derivative of  $f(E)$ , as indicated in Fig. 5-4, to access the width of the energy transition between filled and empty states. Note from Fig. 5-4 that  $E_{qf}$  corresponds to the peak in these curves and that the FWHM is approximately 0.1 eV or less and that it does not change significantly with the field strength; this demonstrates the validity of the step function approximation under a constant phosphor field.

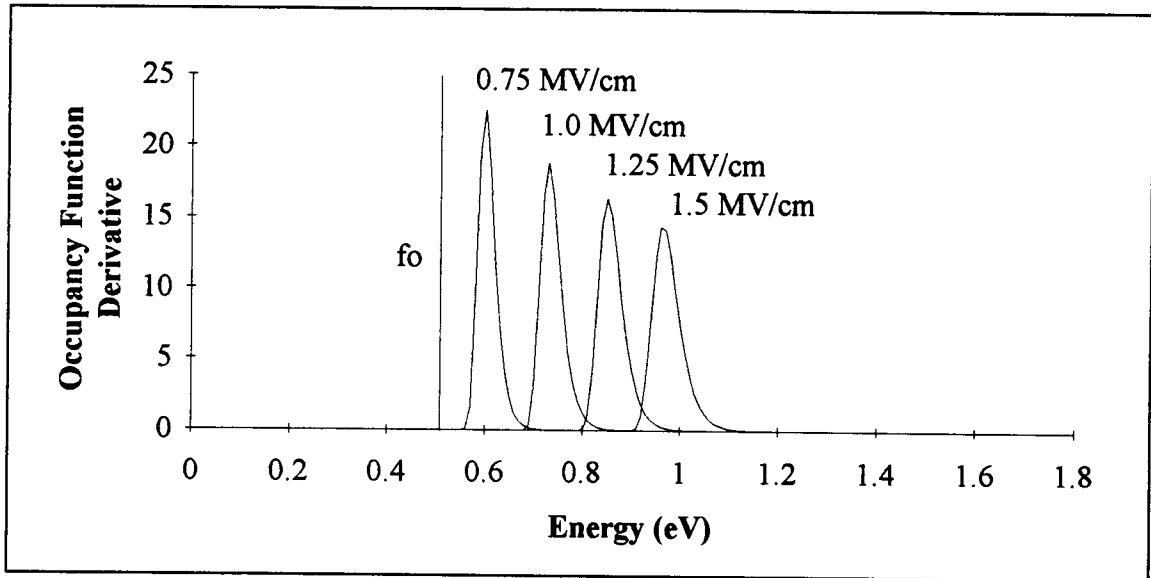


Figure 5-4. Spread of the occupancy function after 5 ms at various fields.

In summary, it has been shown that if the electric field in the phosphor is held at a constant value for approximately 5 ms, the quasi-Fermi level,  $E_{qf}$ , reaches steady-state,

and all states above  $E_{qf}$  are depopulated to within an accuracy of 0.1 eV. This suggests that the interface state density may be assessed if the transferred charge is measured as the field is stepped from low to high values and held constant at each field for 5 ms to allow steady-state to be attained. The maximum emission energy,  $E_{qf}(t_{ss})$ , from which all the charge at a given field strength is emitted is given by Eqn. 5-12. With each increasing magnitude of the field, the increase in the total amount of emitted charge is attributed to the increased depth at which  $E_{qf}$  saturates. This is illustrated in Fig. 5-5. If field  $E_1$  is held constant for 5 ms, all electrons above  $E_{qf}(1)$  are emitted. Then, if the field is increased to  $E_2$ , all electrons above  $E_{qf}(2)$  are emitted. Of course this assumes that there are electrons in the interface states to be emitted; this means that some initial polarization charge is present before the field can be set to a constant.

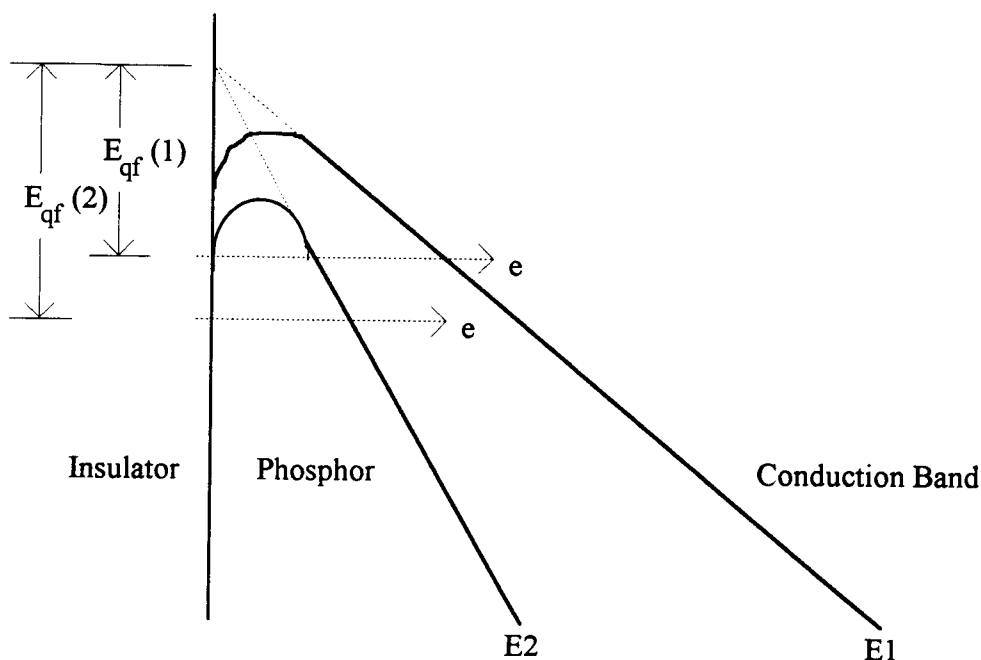


Figure 5-5. Emission at various field strengths.

Maintaining a constant field is very difficult because, as shown in Chapter 2 and 4, the electric field has two contributions, one due to the externally applied voltage and one

due to the internal polarization charge. As charge is emitted from interface states, the internal field changes. This internal feedback effect associated with the emission of interface charge leads to charge emission under a variable field condition. However, a technique to force the internal field to a constant value has been developed, as discussed in the next section.

### 5.3 Experimental Technique

The ability to measure interface state density hinges on being able to accurately hold the electric field at a constant value for a given duration. Consider the equation for the phosphor electric field which is given in terms of the charge measured externally by a Sawyer-Tower<sup>11</sup> capacitor and the external applied voltage,

$$F_p = \frac{1}{d_p} \left( \frac{Q_{st}}{C_i} - V_{ext} \right). \quad (5-14)$$

Rearranging this equation yields,

$$V_{ext} = \frac{C_{st}}{C_i} \left( V_{st} - \frac{C_i}{C_{st}} d_p F_p \right) \quad (5-15)$$

where  $Q_{st} = C_{st} V_{st}$ . If  $F_p$  is set to a constant, Eqn. 5-15 prescribes how  $V_{ext}(t)$  must change in response to the measured value of  $V_{st}(t)$  in order to insure that  $F_p$  is indeed constant. Therefore, the equation that needs to be implemented in order to maintain a constant phosphor field is,

$$V_{ext}(t) = G(V_{st}(t) - V_{dc}) \quad (5-16)$$

where  $G$  is the gain, given by  $C_{st}/C_i$ , and  $V_{dc}$  is a dc voltage corresponding to the constant value of the field. The experimental set-up used to realized this is shown in Fig. 5-6.

The experimental set-up shown in Fig. 5-6 periodically forces the phosphor electric field to a constant value during a portion of the driving waveform. Both the arbitrary waveform generators are synchronized. The upper generator creates the standard waveform, shown in Fig. 5-7, with a frequency of 100 Hz. This signal is amplified by the high voltage amplifier which in turn drives the ACTFEL device. The lower generator runs



at one-tenth the frequency of the upper generator (i.e. 10 Hz) and generates a field-control pulse which controls the position of the analog switch (i.e. during the field-control pulse the switch is closed) . Note that the duration of the field-control pulse is approximately

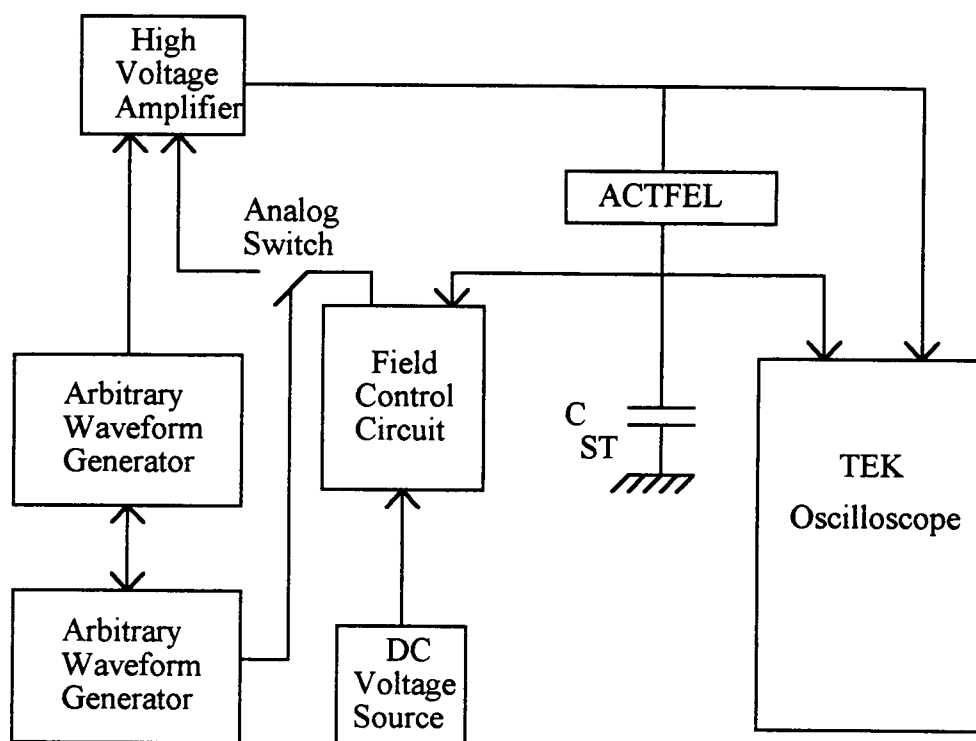


Figure 5-6. Field-control experimental set-up.

half a period of the standard 100 Hz waveform. It is therefore,  $1/200$  seconds or 5 ms as required to reach steady-state, as discussed in the previous section. The field-control waveform generator operates at  $1/10$  of the standard waveform frequency to insure that the device is allowed to re-establish steady-state with the standard waveform prior to the application of the subsequent field-control pulse. Typically, the ACTFEL device can re-establish steady-state with the standard waveform after about 2 complete cycles subsequent to the application of the field-control pulse; 10 cycles are used to insure that steady-state is indeed reached.

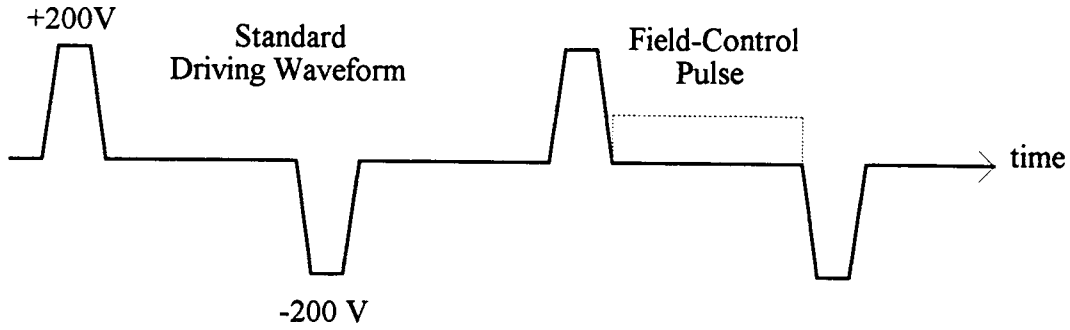


Figure 5-7. Field-control waveforms.

The voltage across the Sawyer-Tower<sup>11</sup> capacitor,  $V_{st}(t)$ , and the external voltage across the device,  $V_{ext}(t)$ , are monitored with a digital oscilloscope. The Sawyer-Tower capacitor is typically very large (50 nF) compared to the total capacitance of the device. This ensures that there is very little voltage dropped across  $C_{st}$ . Note the  $V_{st}(t)$  is fed into the field-control circuit which synthesizes Eqn. 5-16. This circuit compensates for changes in the internal electric field due to the emission of charge from the interface states by changing the externally applied voltage. In effect, the internal feedback caused by the redistribution of transferred charge is canceled out by the external feedback of the circuit. The dc source is used to set the desired phosphor field in the ACTFEL device.

The field-control circuit is illustrated in Fig. 5-8. Both the dc voltage supply and  $V_{st}$  are buffered with op-amps.  $V_{st}$  is buffered to ensure that no charge leaks off  $C_{st}$ , as the input impedance of the op-amp is very large. Both inputs are brought together in a summing node and are fed into a low-gain inverting amplifier. When the analog switch is closed, the total closed-loop gain is the product of the gains of the low-gain inverting amp and the high voltage amp. This gain is variable since it depends on the insulator capacitance of the device as indicated by the  $G$  factor in Eqn. 5-16.

The procedure for calculating the interface state density as a function of energy is as follows;

- 1) Step the electric field using the field-control circuit from low to high values (i.e. 0.1 to 1.6 MV/cm).

- 2) At each field calculate the total internal charge transferred, Eqn. 2-4, and the maximum depth from which the electrons are emitted, using Eqn.5-12.
- 3) Approximate the derivative of Eqn. 5-13 between each pair of data points with a finite difference equation.

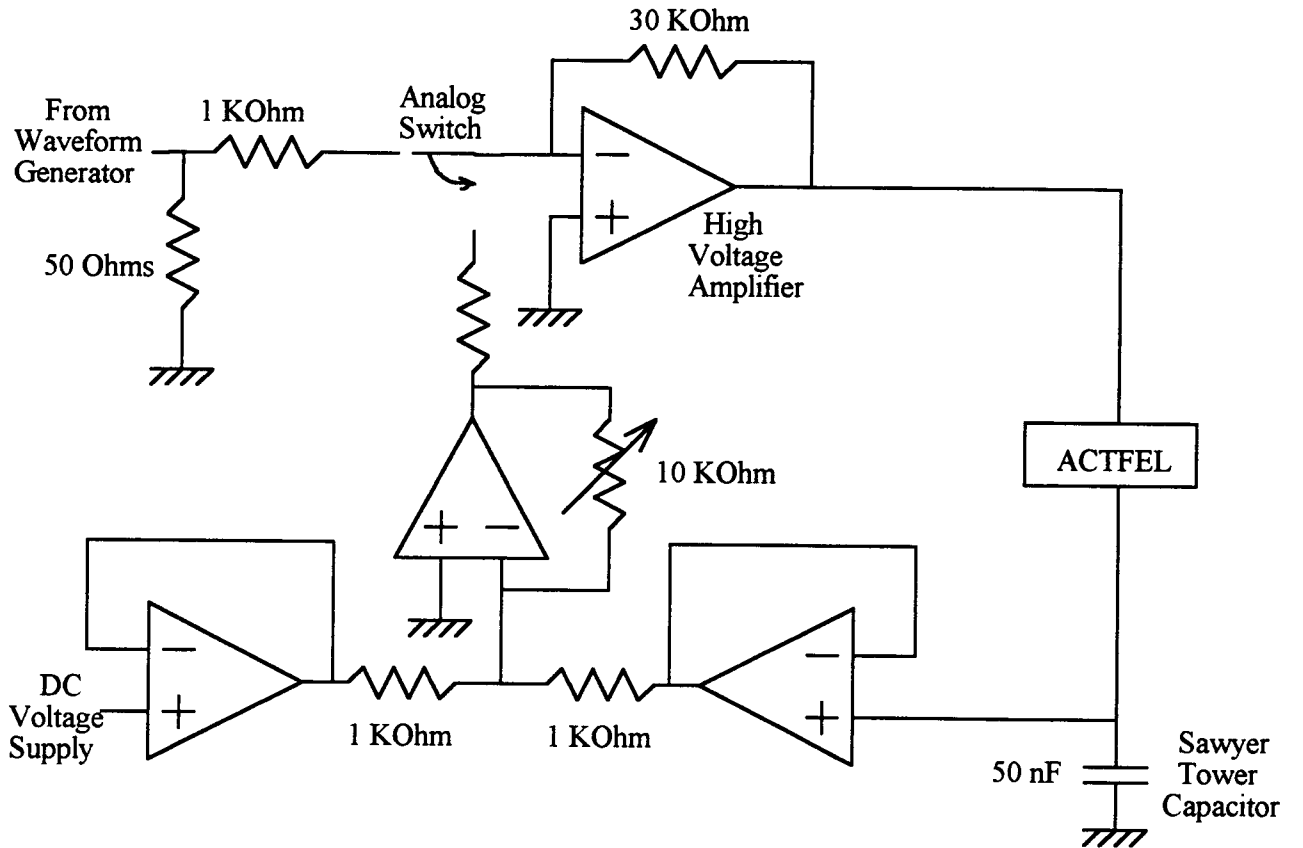


Figure 5-8. Field-control circuit.

The finite difference equation is,

$$N_{ss}(E) \approx \frac{1}{q} \frac{\Delta Q}{\Delta E} = \frac{1}{q} \frac{Q_{ss}(F_{p2}) - Q_{ss}(F_{p1})}{E_{qf}(F_{p2}) - E_{qf}(F_{p1})} \quad (5-18)$$

where

$$Q_{ss}(F_p) = \int_0^{t_{ss}} Q_{int}(t') dt' \quad (5-19)$$

is the total internal charge transferred while the field is held constant across the phosphor for a given field,  $F_p$ , and  $E_{qf}(F_p)$  is the position of the quasi-Fermi level after steady-state is reached (i.e.  $t_{ss}=5$  ms). Note that each value of the differential  $N_{ss}$  is plotted at an energy equal to the average of the two adjacent values of  $E_{qf}$ , i.e.  $[E_{qf}(F_{p2})-E_{qf}(F_{p1})]/2$ . The field steps should be very close in magnitude for the difference equation to be a good approximation to the derivative, but  $\Delta E$  should not be less than 0.1 eV, as indicated by Fig. 5-4.

All of the equations derived thus far have considered pure tunneling to be the exclusive electron emission mechanism. If the interface state measurement is performed at room temperature, it is possible that other emission mechanisms need to be included. Note that the inverse of the total emission rate (pure tunneling + phonon assisted tunneling + thermal emission) is the average time an electron at a given energy spends in an interface state before being injected into the conduction band. By setting the inverse of the emission rate to  $t_{ss}=5$  ms, one can calculate the relationship between the maximum electron emission energy;  $E_{qf}(\max)$ , as a function of the electric field. This relationship is plotted in Fig. 5-9. The main feature to notice is that at room temperature, one of the thermal emission mechanisms could dominate at low electric fields if the capture cross section,  $\sigma$ , is large enough; it will be shown in the next section that this is not the case and that thermal emission mechanisms can be neglected. It is important to note that  $\sigma$  is the only adjustable parameter utilized in the interface state assessment. Additionally, this parameter is only employed for the room temperature measurement while there are no adjustable parameters for the low temperature measurement. Since  $N_{ss}$  is independent of temperature, this approach may be useful for assessing  $\sigma$ .

In summary,  $N_{ss}$  is given by the discrete difference equation, Eqn. 5-18. The transferred charge,  $\Delta Q$ , is calculated from the difference in total charge transferred between two adjacent fields.  $\Delta E$  in the denominator of Eqn. 5-18 is obtained by calculating the difference in the steady-state  $E_{qf}$  between the same two fields. Different

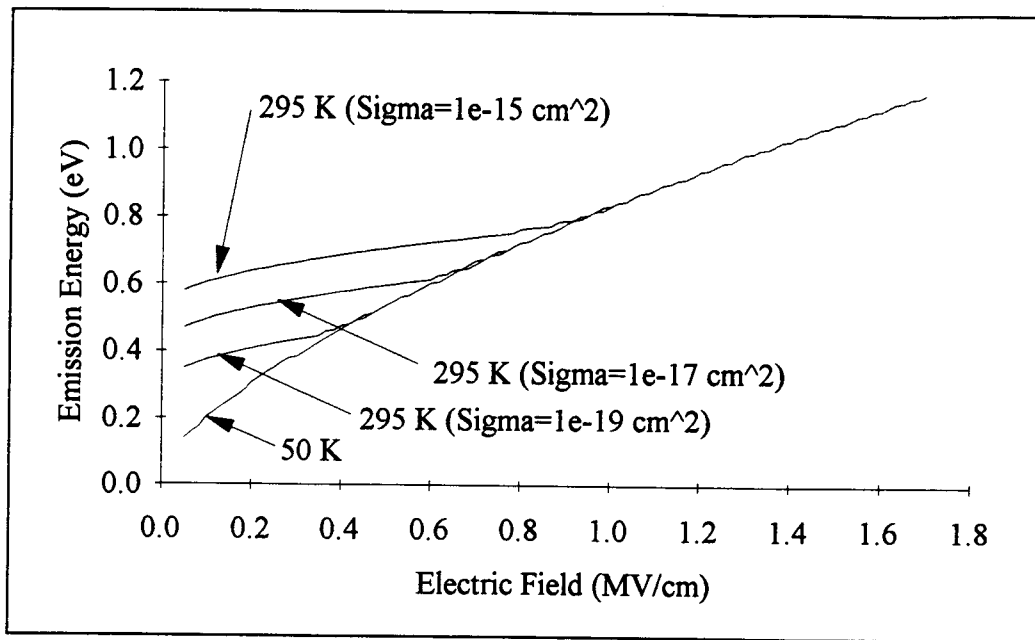


Figure 5-9. Maximum electron emission energy under a constant field for 5 ms.

field values are generated experimentally by discretely changing the phosphor field (from approximately 0.1 to 1.6 MV/cm in steps of 0.1 MV/cm) using the field-control circuit.  $N_{ss}$  is calculated for each pair of phosphor fields and each value of interface state density is plotted at an energy corresponding to the average between the two steady-state values of  $E_{qf}$ .

#### 5.4 Experimental Results

At low temperature, electron emission from interface states occurs exclusively by pure tunneling, whereas at room temperature, thermal emission or phonon-assisted tunneling could presumably play a role, as previously illustrated in Fig. 5-9. The temperature-dependence of the measurement can be understood by plotting  $N_{ss}$  versus energy for the same device at room temperature and at very low temperature (40 K in this case) where all three emission mechanisms are included in Eqn. 5-12. At low temperature pure tunneling is the only significant emission mechanism. Since the  $N_{ss}$  calculation must be temperature-independent,  $\sigma$ , the only variable parameter in the room temperature plot of  $N_{ss}$ , can be adjusted so that both the room and low temperature curves match. For all

devices measured in this work  $\sigma$  is found to be less than  $10^{-20} \text{ cm}^2$  in order to provide agreement between the room and low temperature values of  $N_{ss}$ . This forces the conclusion that the capture cross section is so small that all thermal emission mechanisms are insignificant at room temperature. In retrospect, an extremely small capture cross section is quite reasonable. Traps with this small of a capture cross section are usually assumed to be Coulombically repulsive. In ACTFEL devices, electrons approaching a charged interface would indeed feel an immense amount of Coulombic repulsion due to all of the deeper traps which are filled with electrons.

Figure 5-10 shows the interface state distribution of a standard evaporated ACTFEL device with SiON insulators at room temperature and 40 K. The notation Al + and Al - correspond to the two different interfaces of the ACTFEL device. Al + means that the field-control pulse is asserted immediately following a positive pulse applied to the Al electrode from the driving waveform generator; see Fig. 5-7. Notice that the interfaces, Al + and Al -, are symmetric. The difference between the low and high

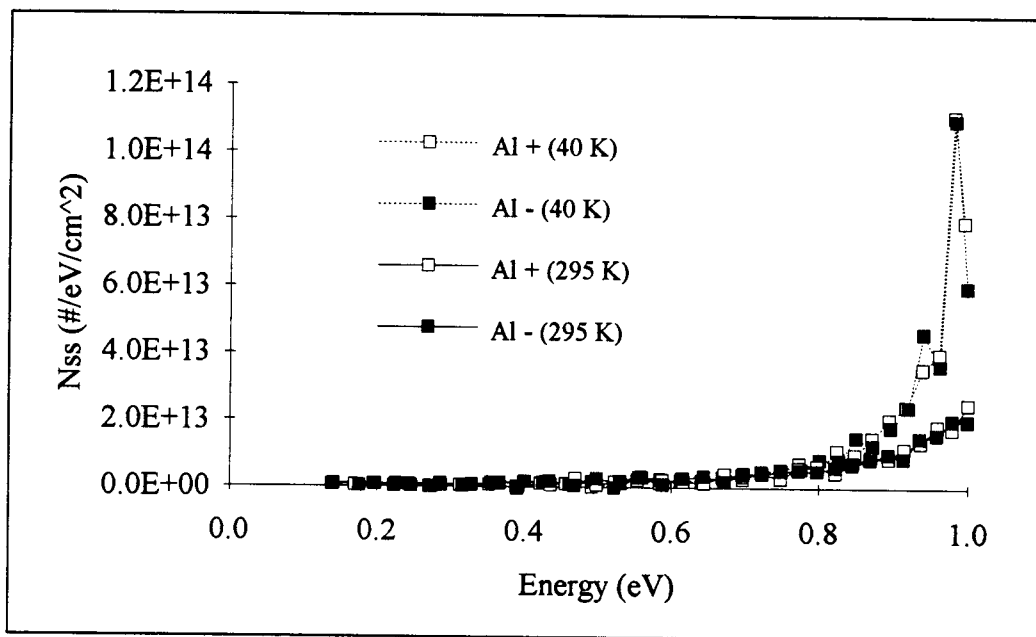


Figure 5-10. Interface state distribution for a SiON ACTFEL device.

temperature curves only occurs at high energy. If this difference were due to a thermal emission mechanism, Fig. 5-9 predicts that this difference would be evident in the low energy portion of the curve. Thus, this high energy difference is attributed to the temperature dependence of the capacitance of the ACTFEL device. This will become more apparent as the driving voltage amplitude dependence is explored.

Figure 5-11 illustrates that a difference in the amplitude of the driving waveform affects the shape of the  $N_{ss}$  plot. This is due to the fact that the amplitude of the driving waveform determines the amount of charge transfer during the pulse; the larger the amplitude, the more charge transferred. The present technique for measuring interface states depends on filling the interface with excess electrons, i.e. polarization charge, and then observing the amount of charge and the depth from which the charge is transferred under a constant field. This means that the interface states must be filled with electrons before the density of interface states can be measured. In the case of Fig. 5-10, the difference between  $N_{ss}$  curves with temperature is attributed to a change in capacitance. A change in capacitance implies that the amount of voltage dropped across the phosphor is different, and therefore the extent to which the states are filled initially is different.

To summarize, it is shown that there is negligible temperature dependence in the emission rate and in the electron distribution at the interface. Any temperature dependence observed in the measurement is due to variations in the insulator and/or phosphor capacitances. This difference in capacitance leads to a difference in the initial occupancy of the interfaces and leads to a difference in the high energy portion of the  $N_{ss}$  plot.

Figure 5-11 shows the transferred charge versus energy for an evaporated ACTFEL device with BTO insulators. The  $N_{ss}$  curve can be calculated by differentiation. Charge versus energy plots yield the same information as an  $N_{ss}$  plot but avoid the problem of the numerical "noise" associated with the differentiation operation. Notice that as the driving voltage amplitude is increased the transferred charge curves shift to lower

energies. This is due to the fact that increasing the voltage increases the amount of charge at the interface (i.e. the initial occupancy function,  $f_0$ , shifts to lower energies). This additional charge must occupy shallower states since the deeper states are filled. The origin of the transferred charge at low energy is not clearly understood at present. The occupancy functions shown in Figs. 5-2 and 5-3 show that the shallow states should be empty. As mentioned previously, the field control pulse is applied immediately following the driving waveform pulse. The existence of transferred charge at low energy may be caused by electrons that have not reached equilibrium prior to the field-control pulse.

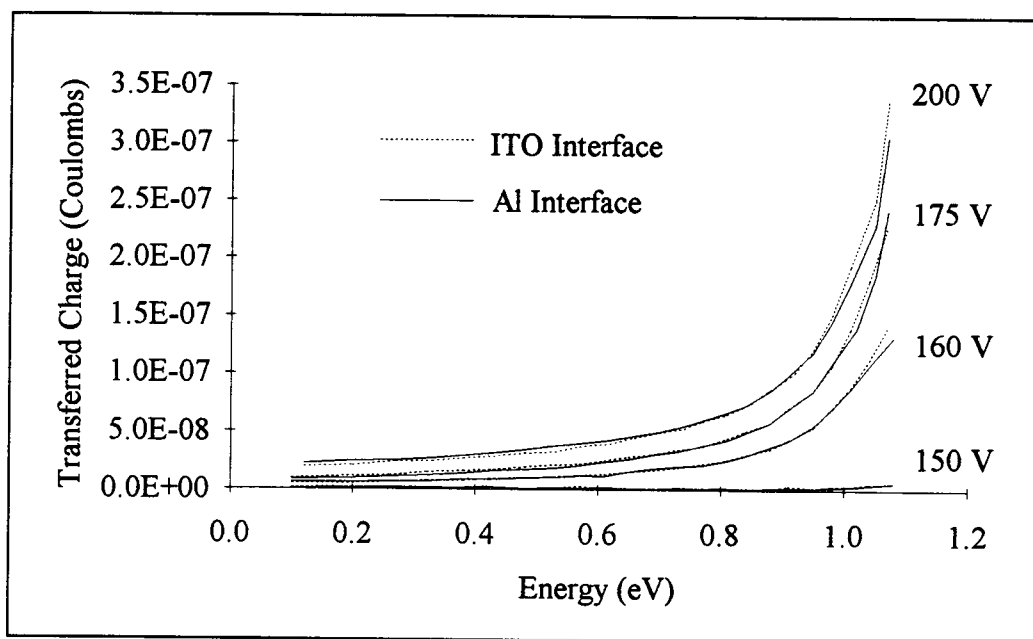


Figure 5-11. Transferred charge versus energy for an ACTFEL device with BTO insulators.

Figure 5-12 shows a plot similar to Fig. 5-11 except that this data corresponds to an ALE grown ACTFEL device with ATO insulators. This device has an asymmetrical interface state distribution. The asymmetry is particularly evident at 195 V. This implies that the difference in the interface state distribution is probably in shallow states that become filled once the driving amplitude reaches high voltage levels. Figure 5-13 shows



data taken from the same ALE sample before and after 10 hours of aging at 200 V. Notice that both curves shift upward with aging and remain symmetrical since the operating voltage is 180 V.

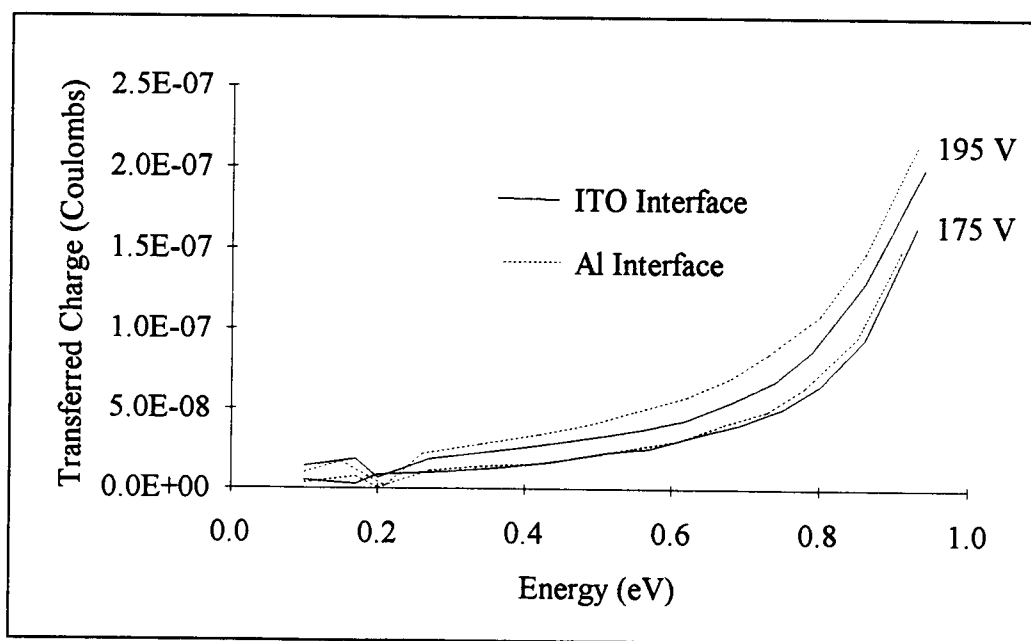


Figure 5-12. ALE ACTFEL device transferred charge versus energy.

Figure 5-14 shows the same device operated at 200V. In this case the device shows the same asymmetry before and after aging. Once again the curves shift upward. This confirms the observation that the device is asymmetrical at high voltage, yet it ages symmetrically. Whatever mechanism is responsible for device aging occurs symmetrically and any asymmetrical characteristics existed prior to aging.

## 5.5 Discussion

Notice that all of the data presented shows a rapid increase in charge (or  $N_{ss}$ ) at approximately 0.9 eV. This is consistently observed for all three different phosphor/insulator systems studied. Devices with SiON, BTO, and ATO insulators have been studied and in all cases the phosphor is ZnS. This leads to two possible conclusions; 1) the interface state distribution is determined primarily by the phosphor and is relatively

independent of the insulating material, or 2) the shape of the transferred charge or  $N_{ss}$  curves is determined by the initial occupancy function,  $f_0$ .

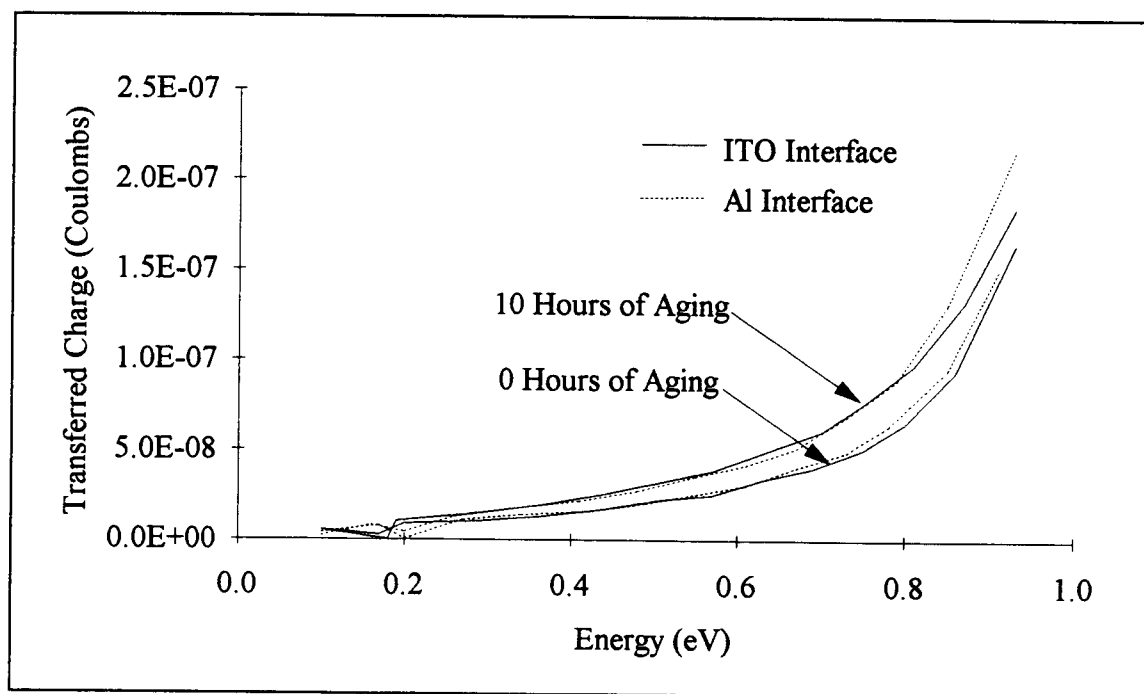


Figure 5-13. ALE ACTFEL device aged at 200V and operated at 180V.

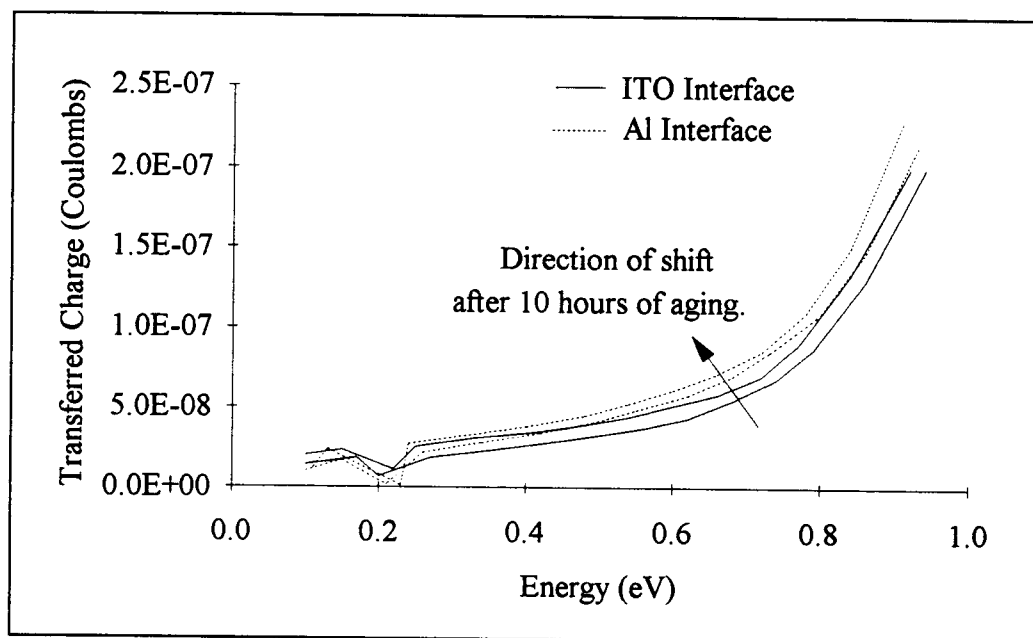


Figure 5-14. ALE ACTFEL device aged and operated at 200V.

The interface state density measurement technique introduced herein has several limitations. First, note that in all cases the initial occupancy function has not populated states shallower than about 0.5 eV nor has this technique been able to probe states deeper than about 1.0 eV. The low energy limit is due to the fact that the amplitude of the driving voltage waveform determines the extent of electron filling at the interface; to fill shallower states would require driving voltages that would cause destructive breakdown of the device. The high energy limit is determined by the maximum electric field that can be generated by the field-control circuit without destroying the device because of excessive charge transfer. Therefore, this technique is limited to an  $E_{qf}$  range of approximately 0.5 to 1.0 eV.

## 5.6 Summary

A new technique for measuring the density and distribution of interface states in an ACTFEL device is described. The total emission rate and electron distribution are found to be independent of temperature. This is due to a very small electron capture cross section of the interface states and the a field-dominated distribution function, respectively.

It is shown that the best energy resolution one can expect in an interface state density measurement is approximately 0.1 eV due to the spreading of the occupancy function. The measured data shows that the interface state distribution rises fairly abruptly at about 0.9 eV in all of the ACTFEL devices measured. This is attributed to an energy state in the ZnS phosphor, possibly a sulfur vacancy, or to the position of the edge of the initial occupancy function. At present, the initial occupancy function position explanation seems the most likely considering the fact that the energy corresponding the rapid increase in the transferred charge curves, shown in Fig. 5-11, shifts to lower energies as the driving voltage is increased (i.e. increasing the driving voltage fills the interface states with more charge and, therefore, the occupancy function shifts to shallower energies). The fact that the curves shift, leads to the conclusion that  $N_{ss}$  technique is measuring the edge of the occupied states which happens to lie at approximately 0.9 eV.

ALE grown ZnS/SiON devices have symmetric interface state densities for driving voltages below 195V, whereas the interfaces are asymmetric for driving voltages above 195V. This is attributed to a difference in the interface state density at shallow energies. Thus, the higher driving voltage fills shallow states that are present only at one of the interfaces. From Fig. 5-12 it seems that the interface on the Al side of the device is emitting more charge at high voltage and must, therefore, be the interface with these additional shallow states. These shallow states are probably due to a chemical difference in the interfaces that originates during device processing. Aging is found to cause an upward shift in the transferred charge curves; this shift occurred symmetrically at both high and low driving voltages. Thus, the interface state density is changed by the same physical mechanism at both interfaces. This is probably due to atomic rearrangement due to impact by hot electrons.

Finally, with regard to the limitations of this technique, ACTFEL interface state densities can be measured for energies between 0.5 and 1.0 eV on either interface.

This work has obvious applications in aging studies, interface-engineering, and it is a valuable technique for refining ACTFEL device models. Bringuier's<sup>1</sup> device physics model assumed a discrete trap level at 1.0 eV and a step function occupancy. In light of this work, it seems that these assumptions are quite reasonable for typical ACTFEL devices.

## **6.0 HOT ELECTRON LUMINESCENCE/MONTE CARLO MODEL**

### **6.1 Introduction**

In this chapter hot electron luminescence experiments performed on both doped and undoped ZnS ACTFEL devices are described. The purpose to these experiments is to determine the extent to which the electron distribution is heated. This measurement provides an experimental basis to help establish the required complexity of the model used in Monte Carlo simulation. To obtain accurate simulation results one must consider how to model the conduction band structure. For low-field electron transport a simple parabolic valley approach is sufficient. However, as the electrons reach higher and higher energies, this approximation fails dramatically. The purpose of the hot electron luminescence measurement is to establish the energy of the hot electron tail which then determines the required complexity of the band structure model for accurate Monte Carlo simulation.

Electron transport in ACTFEL devices is the source of some controversy. One point of view<sup>40-41</sup> contends from Monte Carlo calculations and vacuum emission measurements that electrons travel ballistically through the ACTFEL device and reach exceedingly high energies. Other workers have concluded from Monte Carlo calculations<sup>38-39</sup> and lucky-drift modeling<sup>42</sup> that the average energy of the electron distribution is approximately 1-2 eV with high energy tails out to perhaps 3-4 eV for phosphor fields at which ACTFEL devices typically operate ( $\sim 1.5$ -2.0 MV/cm). The hot electron luminescence measurements discussed in this chapter are similar to those reported previously<sup>44</sup> using ZnS Schottky diodes subjected to dc bias. The hot electron luminescence spectrum observed under dc bias was interpreted<sup>44</sup> as originating from hot electron radiative recombination within the conduction band; it is assumed that the ac hot electron luminescent spectrum measured in the present case arises from the same physical process.

## 6.2 Experimental Technique

The ACTFEL devices used in this work are fabricated by evaporation in the typical stack configuration shown in Fig. 2-1. The measurement is performed on both doped and undoped ACTFEL devices. The undoped samples were used to avoid possible confusion of the emission spectrum by the intense manganese emission at 585 nm.

The hot electron luminescence experiment consists of driving an ACTFEL device with the standard voltage waveform and monitoring the luminescence spectrum. The amplitude of the voltage pulses is approximately 20 V above the threshold for the onset of conduction at a frequency of 100 Hz.

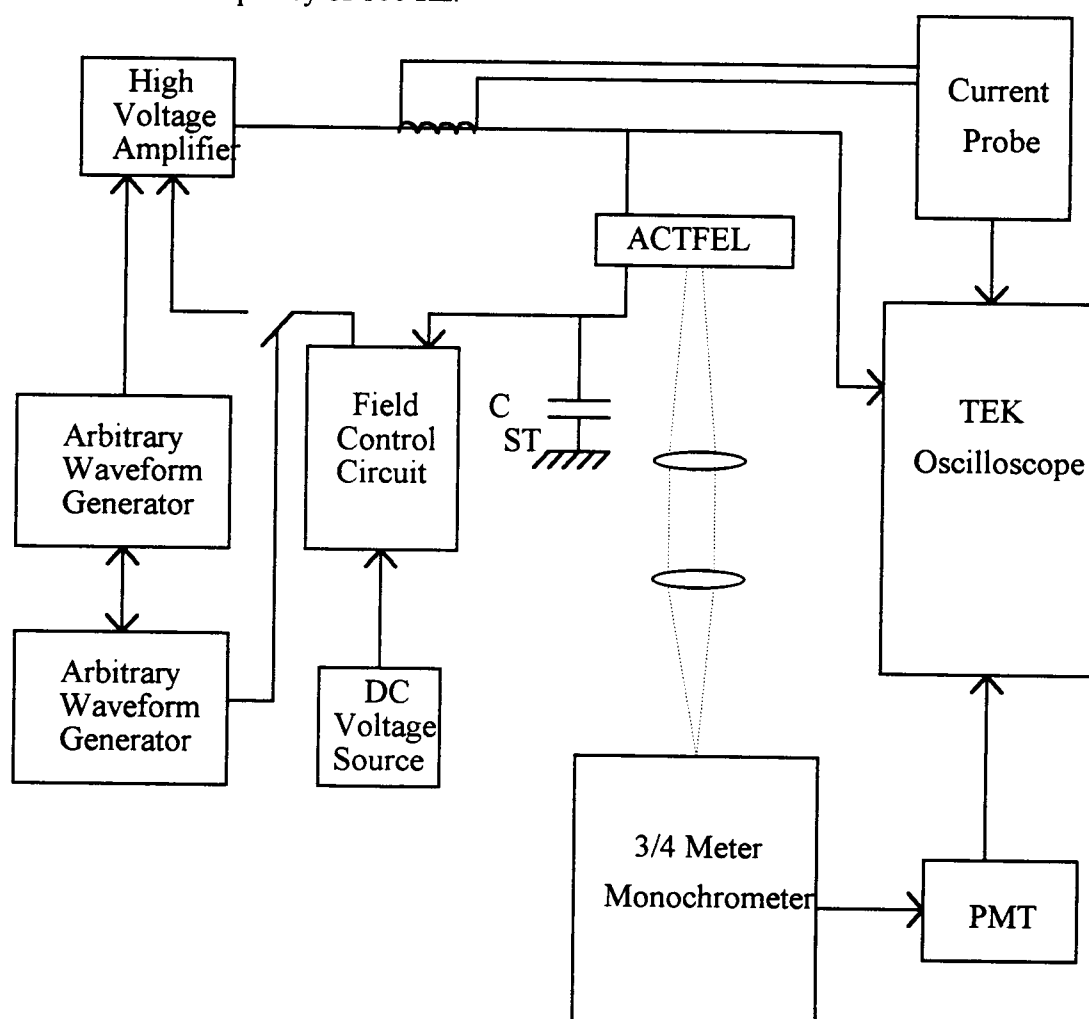


Figure 6-1. Hot electron luminescence experimental set-up.

Hot electron luminescence is measured at three phosphor fields:  $F_p=1.2$ , 1.4, and 1.6 MV/cm. These phosphor field values are obtained using the field-control circuit discussed in the previous chapter and shown in Fig. 5-8. The experimental set-up is shown in Fig. 6-1.

The hot electron luminescence spectra are measured using a SPEX 3/4 meter monochromator and a cooled, extended range photomultiplier tube (PMT). Spectra are obtained in a time-resolved manner by digitally acquiring the voltage across a 50 k $\Omega$  resistor between the PMT and ground. A single-system correction to the raw spectral data is performed which accounts for lens, grating, and detector response.

Optical absorption measurements of the ACTFEL stack are performed using a SPEX Fluorolog System which includes a xenon lamp and a pair of 0.22 meter double monochrometers.

### 6.3 Experimental Results

Phosphor field and hot electron luminescence transient curves are shown in Fig. 6-2 for a wavelength of 460 nm. The first peak in the  $F_p(t)$  curve corresponds to the

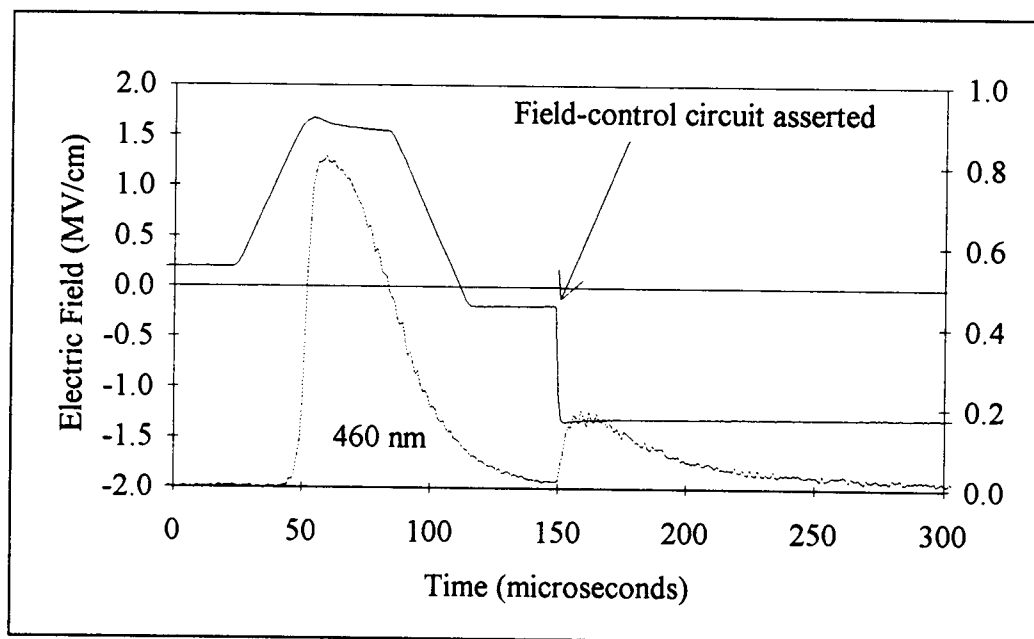


Figure 6-2. Time-resolved electric field and 460 nm luminescence.

application of an external voltage pulse; note that field-clamping occurs at approximately 1.6 MV/cm. The 1.4 MV/cm constant field portion of the  $F_p(t)$  curve occurs when the field-control circuit is operational. Note that although the duration of the hot electron luminescence is very short (microseconds) and is concomitant with the flow of conduction current, the duration of the measured luminescence transient is approximately 100  $\mu$ s which is determined by the RC time constant of the 50 k $\Omega$  resistor and the PMT. Also, notice that the 1.4 MV/cm luminescence signal is weak compared to that of the first peak; 1.2 MV/cm is found to be the smallest phosphor field at which an adequate signal intensity can be obtained with the present set-up. Hot electron luminescence spectra are plotted in Fig. 6-3 for  $F_p=1.2, 1.4$ , and 1.6 MV/cm. The structure observed in Fig. 6-3 is attributed

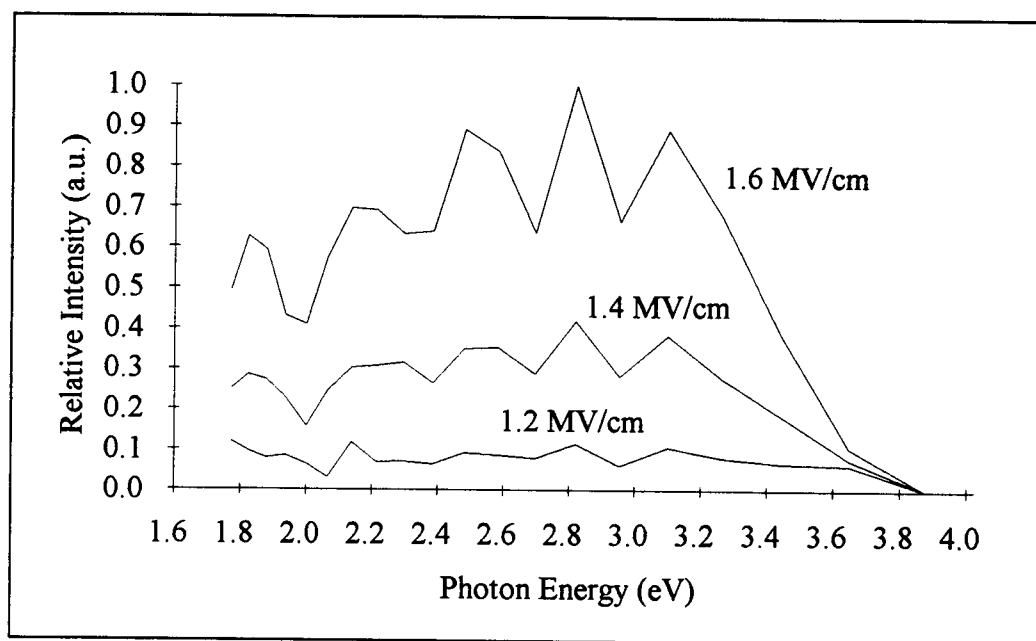


Figure 6-3. Hot electron luminescence at various fields.

to optical interference since these peaks shift, as shown in Fig. 6-4, when the emission angle of the sample is rotated by approximately 45° with respect to the monochromator. As apparent from Fig. 6-3, the high energy, hot electron luminescence cut-off occurs at about 3.7 eV. Optical absorption spectra for the ACTFEL stack, the glass substrate, and



ITO on glass are given in Fig. 6-5. It is clear from Fig. 6-5 that the absorption edge at about 3.7 eV arises from absorption within the ZnS layer.

Thus, a comparison of the hot electron luminescence spectra of Fig. 3 and the optical absorption spectra of Fig. 5 indicates that the high energy, hot electron luminescence cut-off arises from optical absorption within the ZnS layer. Therefore, a correction is made for optical interference and absorption effects, the hot electron luminescence spectrum is broad and rather structureless out to energies approaching 3.7 eV, the bandgap of ZnS.

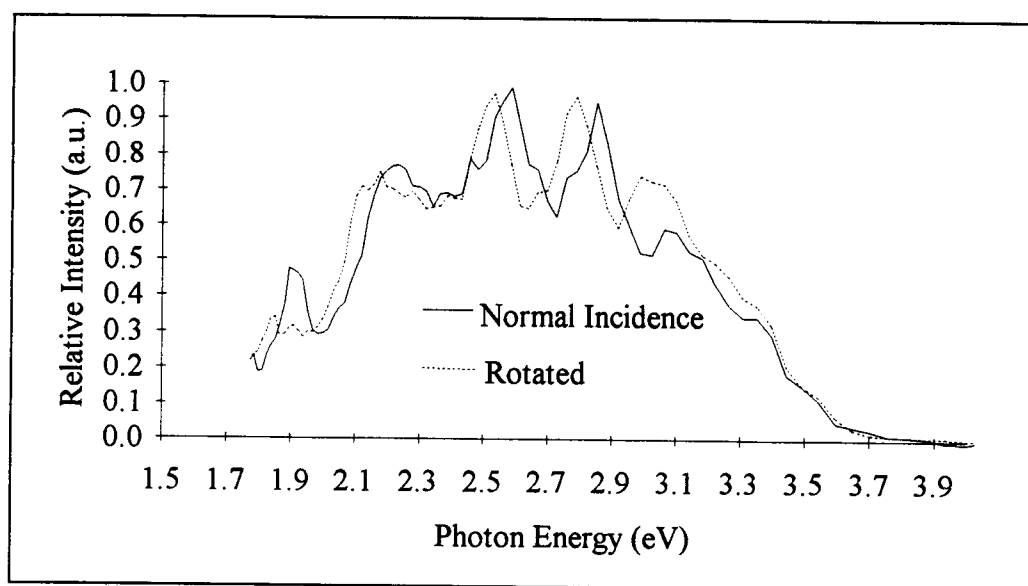


Figure 6-4. Rotated and normal incidence hot electron luminescence at 1.6 MV/cm.

The hot electron luminescence spectrum arises from radiative transition of energetic electrons within the ZnS conduction band<sup>44-45</sup> and, therefore, is related to the hot electron distribution. Thus, it is concluded that a significant fraction of the hot electrons transiting the ZnS possess kinetic energies near to, and most likely in excess of, the 3.7 eV bandgap of ZnS. Moreover, although the intensity of the hot electron luminescence scales with the magnitude of the applied field, as indicated in Fig. 6-3, the shape of the hot electron luminescence spectrum is relatively independent of field. In

particular, the high energy tail extends out to 3.7 eV for all of the fields investigated. This implies that for any field large enough to cause significant tunnel emission from interfaces states, a substantial number of the emitted electrons will reach at least bandgap energies. Nothing can be inferred about the hot electron distribution for energies in excess of 3.7 eV since these energies are inaccessible to this experiment.

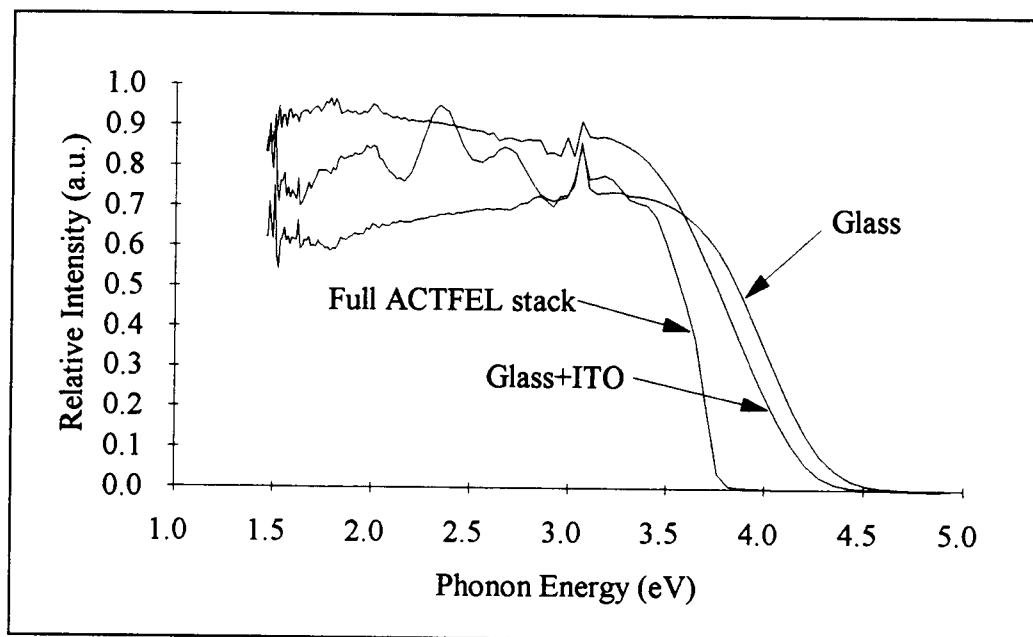


Figure 6-5. ACTFEL film transmission spectra.

Further attempts were made to optically measure the high energy tail of the electron emission. A sample was broken and edge emission monitored. The edge emission spectrum contains the same 3.7 eV cut-off as before. This implies that the intensity of edge-emitted, high energy photons is so low that they are completely undetectable.

The fact that conduction electrons reach very high energies greatly complicates Monte Carlo simulation of ACTFEL devices. Figure 6-6 shows the conduction band density of states for Bhattacharyya et al.'s<sup>39</sup> non-parabolic approximation and a more realistic density of states. Notice that Bhattacharyya et al.'s calculation overestimates the

density of states for energies in excess of 2.7 eV. This causes more electron scattering in the simulation and, therefore, predicts a cooler distribution. Bhattacharyya et al.'s simulation predicts electron energies up to 3.5 eV for a field of 1.5 MV/cm. It is speculated that if a more realistic density of states is utilized, a significant fraction of the electrons would reach 3.7 eV even at fields as low as 1.2 MV/cm, as found experimentally.

#### 6.4 Discussion

One implication of the high energy of the electron distribution inferred from the hot electron luminescence experiment is that it now seems not only possible but likely that band to band impact ionization occurs in undoped devices. The threshold energy for impact ionization,  $E_{th}$ , is given by<sup>46</sup>,

$$E_{th} = \frac{2m_e + m_h}{m_e + m_h} E_G \quad (6-1)$$

where<sup>46</sup>  $m_e = 0.34m_0$  is the electron effective mass,  $m_h = 1.76m_0$  is the heavy hole effective mass, and  $E_G = 3.7$  eV is the bandgap. This results in  $E_{th}$  of approximately 4.3 eV.

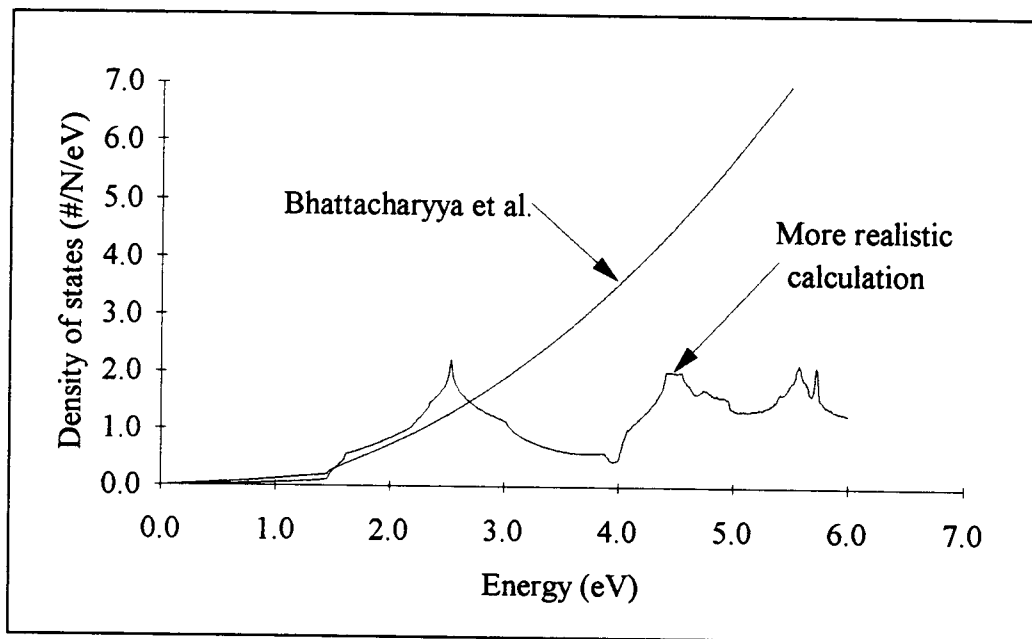


Figure 6-6. ZnS conduction band density of states.

Extrapolation of Fig. 6-3 suggests that band-to-band impact ionization would likely occur in ZnS ACTFEL devices under normal operating conditions.

A second implication of the work reported herein is that the achievement of efficient blue ACTFEL devices should not be impeded by the transport properties, if ZnS is employed as the host phosphor.

Finally, it should be noted that although all of the data shown in this chapter is for undoped samples, the high energy portion of the hot electron luminescence spectrum is identical for Mn-doped samples, to within the accuracy of the experiment. Thus, the Mn luminescent impurities do not significantly cool the electron distribution. This result is consistent with the Monte Carlo simulation<sup>39</sup> of Bhattacharyya et al., who find the Mn impact excitation scattering rate to be several orders of magnitude smaller than that of polar optical phonon or intervalley scattering.

## 6.5 Summary

The hot electron luminescence spectrum is measured for an ACTFEL device in which the ZnS is grown by evaporation. The luminescence spectrum is broad and featureless and is cut off at the ZnS bandgap due to optical absorption. This result provides evidence that a substantial fraction of the electrons transiting the ACTFEL device have energies near to or in excess of the ZnS bandgap.

As far as Monte Carlo modeling of an ACTFEL device is concerned, the work described in the chapter demonstrates the need to accurately model the conduction band density of states up to energies greater than 3.7 eV above the conduction band minimum.

## **7.0 CONCLUSIONS AND RECOMMENDATIONS FOR FUTURE WORK**

The research presented in this thesis focuses on the physics of ACTFEL devices with emphasis placed on refining ACTFEL device models. In this chapter, the experimental results of this thesis are reviewed, the impact to ACTFEL device modeling is considered, and recommendations for future research are presented.

### **7.1 Waveform Variation Trends\Equivalent Circuit Model**

Chapter 3 presented a refined equivalent circuit model for the ACTFEL device. It is found that by adding an additional RC time constant in the conduction current path, relaxation charge which flows across the phosphor layer while the driving voltage pulse is at its maximum value, can be modeled. This observation provides a better fit to the time-dependent device response. More importantly, accounting for relaxation charge allows one to fit the ACTFEL device response over a wide range of variations in the shape of the driving waveform pulse.

It is known that in a matrixed display each row or column looks like a distributed network or a transmission line. This work is very applicable to the design of full panel displays because as the pulse propagates down the line, the pulse shape changes. This equivalent circuit should predict the electrical behavior of the first pixel as well as the last pixel in the line.

Chapter 3 also presented a "optical" equivalent circuit where the current flowing through one of the branches can be interpreted as the intensity of light emitted by the device. This model, which is simulated with the electrical model, allows a designer to model both the electrical and optical variation across the panel.

One aspect of these models that is disappointing is the fact that they are derived empirically and are, therefore, difficult to associate with the device physics or processing. Many attempts were made to relate the device physics equations presented in Chapter 4 to the equations which describe the equivalent circuit response. Attempts were also made to linearize the device physics equations. Unfortunately, these methods did not succeed in

simplifying the problem.

The following are a few suggestions for future work.

**1) Refine diode models.**

Further work may be possible in the refinement of the back-to-back diode models. Specifically, it may be possible to relate the I-V characteristics of the diodes to the I-V characteristics of the phosphor layer. This fit could be performed theoretically if one assumes that emission occurs via pure tunneling (a reasonable assumption based on the conclusions of Chapter 5). In this case, one would fit a SPICE simulated diode curve to the emission rate, Eqn. 5-5. The fit could also be performed experimentally by fitting the SPICE diode I-V curves to a measured conduction current versus phosphor field curve.

**2) Simulate device performance with state-space analysis.**

Another possible approach to ACTFEL device simulation is to use state-space analysis from systems theory. This would require one to look at the device as a non-linear system which is, in general, very difficult. If successful, this may allow one to construct a matrix to model the response of a single device and extend this to a full panel simulation by multiplication of successive matrices which represent individual pixels. This would be a very significant contribution in terms of simulation speed. Note that with the equivalent circuit model presented in this thesis, hundreds of pixels connected in parallel must be simulated in order to observe the effects of pulse degradation.

## **7.2 Phosphor Space Charge/Device Physics Model**

In Chapter 4 the possibility of a spatial distribution of charge in the phosphor is considered. Very convincing evidence is found for space charge in ALE devices at low temperature. In particular, two additional current peaks on the falling edge of the voltage pulse are observed. The first current peak occurs before the phosphor electric field (assuming no space charge) changes sign. This leads to the conclusion that space charge is present at low temperature. Also, the first peak emits 460 nm light and this emission is thermally quenched. This agrees with observations made by other researchers and leads to

the conclusion that the emission is due to recombination between Cl atoms and Zn vacancies. The space charge is believed to originate from the impact ionization of Zn vacancies by energetic electrons. Finally, this space charge is found to form predominately on the ITO or first grown side of the phosphor layer.

The impact of space charge is primarily with respect to asymmetrical device operation and aging. However, one must keep in mind that this effect is only observed at very low temperatures and at driving voltages of approximately 160 V. Space charge is believed to originate at high temperatures when larger driving voltages are employed. However, at higher voltage the effects of space charge are believed to be present during the main conduction current pulse. The secondary current peaks are not visible. This implies that space charge effects are much more difficult to isolate at room temperature.

With these conclusions in mind, the following recommendations for future work are presented.

**1) Establish impact and identify of cause of space charge.**

Generally speaking, the first step in pursuing future research in this area is to identify the impact of space charge to devices under normal, room temperature operation. It is recommended that future work focus on device aging and/or B-V symmetry during any study of space charge. If strong evidence for space charge is observed, some kind of chemical profile of the phosphor layer should be attempted. A possible technique for this measurement is ion milling the phosphor to obtain a depth profile and performing either Auger electron emission or x-ray fluorescence to determine the chemical concentration. This kind of research would be well received as it would address the impact of space charge and identify its chemical origin.

**2) Study space charge in other types of ACTFEL devices.**

Another possible area for future work is to consider space charge in other types of ACTFEL devices; for example, SrS:Ce devices grown by ALE. Researchers at Planar International are very interested in understanding and modeling a dissipative current which

flows during the falling edge of the voltage pulse. Assessment of the dissipative current may lead to observations similar to those made in Chapter 4 and the measurement may be possible at room temperature.

### **3) Space charge modeling with an equivalent circuit.**

Finally, additional work is certainly possible in the area of space charge modeling. If, for instance, blue devices are shown to have significant space charge effects at room temperature, it would be very helpful to refine the equivalent circuit model presented in Chapter 3 to include this effect. Equation 4-7 of Chapter 4 indicates that the phosphor field has two components when space charge is present. Perhaps another capacitor could be connected in series with the phosphor capacitor. This capacitor should be shorted until conduction current flows. The charging and discharging could be controlled with Zener diodes with various breakdown voltages. Another approach would be to model the effect as a capacitor located somewhere in the conduction current path. This is less physical, but it is easier to visualize the various techniques for charging (with conduction current) and discharging (during the falling edge of the voltage) the capacitor.

## **7.3 Interface State Distribution/Device Physics Model**

Chapter 5 introduced a new technique for measuring the distribution of interface states in an ACTFEL device. The technique is based on a new field-control circuit which forces the electric field to a constant value during conduction. This is achieved by changing the external bias to compensate for the change in the phosphor field due to the redistribution of charge. The interface state measurement technique can measure the distribution at either interface for energies between approximately 0.5 to 1.0 eV. The distribution is found to rapidly increase at 0.9 eV for all devices measured. This common feature is attributed to that fact that ZnS is used as the phosphor material in each device measured.

This work has great potential for studying device aging mechanisms and interface engineering. With respect to aging studies, it may be possible to determine which



interface changes as the device ages. Also, if the resolution of the measurement can be improved, it may be possible to determine the energy range in which the changes occur and, therefore, identify the source. With respect to interface engineering, studying the distribution of states for devices with different phosphors, insulators, and deposition processes may lead to a procedure for tailoring the interface to optimize the efficiency of the device or reduce the operating voltage. It may also be possible to control the energy at which electrons are emitted from by depositing thin interfacial-layers between the insulator and phosphor materials.

Of all the experiments performed in this thesis, the interface state distribution measurement is the most highly recommended for future work. The following lists areas which deserve particular attention.

**1) Identify possible measurement error at low energies.**

In Chapter 5, the presence of transferred charge at low energies is identified as a possible error in the measurement. From the calculation of the occupancy function, states shallower than about 0.5 eV should not be filled. This is a problem that needs to be addressed. Two likely causes of the charge at low energies are 1) a non-equilibrium electron distribution and, 2) error in the field-control voltage. The first cause is attributed to electrons that have not had sufficient time to reach a stable occupancy function prior to the assertion of the field-control circuit. Figure 5-7 shows the field-control circuit asserted immediately following the driving voltage pulse. In this figure, relaxation charge flows while the voltage pulse is at maximum amplitude. Therefore, relaxation charge may lead to a non-equilibrium electron distribution. If this is the cause, moving the field-control pulse to later times may correct the low energy charge problem. The second possible cause is attributed to the fact that the field-control circuit generates a voltage,  $V_{ext}$ , which is applied to the device after measuring the Sawyer-Tower voltage. However,  $V_{st}$  is actually applied across both the device and the Sawyer-Tower capacitor rather than just the ACTFEL device. This may lead to an error of a few volts because of the voltage

drop across  $C_{st}$ . If this is the cause of the error at low energy, the problem could be solved modifying the field control circuit to subtract  $V_{st}$  from Eqn. 5-16 before  $V_{ext}$  is calculated.

## **2) Study the interface state distribution of other types of ACTFEL devices.**

As all of the studies to date have been performed on ZnS devices with ATO, BTO, and SiON insulators, it is recommended that the interface characterization be performed on other devices with different phosphors, such as SrS and CaS. If these devices show similar characteristics, measurements should be performed on non-sulfur based ACTFEL devices. This is suggested because sulfur vacancies are speculated to be a possible cause of the rapid increase in the density of states at 0.9 eV. Therefore, non-sulfur based phosphors may demonstrate more distinctive features in the distribution.

## **7.4 Hot Electron Luminescence/Monte Carlo Model**

Chapter 6 presents a measurement of the electron luminescence which is used to determine the extent to which the electrons are heated during transport. The measurement shows that for any field sufficient for electron emission, a significant fraction of the electrons reach energies in excess of 3.7 eV. Hotter electrons are likely, but photons corresponding to these high energy electrons are absorbed by the ZnS layer before exiting the device. Therefore, the current technique is not capable of specifying the extent of heating in these devices.

Future work in this area can be pursued by Monte Carlo simulation and in experimental measurement of electron energies during transport.

### **1) Refine Monte Carlo simulation with a full band structure calculation.**

This work indicates that electrons obtain much higher energy than originally thought and that a non-parabolic model of the conduction band is not sufficient. To accurately predict bulk ZnS transport properties a more realistic conduction band model is necessary. This will most likely involve a full band structure calculation.

**2) Measure hot electron luminescence in a low-field regime and compare with Monte Carlo simulation.**

A slightly modified experiment may be able to generate additional experimental data to compare with Monte Carlo results at low fields. Specifically, a new device could be fabricated where both electrodes are formed with ITO and no insulators are deposited. Thus, the structure is Glass/ITO/ZnS/ITO. A dc bias is applied across the electrodes giving rise to a low, constant electric field. Then, a laser is used to inject carriers from the ITO electrode into the conduction band of ZnS. These electrons gain energy from the field and radiatively recombine to shallower conduction band states exactly like the previous electron luminescence experiment. Therefore, once the excitation spectrum has been accounted for, the remaining portion of the emission is due to hot electron luminescence. In this low field regime, the electrons should not reach 3.7 eV, so the maximum in the emission spectrum can be measured. By stepping the field through several values, one should be able to provide a comparison to the results predicted by Monte Carlo simulation at low fields.

**3) Assess maximum electron energy with a variable insulating barrier.**

Another technique that may allow one to assess the high energy tail of the electron distribution is a variable insulating barrier. The details are still unclear, but essentially one would modify the device so that the insulating barrier that the electrons impact after transport is variable. The device might be fabricated as follows; glass/ITO/SiON/ZnS/ITO(thin)/Insulator(Thin)/Al. The thin ITO layer (probably a few hundred Angstroms thick) is used to bias the device (i.e. to create the high field). The outer Al electrode can be used to bend the top of the thin insulating layer and thus form a variable barrier for electrons. If the bias on the thin insulating layer is swept during conduction, one may actually be able to map the distribution of electrons during conduction. A similar technique has been used to map the electron distribution in bipolar transistors where the base is formed with a GaAs superlattice<sup>48</sup>.

## BIBLIOGRAPHY

- [1] E. Bringuier, "Charge Transfer in ZnS-type Electroluminescence", J. Appl. Phys., vol. 66, no. 3, pp. 1314, 1989.
- [2] A.A. Douglas and J.F. Wager, "ACTFEL Device Response to Systematically Varied Pulse Waveforms", Sixth International Workshop on Electroluminescence, El Paso, TX, 1992.
- [3] A.A. Douglas and J.F. Wager, "Electrical Characterization and Modeling of ZnS:Mn ACTFEL Devices with Various Pulse Waveforms", SID International Symposium Digest, 23, 1992.
- [4] A.A. Douglas, J.F. Wager, D.C. Morton, J.B. Koh, and C.P. Hogg, "Evidence for Space Charge in Atomic Layer Epitaxy ZnS:Mn Alternating-Current Thin-Film Electroluminescent Devices", J. Appl. Phys. vol. 73, no. 1, 1993.
- [5] A.A. Douglas, J.F. Wager, D.C. Morton, J.B. Koh, and C.P. Hogg, "Space Charge in ZnS:Mn Electroluminescent Devices", Electrochemical Society 182nd Meeting, Oral Presentation, 1992.
- [6] A.A. Douglas, J.F. Wager, D.C. Morton, J.B. Koh, and C.P. Hogg, "Hot Electron Luminescence in ZnS Alternating-Current Thin-Film Electroluminescent Devices", SID International Symposium Digest, 24, 1993.
- [7] A.A. Douglas, J.F. Wager, D.C. Morton, J.B. Koh, and C.P. Hogg, "Hot Electron Luminescence in ZnS:Mn Electroluminescent Devices", Electrochemical Society 182nd Meeting, Oral Presentation, 1992.
- [8] A.A. Douglas, J.F. Wager, D.C. Morton, J.B. Koh, and C.P. Hogg, "Electron Luminescence in Doped and Undoped ACTFEL Devices", Appl. Phys. Lett., Submitted.
- [9] M. Leskela and M. Tammenmaa, Materials Chemistry and Physics, vol. 16, pp. 349, 1987.
- [10] C. King, "EL Displays", Sixth International Workshop on Electroluminescence, El Paso, TX, Oral Presentation, 1992.
- [11] C.B. Sawyer and C.H. Tower, Phys. Rev. 35, pp. 269, 1930.
- [12] V.P. Singh and S. Krishna, J. Appl. Phys. vol. 70, pp. 1811, 1991.

- [13] Y.S. Chen and D.C. Krupka, "Limitation imposed by field clamping on the efficiency of high field ac electroluminescence in thin films," J. Appl. Phys., vol. 43, pp. 4089, 1972.
- [14] R.C. Mc Arthur, J.D. Davidson, J.F. Wager, I. Khormaei, and C.N. King, "Capacitance-voltage characteristics of alternating-current thin-film electroluminescent devices," Appl. Phys. Lett., vol. 56, pp. 1889, 1990.
- [15] J.D. Davidson, J.F. Wager, and S. Kobayashi, "Aging studies of evaporated ZnS:Mn alternating-current thin-film electroluminescent devices," J. Appl. Phys., vol. 71, no. 8, 1992.
- [16] J.D. Davidson, J.F. Wager, I. Khormaei, C.N. King, R. Williams, "Electrical Characterization and modeling of Alternating-Current Thin-Film Electroluminescent Devices," IEEE Trans. on Elect. Dev., vol. 39, no. 5, pp. 1122, 1992.
- [17] J. D. Davidson, M.S. Thesis, Oregon State University, 1991.
- [18] S. M. Sze, *Physics of Semiconductor Devices*, 2nd ed., Wiley, New York, pp. 49, 1981.
- [19] D.H. Smith, "Modeling a.c. Thin-Film Electroluminescent Devices," J. Lum., vol. 23, pp. 209, 1981.
- [20] Y.A. Ono, H. Kawakami, M. Fuyama, and K. Onisawa, Jpn. J. Appl. Phys., vol. 26, pp. 1482, 1987.
- [21] K.W. Yang, S.J.T. Owen, and D.H. Smith, IEEE Trans. Electron Devices ED-28, pp. 703, 1981.
- [22] W.E. Howard, O. Sahni, and P.M. Alt, J. Appl. Phys., vol. 53, pp. 639, 1982.
- [23] K.W. Yang and S.J.T. Owen, IEEE Trans. Electron Devices ED-30, pp. 452, 1983.
- [24] P.M Alt, D.B. Dove, and W.E. Howard, J. Appl. Phys., vol. 53, pp. 5186, 1982.
- [25] J.M. Jarem and V.P. Singh, IEEE Trans. Electron Devices ED-35, pp. 1834, 1988.
- [26] K.A. Neyts, IEEE Trans. Electron Devices ED-38, pp. 2604, 1991.
- [27] E. Bringuier and A. Geoffroy, "Charge transfer in ZnS-type electroluminescence revisited," Appl. Phys. Lett., vol. 60, pp. 1256, 1992.

- [28] A. Geoffroy and E. Bringuier, "Bulk deep traps in ZnS and their relation to high-field electroluminescence," *Semicond. Sci. Tech.*, vol.6, 1991.
- [29] K. Neyts, P. De Visschere, J. Van den Bossche, D. Corlatan, and F. Vereecken, "Transient Measurements on AC Thin-Film Electroluminescent Devices," *Electrochemical Society 182nd Meeting, Poster Presentation*, 1992.
- [30] A. Mikami, K. Terada, K. Okibayashi, K. Tanaka, M. Yoshida, and S. Nakajima, "Chemical vapor deposition of ZnS:Mn electroluminescent films in a low-pressure halogen transport system," *J. Crystal Growth*, vol. 110, pp. 381, 1991.
- [31] S. Kobayashi, J.F. Wager, and A. Abu-Dayah, "Distribution of Trapped Electrons at Interface States in ACTFEL Devices," *Sixth International Workshop on Electroluminescence*, El Paso, TX, Poster Presentation, 1992.
- [32] Y. Sano and K. Nunomura, "Thermally Stimulated Currents in Thin-Film Electroluminescent Devices," *Electroluminescence*, Springer Proceedings in Physics, vol. 38, 1989.
- [33] Jia Zhen Zheng and J.W. Allen, "Photocapacitance studies of deep levels in zinc sulfide," *Semicond. Sci. Tech.*, vol. 5, 1990.
- [34] F. A. Kröger, *The Chemistry of Imperfect Crystals*, 2nd ed., vol.II, pp.741-743.
- [35] Landolt-Börnstein, New Series (Springer, Berlin, 1987), vol. 22a, p.168.
- [36] G. Vincent, A. Chantre, and D. Bois, "Electric field effect on thermal emission of traps in semiconductor junctions", *J. Appl. Phys.*, vol. 50, no. 8, 1979.
- [37] E. Rosencher, V. Mosser, and G. Vincent, "Transient-current study of field-assisted emission from shallow levels in silicon," *Physical Review B*, vol. 29, no. 3, 1984.
- [38] K. Brennan, "Theory of high-field electronic transport in bulk ZnS and ZnSe," *J. Appl. Phys.*, vol. 64, no.8, pp. 4024, 1988.
- [39] K. Bhattacharyya, S.M. Goodnick, and J.F. Wager, "Monte-Carlo Simulation of High-Field Transport in Alternating-Current Thin-Film Electroluminescent Devices," *Sixth International Workshop on Electroluminescence*, El Paso, TX, Poster Presentation, 1992.
- [40] H.J. Fitting, A. Von Czarnowski, and G.O. Müller, "Ballistic Transport in Alkaline Earth Sulfides," *J. Crystal Growth*, vol. 101, pp. 876, 1990.

- [41] R. Mach and G.O. Müller, "Ballistic Transport and Electroluminescence in IIB-VI and IIA-VI Compounds," J. Crystal Growth, vol. 101, pp. 967, 1990.
- [42] E. Bringuier, J. Appl. Phys. vol. 70, pp. 4505, 1991.
- [43] Private communication with E. Bringuier, J. Allen, and K. Bhattacharyya.
- [44] N.E. Rigby and J.W. Allen, "Light emission from hot electrons in zinc sulfide," J. Phys. C: Solid State Phys., vol. 21, pp. 3483, 1988.
- [45] P. Thioulouse, "ZnS Blue Emission Probing for the Study of AC Thin-Film Electroluminescent Structures," J. Crystal Growth, vol. 72, pp.545, 1985.
- [46] C.M. Wolfe, N. Holonyak, Jr., and G.E. Stillman, *Physical Properties of Semiconductors*, Prentice Hall, Englewood Cliffs, NJ, p. 299., 1989.
- [47] K.A. Neyts and P. De Visschere, "Analytical model for thin-film electroluminescent devices," J. Appl. Phys., vol. 68, no. 8, pp. 4163, 1990.
- [48] A. Choo, M.S. Thesis, Oregon State University, 1993.